Dankwoord

This PhD has been a nice four-year journey, having the opportunity to work in such a wonderful group, learning a lot about light and living in lovely Gent. It has been four years of happiness, satisfaction and hard work.

For all these great things, first of all, I would like to thank my supervisors Geert and Günther. I was lucky that I had supervisors who were expert in the field but also were like real friends. Geert is such a kind and very wonderful person who always has great ideas with an ambitious and positive spirit. Motivating a PhD student is one of the important characteristics of a good supervisor and he is very good in that. I also had a chance to work with Günther. He is a well-organized, precise and smart. I learned from him to be structured and accurate. I am thankful for sharing his knowledge and experience with me. The collaboration with Geert and Günther during this PhD has been an excellent opportunity in my life which I will never forget!

I would like to thank the big family of the Photonics Research Group from professors to Post docs and PhDs, clean-room staff, secretary and support staff in iGent. I wish all the best for all of you!

Finally I would like to thank my parents and my brothers. I shared the memory with them which is curved in my heart for an endless time.

Special thanks go to my love (and colleague) Leila, who is a happy friend and a great support to my life. Without her I would not enjoy my research and life this much. She is a strong and provident partner. I hope this scientific life lasts forever.

Ghent, Nov 2016
Amin

Table of Contents

List of Acronyms

A

AC	Alternating Current
ASK	Amplitude Shift Keying
AWG	Arbitrary Waveform Generator

B

BCB	Benzocyclobutene
BER	Bit Error Rate

C

CD	Carrier Depletion
CH	Carrier Heating
CML	Chirp Managed Laser
CMOS	Complementary Metal-Oxide-Semiconductor
CPR	Carrier Photon Resonance
CW	Continuous-Wave

D

DBR	Distributed Bragg Reflector
DC	Direct Current
DFB	Distributed Feedback
DH	Double Heterostructure
DML	Directly Modulated Laser

E

EAM	Electro Absorption Modulator
ECC	Error Correcting Coding
ED	Electrical Duobinary

F

FEC	Forward Error Correction
FEE	Feed Forward Equalization
FIB	Focused Ion Beam
FM	Frequency Modulation
FSK	Frequency Shift Keying

G

GSG	Ground Signal Ground

I

ICP	Inductively Coupled Plasma
IM/DD	Intensity Modulation/ Direct Detection
ISI	Inter-Symbol Interference

L

LED	Light Emitting Diode
LSHB	Longitudinal Spatial Hole Burning

M

MMI	Multi-Mode Interferometer
MQW	Multi Quantum Well
MZM	Mach-Zehnder modulator

N

NRZ	Non Return to Zero
NZ-DSF	Non Zero-Dispersion Shifted Fiber

O

OD	Optical Duobinary
OOK	On Off Keying
OSR	Optical Spectrum Reshaper

P

PAM	Pulse Amplitude Modulation
PICs	Photonic Integrated Circuits
PL	Photoluminescence
PECVD	Plasma-Enhanced Chemical Vapor Deposition
PPR	Photon Photon Resonance
PON	Passive Optical Network
PSK	Phase Shift Keying
PSD	Power Spectral Density
PPG	Pulse Pattern Generator
PRBS	Pseudo Random Binary Sequence

R

RIE	Reactive-Ion Etching

S

SOI	Silicon on Insulator
SEM	Scanning Electron Microscope
SMSR	Side Mode Suppression Ratio
SHB	Spectral Hole Burning
SOA	Semiconductor Optical Amplifier
SNR	Signal to Noise Ratio
SCH	Separate Confinement Heterostructure

T

TE	Transverse-Electric
TM	Transverse-Magnetic

V

VCSEL	Vertical Cavity Surface Emitting Laser

W

WDM	Wavelength Division Multiplexing

Nederlandse samenvatting
–Summary in Dutch–

Optische interconnecties worden van steeds groter belang voor de informatiemaatschappij. Vroeger werd optische-vezelcommunicatie vooral gebruikt voor de transmissie van data over grotere afstanden (10 km en meer bv.). Sinds enkele jaren wordt ook glasvezelcommunicatie gebruikt voor interconnecties over kortere afstanden, bv. over enkele honderden meter. De afstanden waarvoor optische interconnecties ingevoerd worden, worden korter naarmate de bitsnelheden stijgen. De transmissieverliezen van koperkabels nemen namelijk heel sterk toe met de bitsnelheid daar waar de transmissieverliezen van optische vezels laag zijn ongeacht de bitsnelheid.

Meer en meer wordt gebruik gemaakt van grote hoeveelheden data die in datacentra opgeslagen zijn en worden dataverwerkingen en – bewerkingen integraal in het datacentrum uitgevoerd. Om daarbij de massieve hoeveelheid gegevens te kunnen uitwisselen tussen de verschillende servers van het datacentrum is er nood aan interconnecties met heel hoge datadebieten. Er wordt momenteel gewerkt met bitsnelheden van 100 Gbit/s, maar er is ook een standaard in voorbereiding voor 400 Gbit/s interconnecties en reuzen als Facebook en Google zijn zelfs vragende partij voor een Terabit/s standaard.

Voor de zender voor die optische interconnecties zijn er verschillende opties. Men kan gebruik maken van een laserdiode met constant optische uitgangsvermogen en de intensiteit moduleren met een externe modulator. Modulatoren hebben het voordeel van een lage parasitaire frequentiemodulatie, hetgeen vooral een voordeel is voor communicatie over langere afstanden, maar ze hebben het nadeel van groter te zijn en door het inkoppelingsverlies is ook een groter laservermogen vereist. Voor kortere afstanden kan men ook een direct-gemoduleerde laserdiode gebruiken, waarbij het uitgangsvermogen van de laserdiode gemoduleerd wordt door het moduleren van de elektrische stroom die in de laserdiode wordt geïnjecteerd. Dit kan meestal gebeuren met een lagere vermogenconsumptie dan bij externe modulatie, maar het is niet evident om de gewenste bitsnelheden te bereiken.

Daarnaast is er een sterke tendens om vooral silicium-gebaseerde fotonisch geïntegreerde circuiten te ontwikkelen. Deze technologie heeft als voordeel dat men de geavanceerde fabricatiemethodes uit de micro-electronica kan

hergebruiken voor de fabricatie van fotonisch geïntegreerde circuiten, en dat er een mogelijkheid is om elektronica en fotonica te co-integreren. In dit platform (dat eigenlijk bestaat uit silicium op oxide) kunnen zeer compacte passieve golfgeleidercomponenten gerealiseerd worden (bv. optische filters, multiplexers, e.d.). Maar silicium heeft als belangrijk nadeel dat het niet geschikt is voor de realizatie van lichtbronnen (LEDs of laser diodes).

In de voorbije jaren is, o.a. in de onderzoeksgroep Fotonica van de universiteit Gent, belangrijk werk geleverd op het bonden van III-V materialen op silicium-op-oxide golfgeleiders. Membranen bestaande uit diverse dunne lagen van InP, InGaAs, InGaAsP, of InAlGaAs kunnen nu met grote betrouwbaarheid gebond worden. III-V materialen zijn wel geschikt voor de realisatie van laser diodes. Post-processsing van de gebonden membranen laat dan ook toe om halfgeleiderlasers te fabriceren op silicium-op-oxide.

In het doctoraat werd verder gewerkt op een eerder ontwikkelde, heterogeen geïntegreerde DFB laser diode. DFB (distributed feedback) laser diodes zijn de lichtbronnen die traditioneel gebruikt worden voor optische vezelcommunicatie. Ze emitteren licht met hoge spectrale zuiverheid dankzij een diffractierooster dat in de laserstructuur is ingebed. Indien de lasers heterogeen geïntegreerd worden op silicium-op-oxide kan het diffractierooster geëtst worden in de siliciumgolfgeleider, hetgeen de post-processing op de InP membranen achteraf vergemakkelijkt. In onze heterogeen geïntegreerde DFB laser diodes is het licht vooral geconcentreerd in het InP membraan. Hierdoor wordt een grote overlap bekomen tussen de lasermode en de actieve laag, de laag die voor de versterking zorgt. Aan beide uiteinden van de laser wordt het licht dan met behulp van tapers gekoppeld naar de siliciumgolfgeleider, waarna het licht verder kan propageren in deze siliciumgolfgeleider. In principe kunnen verschillende laser diodes op die manier samen geïntegreerd worden tot een multigolflengtelaser, waarbij bv. elke golflengte apart gemoduleerd wordt aan hoge snelheid.

Het ontwerp van de DFB laser werd in het kader van het doctoraat geoptimaliseerd voor het bekomen van een hoge directe modulatiebandbreedte. In het tweede hoofdstuk, met de theoretische beschouwingen, wordt uitgelegd hoe het modulatieantwoord van een geïsoleerde DFB laser een tweede-orde transfertfunctie is. De bandbreedte wordt vooral bepaald door de DC stroom en door de modale differentiële winst (de verandering van de versterking per lengte-eenheid met de geïnjecteerde ladingsdragersdichtheid). In actieve materialen bestaande uit zgn. strained layer quantum wells kan die modale differentiële winst gemaximaliseerd worden door de caviteitsverliezen te minimaliseren en door een sterke overlap tussen de lasermode en de actieve laag te realiseren. Lage caviteitsverliezen worden bekomen met een zo dun mogelijke bondingslaag (een BCB lijm) om een zo sterk mogelijke werking van het diffractierooster te bekomen. Er wordt ook aangetoond dat de introductie van

externe reflecties op welbepaalde afstanden van de laser toelaat om een foton-fotonresonantie te verkrijgen in het modulatieantwoord en zo de bandbreedte verder te verhogen.

De fabricatieprocessen worden uitvoerig uit de doeken gedaan in het derde hoofdstuk. Alles begint met de fabricatie van het silicium-op-oxide (SOI: silicon on insulator) deel. Deze golfgeleiders en mogelijke diffractieroosters worden in de onderzoeksgroep ontworpen, maar de fabricatie ervan gebeurt bij IMEC dmv. diep-UV lithografie en droge etsprocessen. Daarna wordt de InP epitaxiaalstructuur gebonden op dit SOI: het DVS-BCB polymeer wordt gesponnen op het SOI zodat een heel dunne laag van het polymeer over het SOI verspreid is en het InP wordt er op gekleefd. Na het verwijderen van het InP-substraat wordt begonnen met de processing (opnieuw lithografie en etsen) van de InP structuur zodat uiteindelijk een geometrie bekomen wordt zoals in onderstaande figuur.
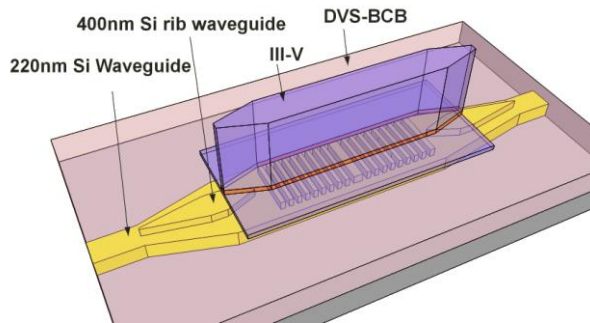
Figuur 1: Typical Schema van een heterogeen geïntegreerde III-V op silicium DFB laser.

Het laatste hoofdstuk van het doctoraat omvat alle belangrijke meetresultaten. Diverse laserdiodes, met InGaAsP of InAlGaAs actieve lagen, met en zonder externe caviteit, werden gefabriceerd en gekarakteriseerd. Eerst worden enkele statische karakteristieken, zoals uitgangsvermogen en spanning versus geïnjecteerde stroom en optisch spectrum, opgemeten. Uit de spanning versus de stroom kan men de serieweerstand halen, terwijl het optisch spectrum toont hoe sterk de laser monomodaal is. Het optisch spectrum van DFB lasers vertoont ook een zgn. stopband en uit de breedte hiervan kan men besluiten hoe sterk de werking van het diffractierooster is. Er worden uitgangsvermogens gemeten van 6 mW (in de silicium golfgeleider) en serieweerstanden van minder dan 10 Ohm. De meeste optische spectra vertonen een brede stopband, corresponderend met een waarde van de koppelingscoëfficiënt van het diffractierooster van 135 tot 200 cm-1.

Na deze statische metingen wordt gekeken naar het kleinsignaal-modulatieantwoord als functie van de modulatiefrequentie. Dit wordt opgemeten met behulp van een netwerk-analyser en een fotodiode (ontvanger) met heel hoge bandbreedte. Aan de hand van dit modulatieantwoord kan al geschat worden wat de maximale bitsnelheid zal zijn bij grootsignaalmodulatie (bv. on-off keying). De hoogste modulatiebandbreedtes werden gemeten voor de lasers met InAlGaAs actieve lagen (actieve lagen bestaande uit 8 quantum wells). Bij verschillende van die lasers is de bandbreedte ook merkbaar hoger door het optreden van een foton-fotonresonantie. Er werd een maximale bandbreedte van 27 GHz gemeten.

Na de kleinsignaalmetingen werden experimenten uitgevoerd met grootsignaalmodulatie, bv. aan-uit modulatie en pulse amplitude modulatie met 4 niveaus (PAM-4). De kwaliteit van de optische gemoduleerde signalen kan afgeleid worden van oogdiagrammen en bitfoutprobabiliteiten kunnen gemeten worden met een bit-error-rate testset. Daarbij kan men het gemoduleerde optische signaal onmiddellijk detecteren met een optische ontvanger, of het eerst over een aantal km glasvezel sturen in een linkexperiment. Verschillende bitrates en transmissie over verschillende afstanden werden onderzocht. Voor Non Return to Zero On-Off-Keying (NRZ-OOK) werd een maximale bitrate van 40 Gbit/s gedemonstreerd. Voor voldoende kleine woordlengtes werd bij deze bitrate zelfs foutvrije transmissie over 2 km glasvezel aangetoond. Oogdiagrammen voor deze bitsnelheid zijn hieronder te zien, bovenaan voor een woordlengte van 2^7-1 en onderaan voor een woordlengte van 2^{31}-1. Links zijn de oogdiagrammen onmiddellijk na de laser en rechts zijn de diagrammen na transmissie over 2 km vezel.
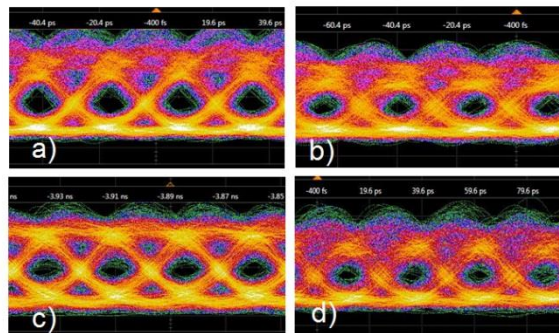
Figuur 2: 40 Gb / s directe modulatie van een heterogeen geïntegreerde DFB laser, voor een PRBS lengte van 2^7-1 voor back-to-back (a) en na 2 km vezel (b), en hetzelfde voor een lengte van 2^{31} -1 (c, d).

Naast on-off-keying werden ook speciale modulatieformaten zoals duobinary en PAM-4 geprobeerd en met beide formaten werd ook 40 Gbit/s aangetoond. Tenslotte werd ook chirp managed transmision onderzocht. Hierbij wordt de

parasitaire frequentiemodulatie (chirp genoemd) door middel van een optisch filter omgezet in extra intensiteitsmodulatie. Bovendien wordt ook het optische spectrum na het filter iets smaller, zodat er minder problemen zijn met de dispersie in de glasvezel. Op die manier kon ook foutvrije transmissie van een 28 Gbit/s signaal over 21 km glasvezel gedemonstreerd worden.

Modale winst van meer dan 100 cm^{-1} in (100/55/100 nm) SiN/QD/SiN structuren werd bekomen. Een identieke lagenstack werd dan gebruikt voor de fabricage van microdisks. Eerst toonde een kwantitatieve studie van de disk modes en hun verliezen aan dat lasing in principe mogelijk moest zijn, gezien de haalbare winst in deze stack. Wanneer we de disk pompten met een picoseconde laser konden we dan ook effectief laserwerking demonsteren, bij kamertemperatuur en met heel lage drempel (27 μJ·cm^{-2} voor 7 μm diameter disk). Een uitgebreide karakterisatie van de spectrale, temporele en coherentie eigenschappen werd uitgevoerd. De resultaten tonen aan dat golflengteafstembare colloïdale QDs de basis kunnen vormen voor een versatiel SiN-golfgeleiderplatform. Dit opent perspectieven voor zowel praktische applicaties als fundamenteel onderzoek in kwantumemitters en kwantum elektrodynamica.

English summary

Optical interconnects are becoming increasingly important for the information society. Before, optical fiber communication was mainly used for the transmission of data over long distances (10 km and more). But since a few years optical fiber communication is used also for interconnections over shorter distances, e. g. a few hundred meters. The distances where optical interconnects are introduced become shorter as the bit rates increase. The reason is that the transmission losses of copper cables increase strongly with the bit rate while the transmission losses of optical fibers are low irrespective of the bit rate.

Nowadays ever larger amounts of data are stored in data centers and both data processing and logical operations are fully implemented in the data center. Interconnections with very high bit rates are needed to exchange the massive amount of data between the different servers of the data center. At present, bit rates of 100 Gb/s are used, but there is also a standard in preparation for 400 Gb/s interconnects and big companies like Facebook and Google are even asking for a Tb/s standard.

The generation of the optical data at the transmitter side of the interconnect can be realized in a variety of ways. One can use a laser diode with a constant optical output power and modulate the intensity using an external (intensity) modulator. Such modulators have the advantage of a low parasitic frequency modulation, which is especially an advantage for communication over longer distances, but they have the disadvantage of a larger footprint and because of high coupling loss they require a larger laser power. For shorter distances, one can also use a directly modulated laser diode, whereby the output power of the laser diode is modulated by modulating the electrical current injected into the laser diode. This can usually be done with lower power consumption than for external modulation, but it is not easy to achieve the desired bit rates.

In addition, there is a strong tendency to develop silicon-based photonic integrated circuits. This technology has the advantage that one can reuse the advanced manufacturing methods from microelectronics for the fabrication of photonic integrated circuits. And there is a possibility to co-integrate electronics with photonics. In this technology (which is actually a silicon-on-insulator platform) very compact passive waveguide components (e. g. optical filters, multiplexers, etc.) can be realized. However, silicon has the disadvantage that it is not suitable for the fabrication of light sources (LED's or laser diodes) because of its indirect band-gap.

In recent years, a significant activity has started on the bonding of III-V materials on silicon-on-insulator (SOI) waveguide circuits, a.o. in the Photonics

Research Group of Ghent University. Membranes consisting of several thin layers of InP, InGaAs, InGaAsP, InAlGaAs can now be bonded with high yield on the SOI substrate. III-V materials are well suited for the realization of laser diodes. Semiconductor lasers can thus be fabricated on SOI by simple post-processing of the bonded membranes.

In this PhD, we continued on earlier work on a heterogeneously integrated DFB laser diode. DFB (distributed feedback) laser diodes are the light sources that are traditionally used for optical fiber communication. They emit light with high spectral purity due to a diffraction grating that is embedded in the laser structure. For the heterogeneously integrated DFB laser, the diffraction grating can be etched into the silicon waveguide, something which makes the processing on the InP membranes considerably easier. In our heterogeneously integrated DFB laser diodes, the light is largely concentrated in the InP membrane. As a result, a large overlap is obtained between the laser mode and the active layer, the layer that is responsible for the amplification. The light couples to the silicon waveguides at both ends of the laser by means of two tapers, after which it can propagate further in the silicon waveguide. In principle, multiple laser diodes can be integrated together in this way to form a multi-wavelength laser, of which each wavelength is modulated separately at high speed.

The design of the DFB laser has been optimized in the context of this PhD to obtain a high direct modulation bandwidth. In the second chapter, with the theoretical considerations, it is explained how the modulation response of a DFB laser is a second order transfer function. The bandwidth of the laser is mainly determined by the DC current and by the differential modal gain (the change of the gain felt by the laser mode per unit length with the injected carrier density). For active materials consisting of so-called strained layer quantum wells, the modal differential gain is maximized by minimizing the cavity loss and also by establishing a strong overlap between laser mode and the active layer. Low cavity loss can be obtained by a thin bonding layer (a BCB adhesive) in order to obtain a strong effect from the diffraction grating. It is also shown that introducing an external reflection at well-defined distances from the laser allows realizing a photon-photon resonance in the modulation response, which can further increase the bandwidth.

The manufacturing processes are thoroughly explained in the third chapter. The process starts with the fabrication of the silicon-on-insulator circuit. The waveguides and diffraction gratings are designed in the Photonics Research Group, but manufacturing is done at IMEC facilities using deep UV lithography and dry etching. After that, the InP epitaxial structure is bonded to this SOI. For the purpose of bonding, a very thin layer of DVS-BCB polymer is spin coated on the SOI and the III-V materials are machine bonded on it. After the removal of the InP substrate, the processing steps such as lithography, etching, deposition and metallization follow so that a geometry which is shown in the figure below is fabricated.
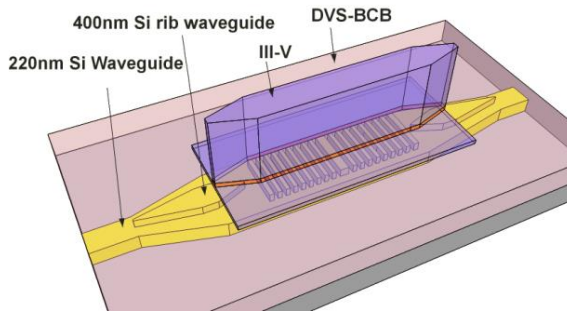
Figure 1: Schematic of a heterogeneously integrated III-V-on-silicon DFB laser.

The final chapter of the doctoral thesis covers all key measurements. Several laser diodes, with InGaAsP or InAlGaAs active layers, with and without external cavity, were fabricated and characterized. First, some static characteristics such as output power and voltage versus injected current and optical spectrum were measured. From the voltage versus the current curve, one can extract the series resistance, while the optical spectrum shows how well the laser operates in a single mode. The optical spectrum of DFB lasers also exhibits a so-called stop band and from the width of this stop band one can evaluate the strength of the diffraction grating. We measured output powers as high as 6 mW (in the silicon waveguide) and series resistances of less than 10 Ω. Most optical spectra show a broad stop band, corresponding to a value of the coupling coefficient of 135 to 200 cm^{-1}.

After these static measurements we measured the small-signal modulation response. This is measured with the aid of a network analyzer and a photodiode (receiver) with very high bandwidth.

The highest modulation bandwidths were measured for the InAlGaAs lasers with active layers consisting of 8 quantum wells. The higher bandwidth of these lasers is due to the occurrence of a photon-photon resonance. A maximum bandwidth of 27 GHz was measured.

After the small signal measurements, experiments were carried out with a large signal modulation, e. g. on-off modulation and pulse amplitude modulation with 4 levels (PAM-4). The quality of the optical modulated signals can be derived from eye diagrams and also from a bit error rate measurement with a BER test set. The modulated signals can be detected by an optical receiver in a back-to-back configuration (without an optical fiber), or after transmission over a few km of a fiber. For non-return to zero on-off-keying (NRZ-OOK) a maximum bit rate of 40 Gb/s has been demonstrated. For sufficiently small word lengths an error-free transmission over 2 km of fiber has been shown at this bitrate. Eye diagrams for this bit rate are given below, at the top row for a word length of 2^7-1, and at the bottom row for a word length of 2^{31}-1. The eyes on the left hand side are from the back-to-back measurements and the ones on the right hand side are after transmission over 2 km fiber.

In addition to the on-off keying, special modulation formats such as electrical duobinary and PAM-4 have been demonstrated both at 40 Gb/s.

Finally chirp managed transmission was also examined. The parasitic frequency modulation (chirp) which accompanies the intensity modulation in a directly modulated laser can be exploited by means of an optical filter to convert FM into additional IM modulation. In addition, the optical spectrum after the filter becomes slightly narrower, so that there are fewer problems with the dispersion in the optical fiber. In this way, an error-free transmission of 28 Gb/s NRZ-OOK has been demonstrated over 20 km of a standard single mode fiber.
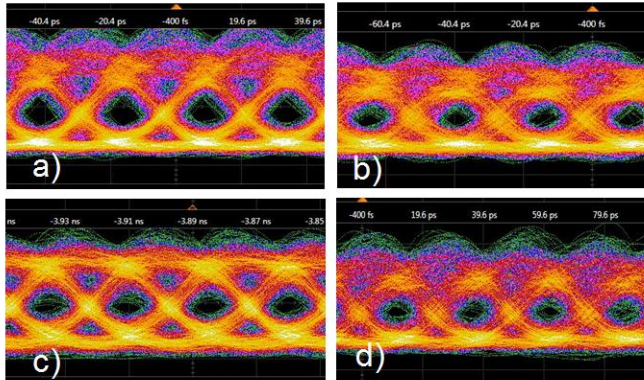
Figure 2: 40 Gb/s direct modulation of a heterogeneously integrated DFB laser, for a PRBS length of 2^7-1 for back-to-back (a) and after 2 km fiber (b), and the same for a length of 2^{31}-1 (c,d).

1

Introduction

1.1 Introduction of research background

There used to be an era where people only had access to radios or telegraphs to get news over long distances. The communication systems were slow, vulnerable to noise, costly and with low capacity. It took years of research for scientists to overcome all obstacles to reach where we are now. Nowadays ultrafast internet connections are available almost everywhere on the earth. Part of this progress is indebted to microelectronics and the development of very fast and ultra-compact electronic circuits for communication systems. Another part is due to the introduction of photonics and optical fiber technology.

Today, the impact of photonics technology on our daily life is impressive. Microphotonic devices are emerging in all high-tech areas such as sensing [1], medical applications [2], space technology [3] and data transmission [4, 5]. In the communication field, the invention of the semiconductor laser [6, 7] and the steep reduction of the optical fiber loss [8] initiated the research on optical fiber communication. This revolutionized data transmission in the twentieth century.

Optical fiber has been dominating long distance communications for several decades (Figure 1.1). Nowadays, long distance optical links are based on coherent communication and carry information over oceans with a huge capacity (tens of Tb/s) [9, 10]. This technology keeps advancing to meet ever more stringent requirements for bandwidth and power consumption. Just in June 2016, for example, Google announced a new undersea fiber-optic cable between USA and Japan over 5600 miles that can theoretically carry as much as 60 Tb/s.

Figure 1.1: Optical fiber connection map.

As the data volumes generated and transmitted worldwide are exponentially increasing, the processing of this data becomes another challenge. Inside datacenters, where all this data is stored and processed, multi core electronic ICs are responsible for all the processing. These circuits need to communicate with each other during processing. They can be located in one rack or in different racks and can be separated by distances of a few tens of cm up to a few km. The link speeds (tens of Gb/s) are so high that metal lines are very lossy and unsuitable even for relatively short distances [11, 12]. This limitation motivated researchers to study optical interconnects. However, for these cases, the coherent communication is too complex and costly. Leveraging photonics for the data transmission will improve speed and power consumption in interconnects, especially in the shorter links. In the next section, optical interconnects will be introduced briefly.

1.2   Optical interconnects

It has been anticipated that bandwidth hungry systems such as cloud computing and other emerging web applications will create the need for more powerful warehouse-scale data centers. These data centers comprise hundreds of thousands of servers that need to communicate with each other via high performance and low latency interconnection networks. The fundamental limitations of copper as an interconnect medium in terms of loss, dispersion, and crosstalk are becoming clear as interconnect density and speed is rocketing. Many of the interconnects in existing datacenters are already based on optical fiber, even single mode fiber, and several standards for optical interconnects have been defined or are being discussed.
The optical interconnects were so far mainly aimed at longer distance interconnects, e.g. between datacenters or between distant servers inside a datacenter, with distances going from a few hundred meter to several kilometers. The penetration of optical links into short and very short distances (for chip-to-chip or intra-chip interconnects) will then come over time, as the technology becomes more cost effective together with the increasing bandwidth

requirements. Optical interconnects provide high bandwidth, low power and low latency compared to traditional electrical interconnects. However, there are still challenges in exploiting the optical technology in real life applications. Temperature sensitivity, footprint and power consumption are the main issues. All-optical interconnects are a promising solution in order to significantly reduce power consumption [5, 13], but this technology is in its early stage and intense research is going on to improve the performance of such systems.

One realistic roadmap for optical interconnects is illustrated in Figure 1.2. It shows how optical interconnects are replacing copper interconnects in the communication distance versus volume frame. The optical interconnects are expanding their application domain from long haul and metro links to rack-to-rack links as bandwidths and power consumption for these links increase.
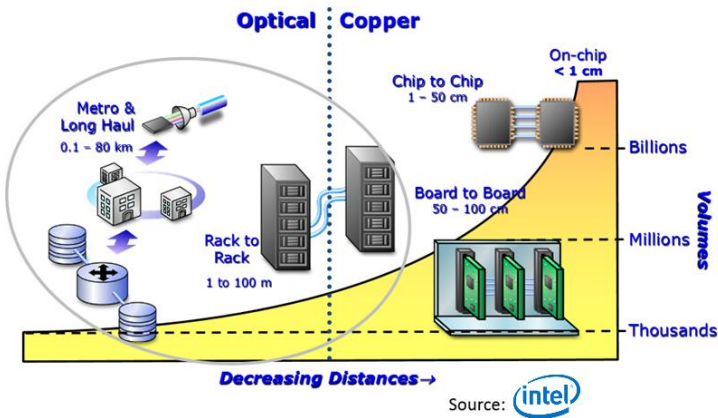
**Figure 1.2:** Optical interconnects roadmap in data communication networks.

In the typical optical interconnect, there is an optical transceiver which consists of two main parts: a transmitter and a receiver (Figure 1.3). In the transmitter, the processed data from one CPU will be modulated on the coherent light beams from lasers with different wavelengths. The light acts as a carrier signal for the data. Each wavelength can be modulated separately and corresponds with an optical channel. The modulation can be done directly (by modulating the current injected into the laser diodes) or externally, in a separate modulator. In each case, single mode, power efficient and integratable light sources are required. DFB lasers are interesting candidates for this application, since they more or less can address all the above requirements. Furthermore, these lasers can be directly modulated at high frequencies. A brief introduction about this kind of semiconductor laser will be presented in the next section.
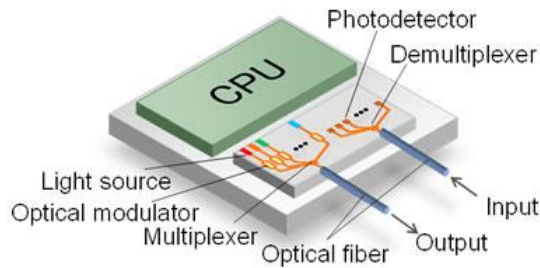
Figure 1.3: Typical optical transceiver schematic by Fujitsu.

1.3   DFB lasers

Distributed feedback (DFB) edge emitting laser diodes are the standard transmitters in most advanced optical communication systems. In contrast to other types of lasers, the feedback is distributed along the laser cavity by diffraction on a Bragg grating (Figure 1.4). The grating which normally is patterned on the cladding layers acts as a very selective optical filter integrated in the laser diode. The period of the grating determines the lasing wavelength and should be designed in order to position the lasing wavelength within the gain spectrum of the active material. For this type of laser, the suitable active materials are typically based on InP ternary and quaternary epitaxial structures such as InGaAsP and InGaAlAs.
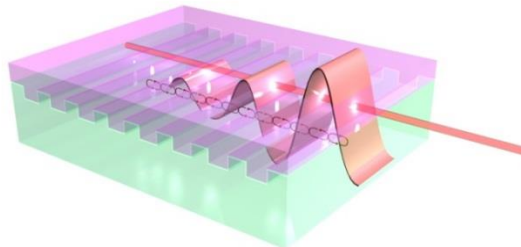
Figure 1.4: Schematic representation of a DFB laser by Adachi Lab.

DFB laser diodes with very high performance have been fabricated using InP-based epitaxial structures. Lasers with threshold currents as low as 5 mA, output powers as high as 100mW, and with very low noise (linewidths below 1 MHz and RIN below -150 dB/Hz) and very high modulation bandwidths (3 dB bandwidths above 20 GHz) have been demonstrated at both 1.3 and 1.55 μm wavelengths [14-17]. Electronic and thermal wavelength tuning over several tens of nm has also been achieved using special DFB or DBR (Distributed Bragg Reflector) lasers [18-20].

On the other hand, Si photonics has emerged as the leading candidate for photonic integrated circuits (PICs) due to the unique combination of potential low cost, performance enhancements due to the prospect of both photonic and electronic/photonic integration, as well as compatibility with the world's most successful electronic production technology, CMOS. Silicon-on-Insulator (SOI) is a platform that enables making very compact, high refractive index contrast photonics circuits. Numerous ultra-compact photonic passive devices have been demonstrated on this platform, from simple waveguides to complex filters (ring resonators, arrayed waveguide gratings (AWGs), echelle grating), multimode interference (MMI) couplers and grating couplers [20-22].

Active photonic components such as photodiodes [23, 24] and different types of modulators [25, 26] also can be fabricated in the Si photonics technology. Since Si has an indirect bandgap, making a laser source on this platform is not straightforward. Different methods such as direct growth of bandgap engineered Ge [27] or III-V materials [28] are proposed and few structures have been demonstrated, but the efficiency is still too low to be of practical interest. Electrically pumped efficient sources on silicon remain a challenge and an overview of the numerous efforts is presented in [29].

1.4   Heterogeneously integrated lasers

One practical method is to bond the active materials (InP) on the Si passive circuits (SOI). In this way, the interesting properties of both Si and III-V can be preserved in the integrated circuit. Heterogeneous integration of III-V materials gives the SOI platform access to the complete suite of high-speed and efficient III-V-based photonic components. Therefore, the integration of the III-V epitaxial structures with Si photonics has huge potential for optical communication.

This heterogeneously integration has been developed in the past decade and promising results have been reported. Two main schemes have been presented for heterogeneously integrated III-V/Si lasers with mWs of output power. The first is based on guiding in a silicon waveguide with evanescent coupling to the bonded III-V layer, as reported in [30]. The laser reported in [30], e.g., consists of a 700-nm-thick silicon waveguide under the III-V layer for light confinement and the evanescent field of the optical mode overlaps with the bonded III-V layers for light amplification. The second method is based on a structure in which the light is mainly confined to the III-V waveguide and is coupled to the silicon waveguide at the ends of the III-V waveguide through a 120-μm-long III-V tapering section [31, 32]. In the laser of [31], the top III-V channel waveguide and the bottom 500-nm-thick SOI rib waveguide are separated by a silicon dioxide (SiO2) interlayer. For the laser of [32], the single taper has been replaced by a double adiabatic coupler for improved coupling, and the III-V layers are bonded to 400-nm-thick SOI through a DVS-BCB adhesive layer. The double adiabatic taper has a total length of ~150 μm or even >200 μm, and the III-V and SOI waveguides are tapered in an opposite direction.

In this work, we explored the second method to fabricate a heterogeneously integrated DFB laser based on InP/Si technology for high speed applications. A III-V MQW epitaxial structure is bonded on Si passive rib waveguides using a DVS-BCB polymer. After bonding, the III-V processing continues with a few wet and dry etching steps together with lithography and metallization (Figure 1.5).

As is clear in the figure, two inverse adiabatic tapers are used to couple the light to the Si waveguide. By adjusting the bonding thickness, one can control the feedback strength of the grating. This provides a degree of freedom to design lasers with interesting characteristics (ultra-low linewidth [33] or short cavity DFB lasers [34]).
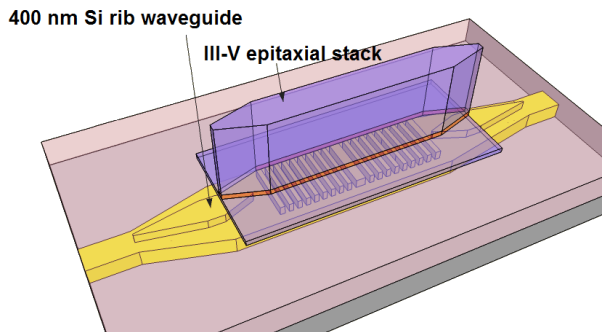

Figure 1.5: Schematic of a heterogeneously integrated DFB laser on Si waveguide.

These lasers can be directly modulated through a modulation of the injected current. In this case, two photonic components (laser and modulator) are merged into one device. This modulation technique reduces the photonic integrated circuit's complexity and can lead to a small footprint and lower power consumption.

1.5   Direct modulation

For short-reach applications, solutions that use intensity modulation and direct detection (IM/DD) are seen as more practical [35]. In this modulation configuration, just the light intensity is modulated in the transmitter. In the receiver, a fast photodiode is used to convert the optical power into electrical power. For a long time, NRZ-OOK (Non Return to Zero – On Off Keying) has been the dominant modulation format in IM/DD fiber-optical communication systems.

Intensity modulation can be obtained either by direct modulation (through modulation of the laser diode current, Figure 1.6-a) or by external modulation (either using electro-absorption or electro-refraction in an interferometer, Figure 1.6-b).
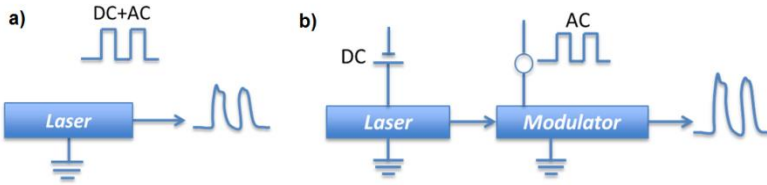
Figure 1.6: Schematic of an optical transmitter using a directly modulated laser (a) and using an external modulator (b)

Direct modulation of laser diodes for high-speed transceivers has significant advantages over the use of external modulators in terms of power consumption, fabrication complexity and compactness [36], especially for short distance optical interconnects. External MZ-based modulators require a long interaction length (~mm's), if a low drive voltage is desired. EAM based modulators suffer from substantial insertion loss, which implies using a higher power laser source to compensate the losses. External modulators are especially desired for longer distance optical communications since they give significantly less parasitic frequency modulation (chirp) and result in less problems with fiber dispersion.

The NRZ direct modulation scheme has been used since the inception of optical fiber communications. For example, in 1975, bit rates of 123 Mb/s and 400 Mb/s were reported using GaAlAs lasers emitting at a wavelength of 0.83 μm, graded index multi-mode fibers and Si avalanche photodiodes [37], [38]. In the past, optical fiber communications relied almost exclusively on directly modulated lasers until the bit rate was increased to and above 10 Gb/s. At such high speeds and for the long distances for which optical communication was typically used, the undesired frequency modulation (chirp) accompanying the direct intensity modulation becomes relatively large, resulting in severe fiber dispersion. For shorter distances, as in optical interconnects, chirp and fiber dispersion are less a problem and direct modulation is becoming increasingly popular for these applications.

Intensive research is now going on to enhance the maximum bitrate that can be transmitted using direct modulation of laser diodes. Recently, several DFB laser diodes have been reported at 1300 and 1550 nm that are capable of direct modulation up to 56 Gb/s [34, 39]. Mostly these lasers are based on the InP platform, but, as we discussed, Si photonics provides a better solution for large scale integrated circuits based on CMOS technology.
In Figure 1.7, we show two recently published heterogeneously integrated lasers that were used for direct modulation experiments. On the left (Figure 1.7-a,b), a hybrid DFB laser is shown which is integrated on a 500 nm thick device layer on the SOI substrate [40]. For a 200 μm device length, they measured a 12.5 Gb/s NRZ-OOK direct modulation. On the right (Figure 1.7-c,d), a hybrid III-V on Si tunable laser based on double ring resonators has been demonstrated [41].

With this design, they achieved 21.4 Gb/s direct modulation and discrete tuning over the C-band.
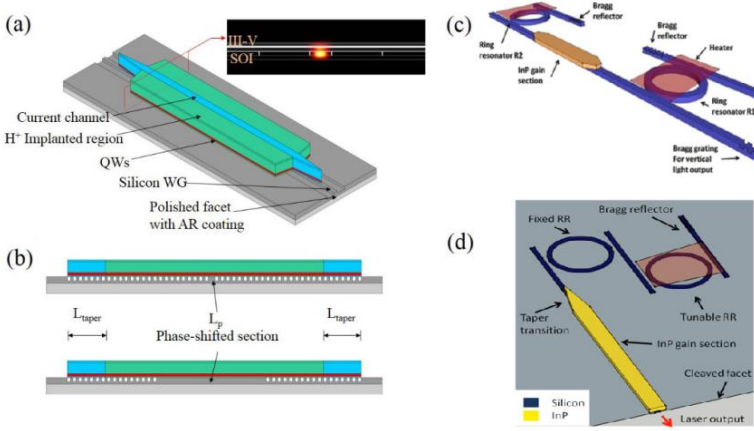
Figure 1.7: Illustration of (a) a hybrid DFB laser; (b) a schematic lateral view with a grating on the waveguide [40], schematic view of two hybrid III-V/Si laser designs with (c) vertical grating coupling (design 1) and with (d) cleaved facet coupling (design 2) [41].

1.6   Outline

This work consists of 3 chapters that each covers a different aspect of heterogeneously integrated III-V-on-Silicon DFB laser. Theoretical backgrounds about DFB lasers based on the rate equations and coupled mode theory are discussed in chapter 2. By using these equations the static and dynamic characteristics of the laser can be derived. Small signal and large signal behaviors of the laser are investigated. For directly modulated lasers, there are two important limitation factors (the modulation bandwidth and the link distance) which hinder the use of this type of lasers for communication systems. Tow techniques that have been used in this thesis to overcome these limitations are studied theoretically in chapter 2. An external feedback effect is used to extend the modulation bandwidth and chirp management is used to extend the reach distance.

Chapter 3 elaborates on fabrication aspect of these lasers. A standard process flow and a III-V epitaxial layer stack are presented in the beginning of this chapter. An optical design to realize the heterogeneous integration on the Si waveguide circuits is discussed. We have shown that the performance of the heterogeneously integrated DFB laser can be optimized by varying the bonding thickness. Coupling between the III-V active waveguide and the Si passive waveguide is also studied to realize an efficient optical power transmission.

Each processing step is briefly introduced and optimization for some of these steps are presented. Finally two epitaxial layer stacks that are used in this PhD thesis are introduced with their layer properties and the PL spectra.

Next, chapter 5 uses the theoretical and technical knowledge built up in the first two chapters to demonstrate a high speed directly modulated heterogeneously integrated DFB laser. The chapter starts with static characterization of different samples with different III-V epitaxial stacks. Two main structures were InGaAsP and InGaAlAs based QW epitaxial stack layers. Using the InGaAsP based DFB laser with 6 QWs, we have successfully demonstrated 28 Gb/s NRZ-OOK direct modulation and transmission over a 2 km long single mode fiber. This modulation speed has been improved to 40 Gb/s NRZ-OOK by using an InGaAlAs based DFB laser with 8 QWs and extended modulation bandwidth. This modulation bandwidth enhancement was realized by introducing an external reflector which creates a photon-photon resonance peak in the small signal response of the DFB laser.

In the rest of the chapter, two advanced modulation formats for short reach optical links are introduced. At 40 Gb/s we managed to successfully demonstrate 4-level Pulse Amplitude Modulation (PAM-4) and Electrical Duobinary (ED) modulation formats and their transmission over a 2 km single mode fiber. Finally a significant enhancement in the fiber link reach has been demonstrated using chirp management of the laser (CML). Putting the theoretical concepts into practice, a 28 Gb/s NRZ-OOK signal was sent over 20 km of a standard single mode fiber.

1.7 Reward & Publications

- **The Best Student Paper Award** (IEEE Photonics Society) in International Semiconductor Laser Conference (ISLC) for the paper "Enhanced Modulation Bandwidth of Heterogeneously Integrated III-V-on-silicon DFB Laser for 40 Gb/s NRZ-OOK Direct Modulation", Kobe, Japan, 2016.

Publications in international journals

1. A. Abbasi, S. Keyvaninia, J. Verbist, X. Yin, J. Bauwelinck, G. Roelkens, G. Morthier, "43 Gb/s Direct Modulation of a Heterogeneously Integrated InP/Si DFB Laser", (**invited**), Journal of Lightwave Technology (submitted).

2. A. Abbasi, C. Spatharakis, G. Kanakis, N. André, H. Louchet, A. Katumba, J. Verbist, H. Avramopoulos, P. Bienstman, X. Yin, J. Bauwelinck, G. Roelkens, G. Morthier,, "High speed direct modulation of a Heterogeneously Integrated InP/SOI DFB Laser", (**invited**), Journal of Lightwave Technology (2016).

3. S. Dhoore, L. Li, <u>A. Abbasi</u>, G. Roelkens, G. Morthier, "Demonstration of a discretely tunable III-V-on-silicon sampled grating DFB laser", IEEE Photonics Technology Letters, (2016).

4. <u>A. Abbasi</u>, J. Verbist, J. Van kerrebrouck, F. Lelarge, G. H. Duan, x. Yin, J. Bauwelinck, G. Roelkens, G. Morthier, "28 Gb/s Direct Modulation Heterogeneously Integrated C-band InP/SOI DFB Laser", Optics Express (2015).

5. G. Roelkens, <u>A. Abbasi</u>, P. Cardile, U.D. Dave, A. De Groote, Y. De Koninck, S. Dhoore, X. Fu, A. Gassenq, N. Hattasan, Q. Huang, S. Kumari, S. Keyvaninia, B. Kuyken, L. Li, P. Mechet, M. Muneeb, D. Sanchez, H. Shao, T. Spuesens, A. Subramanian, S. Uvin, M. Tassaert, K. Van Gasse, J. Verbist, R. Wang, Z. Wang, J. Van Campenhout, X. Yin, J. Bauwelinck, G. Morthier, R. Baets, D. Van Thourhout, "III-V-on-silicon photonic devices for optical communication and sensing", Photonics (**invited**), 2(3), p.969-1004 (2015).

6. <u>A. Abbasi</u>, G. Roelkens, G. Morthier, "Optimization of an Asymmetric DFB Laser Used as All-Optical Flip-Flop", IEEE Journal of Quantum Electronics, (2014).

Publications in international conferences

1. <u>A. Abbasi</u>, H. Chen, J. Verbist, X. Yin, J. Bauwelinck, G. Roelkens, and G. Morthier, "Chirp Managed Transmission over 20 km Standard Single Mode Fiber using a Directly Modulated Heterogeneously Integrated InP-on-Si DFB Laser Diode", OFC Conference , United States, (Submitted).

2. <u>A. Abbasi</u>, B. Moeneclaey, J. Verbist, X. Yin, J. Bauwelinck, G. Roelkens, and G. Morthier, "56 Gb/s Electro-Absorption Modulation of a Heterogeneously Integrated InP-on-Si DFB Laser Diode", OFC Conference , United States, (Submitted).

3. A. Rahim, <u>A. Abbasi</u>, N. André, A. Katumba, H. Louchet, K. Van Gasse, R. Baets, G. Morthier, G. Roelkens, "69 Gb/s DMT direct modulation of a Heterogeneously Integrated InP-on-Si DFB Laser**",** OFC Conference , United States, (Submitted).

4. <u>A. Abbasi</u>, H. Chen, J. Verbist, X. Yin, J. Bauwelinck, G. Roelkens, and G. Morthier, "Toward Si photonics based transceivers using directly modulated heterogeneously integrated DFB lasers", IEEE Photonics Society Benelux, Belgium, (2016).

5. K. Van Gasse, J. Van Kerrebrouck, <u>A. Abbasi</u>, G. Torfs, H. Chen, X. Yin, J. Bauwelinck, G. Roelkens, "480Mbps / 1 Gbps radio-over-fiber link based on a directly modulated III-V-on-Silicon DFB laser", International Topical Meeting on Microwave Photonics, France, (2016)

6. S. Dhoore, L. Li, <u>A. Abbasi</u>, G. Roelkens, G. Morthier, "Demonstration of a discretely tunable III-V/SOI sampled grating distributed feedback laser", IEEE Photonics Conference (IPC), United States, (2016).

7. G. Morthier, <u>A. Abbasi</u>, J. Verbist, S. Keyvaninia, X. Yin, F. Lelarge, G.H. Duan, J. Bauwelinck, G. Roelkens, "High-speed directly modulated heterogeneously integrated InP/Si DFB laser", (**invited**) European Conference on Optical Communication (ECOC), paper M2.E.1, Dusseldorf, Germany, (2016).

8. <u>A. Abbasi</u>, J. Verbist, X. Yin, F. Lelarge, G. H. Duan, J. Bauwelinck, G. Roelkens, G. Morthier, "Enhanced Modulation Bandwidth of Heterogeneously Integrated III-V-on-silicon DFB Laser for 40 Gb/s NRZ-OOK Direct Modulation", paper ThB4, International Semiconductor Laser Conference (ISLC), Sept. 2016, Kobe, Japan, (2016).

9. <u>A. Abbasi</u>, J. Verbist, X. Yin, F. Lelarge, G-H. Duan, J. Bauwelinck, G. Roelkens, G. Morthier, "Above 40 Gb/s Direct Modulation of a Heterogeneously integrated III-V-on-silicon DFB Laser", (**invited**) OSA-LAOP-2016, Medellin, Colombia, (2016).

10. G. Morthier, <u>A. Abbasi</u>, M. Shahin, J. Verbist, G. Roelkens, High speed modulation of InP membrane DFB laser diodes, (**invited**) Proceedings of ICTON (**invited**), Trento, Italy, (2016).

11. <u>A. Abbasi</u>, C. Spatharakis, G. Kanakis, N. S. André, H. Louchet, A. Katumba, J. Verbist, X. Yin, J. Bauwelinck, H. Avramopoulos, G. Roelkens, G. Morthier, "PAM-4 and Duobinary Direct Modulation of a Hybrid InP/SOI DFB Laser for 40 Gb/s Transmission over 2 km Single Mode Fiber", Optical Fiber Communication Conference (OFC), United States, p.M2C.6 (2016).

12. G. Roelkens, <u>A. Abbasi</u>, S. Keyvaninia, S. Uvin, K. Van Gasse, Z. Wang, U.D. Dave, B. Kuyken, G. Morthier, D. Van Thourhout, "III-V-on-silcon photonic integrated circuits for communication and sensing applications", 28th IEEE Photonics Conference (IPC 2015) (**invited**), United States, p.593-594 (2015).

13. <u>A. Abbasi</u>, J. Verbist, J. Van kerrebrouck, F. Lelarge, G. H. Duan, G. Roelkens, G. Morthier, "28 Gb/s Direct Modulation Heterogeneously Integrated InP/Si DFB Laser", European Conference on Optical Communication (ECOC), Spain, paper We.2.5.2 (2015).

14. G. Morthier, <u>A. Abbasi</u>, G. Roelkens, "Heterogenously integrated DFB and DBR membrane lasers for high speed direct modulation", ICOCN (**invited**), China, (2015).

15. <u>A. Abbasi</u>, G. Roelkens, G. Morthier, "Numerical Study of a 10 GHz Optical Flip-Flop Based on a Short Asymmetric DFB Laser" , Conference on Lasers and Electro-Optics (CLEO), United States, p.paper JTh2A.33 (2015) .

16. G. Roelkens, S. Keyvaninia, Y. De Koninck, S. Uvin, <u>A. Abbasi</u>, K. Van Gasse, Z. Wang, G. Morthier, D. Van Thourhout, R. Baets, "III-V-on-silicon photonic integrated circuits for optical interconnects", IEEE Summer Topicals (**invited**), Bahamas, p.TuC2.1 (2015) .

17. H. Shao, M. Vanwolleghem, G. Ducourneau, S. Keyvaninia, <u>A. Abbasi</u>, G. Roelkens, J.F. Lampin, "Narrowband THz generation through optical heterodyning of a dual wavelength heterogeneously integrated III-V/silicon DFB laser", Terahertz Science and Technology 2014, Italy, (2014).

18. <u>A. Abbasi</u>, S. Keyvaninia, G. Roelkens, G. Morthier, "Fast Phase Shifted asymmetrical DFB laser for all-optical flip-flop operation", IEEE Photonics Society Benelux, Netherlands, (2013).

References

[1] N. M. Jokerst, L. Luan, S. Palit, M. Royal, S. Dhar, M. Brooke and T. Talmage, "Progress in chip-scale photonic sensing", IEEE Trans. Biomedical Circuits and Sys., vol. 3, pp. 202-211, (2009).

[2] K. Zinoviev, L. G.Carrascosa, J.Sánchez del Río, B.Sepúlveda, C. Domínguez, and L. M.Lechuga, "Silicon Photonic Biosensors for Lab-on-a-Chip Applications," Advances in Optical Technologies, vol. 2008, Article ID 383927, 6 pages, (2008).

[3] N. Karafolas, J. M. P. Armengol and I. Mckenzie, "Introducing photonics in spacecraft engineering: ESA's strategic approach", IEEE Aerospace conference, Big Sky, MT, , pp. 1-15, (2009).

[4] G.T. Reed, G. Mashanovich, F. Y. Garde and D. J. Thomson, "Silicon optical modulators", Nature photonics vol 4(8), pp. 518-526, (2010).

[5] V. Almeida, C. A. Barrios, R. R. Panepucci and M. Lipson,. "All-optical control of light on a silicon chip", Nature vol. 431(7012),pp. 1081-1084, (2004).

[6] W. Cho and, S. Koch, "Semiconductor-Laser Fundamentals: Physics of the Gain Materials", Springer (2013).

[7] G. P. Agrawal and N. K. Dutta, "Semiconductor Lasers". Springer, (2001).

[8] K. C. Kao, and G. A. Hockham, "Dielectric-fibre surface waveguides for optical frequencies", Proceedings of the Institution of Electrical Engineers- London, vol.113(7), pp.1151–1158, (1966).

[9] A. H. Gnauck and P. J. Winzer, "Optical Phase-Shift-Keyed Transmission", Journal of Lightwave Technol, Vol. 23, pp.115-129, (2005).

[10] Ma, Y., Yang, Q., Tang, Y., Chen, S. and Shieh, W, "1-Tb/s Single-channel coherent optical OFDM transmission over 600-km SSMF fiber with subwavelength bandwidth access", Optics Express,vol. 17,pp. 9421– 9427, (2009).

[11] G. Roelkens, L. Liu, D. Liang, R. Jones, A. W. Fang, B. Koch, and J. E. Bowers, "III‑V/silicon Photonics for on‑chip and intra‑chip optical interconnects", Laser & Photonics Reviews, vol 4(6),pp. 751-779, (2010).

[12] D. Miller "Rationale and challenges for optical interconnects to electronic chips", Proceedings of the IEEE 88.6, pp. 728-749, (2000).

[13] L. Liu, R. Kumar, K. Huybrechts, T. Spuesens, G. Roelkens, E. Geluk, T. Vries, P. Regreny, D. Van Thourhout, R. Baets and G. Morthier,"An ultra-small, low-power, all-optical flip-flop memory on a silicon chip", Nature Photonics vol. 4(3), pp. 182-187, (2010).

[14] T. R. Chen, J. Ungar, J. Iannelli, S. Oh, H. Luong and N. Bar-Chaim, "High power operation of InGaAsP/InP multiquantum well DFB lasers at 1.55 μm wavelength", Electronics Letters, vol. 32(10), pp. 898, (1996).

[15] M. Faugeron, M. Tran, F. Lelarge, M. Chtioui, Y. Robert, E. Vinet, A. Enard, J. Jacquet, and F. Van Dijk, "High-Power, Low RIN 1.55 μm Directly Modulated DFB Lasers for Analog Signal Transmission", IEEE Photonics Technology Letters, vol. 24(2), pp. 116-118, (2012).

[16] J.-R. Burie, G. Beuchet, M. Mimoun, P. Pagnod-Rossiaux, B. Ligat, J. C. Bertreux, J.-M. Rousselet, J. Dufour, P. Rougeolle, F. Laruelle,"Ultra high power, ultra-low RIN up to 20 GHz 1.55 μm DFB AlGaInAsP laser for analog applications", Proc. SPIE, (2010).

[17] L. Coldren, "Monolithic tunable diode lasers." IEEE Journal of Selected Topics in Quantum Electronics vol.6(6), pp. 988-999, (2000).

[18] M. Müller, M. Kamp, A. Forchel and J.-L. Gentner,. "Wide-range-tunable laterally coupled distributed feedback lasers based on InGaAsP– InP", Applied Physics Letters, vol. 79(17), pp. 2684-2686, (2001).

[19] B. Mason "Widely tunable sampled grating DBR laser with integrated electroabsorption modulator", IEEE Photonics Technology Letters, vol. 11(6),pp. 638-640, (1999).

[20] M. Asghari and Ashok V. Krishnamoorthy. "Silicon photonics: Energy-efficient communication", Nature photonics vol. 5(5),pp. 268-270, (2011).

[21] G.T. Reed and Andrew P. Knights. "Silicon photonics." West Sussex, England: John Wiley and Sons, Ltd, (2004).

[22] B. Jalali, and Sasan Fathpour, "Silicon photonics", Journal of lightwave technology, vol. 24(12), pp. 4600-4615, (2006).

[23] L.Vivien1, J. Osmond1, J. Fédéli, D. Marris-Morini1, P. Crozat1, J. Damlencourt, E. Cassan1 , Y.Lecunff, S. Laval1, "42 GHz pin Germanium photodetector integrated in a silicon-on-insulator waveguide", Optics express vol. 17(8), pp. 6252-6257, (2009).

[24] H. Chen, P. Verheyen, P. De Heyn, G. Lepage, J. De Coster, S. Balakrishnan, P. Absil, W. Yao, L. Shen, G. Roelkens, and J. Van Campenhout, "1 V bias 67 GHz bandwidth Si-contacted germanium waveguide pin photodetector for optical links at 56 Gbps and beyond", Optics Express, vol. 24(5), pp. 4622-4631, (2016).

[25] S. Ashwyn Srinivasan, M. Pantouvaki, S. Gupta, H. Chen, P. Verheyen, G. Lepage, G. Roelkens, K. Saraswat, D. Van Thourhout, P. Absil, and J. Van Campenhout, "56 Gb/s germanium waveguide electro-absorption modulator", Journal of Lightwave Technology, vol. 34(2), pp. 419-424, (2016).

[26] D. Petousi, L. Zimmermann, A. Gajda, M. Kroh, K. Voigt, G. Winzer, B. Tillack, and K. Petermann, , "Analysis of optical and electrical tradeoffs of traveling-wave depletion-type Si Mach–Zehnder modulators for high-speed operation", IEEE Journal of Selected Topics in Quantum Electronics, vol. 21(4), pp. 199-206, (2015).

[27] S. Wirthsand D. Grutzmacher, "Lasing in direct-bandgap GeSn alloy grown on Si", Nature photonics, vol. 9(2), pp. 88-92, (2015).

[28] Z. Wang, B. Tian, M. Pantouvaki, W. Guo, P. Apsil, J. Van Compenhout, C. Merckling, D. Van Thourhout, "Room-temperature InP distributed feedback laser array directly grown on silicon", Nature Photonics, vol.9(12), pp. 837-842, (2015).

[29] S. Wirths and D. Grutzmacher, "Lasing in direct-bandgap GeSn alloy grown on Si." Nature photonics, vol 9(2), pp. 88-92, (2015).

[30] J. Pu, K. P. Lim, D. Keh Ting Ng, V. Krishnamurthy, C. Wei Lee, K. Tang, A. Yew Seng Kay, T. Hoe Loh, and Q. Wang, "Heterogeneously integrated III-V laser on thin SOI with compact optical vertical interconnect access" Optics letters, vol. 40(7), pp. 1378-1381, (2015).

[31] B. Ben Bakir, A. Descos, N. Olivier, D. Bordel, P. Grosse, E. Augendre, L. Fulbert, and J. M. Fedeli "Electrically driven hybrid Si/III-V Fabry-Pérot lasers based on adiabatic mode transformers", Optics express, vol. 19(11), pp. 10317-10325, (2011).

[32] S. Keyvaninia, G. Roelkens, D. Van Thourhout, C. Jany, M. Lamponi, A. Le Liepvre, F. Lelarge, D. Make, G. Duan, D, Bordel, and J. Fedeli, "Demonstration of a heterogeneously integrated III-V/SOI single wavelength tunable laser" Optics express, vol 21(3), pp. 3784-3792, (2013).

[33] A. Yariv, "Rethinking and Redesigning the Semiconductor Laser/ Quantum Noise Controlled Semiconductor Lasers", OFC, (2016).

[34] Y. Matsui, T. Pham, W. Ling, R. Schatz, G. Carey, H. Daghighian, T. Sudo, and C. Roxlo, "55-GHz Bandwidth Short-Cavity Distributed Reflector Laser and its Application to 112-Gb/s PAM-4", OFC, (2016).

[35] J. Cartledge and A. S. Karar, "100 Gb/s intensity modulation and direct detection", Journal of Lightwave Technology, vol. 32(16), pp.2809-2814, (2014).

[36] R. S. Tucker, "Green Optical Communications – Part I: Energy Limitations in Transport", IEEE Journal of Selected Topics in Quantum Electronics, vol. 17, pp. 245-260, (2011).

[37] K. Kurokawa, "A 400 Mb/s experimental transmission system using graded index fiber, Optical fiber communications", (1975).

[38] T. Uchida, S. Sugimoto, A. Ueki, T. Usui, S. Ishihara, and I. Kitano, "An experimental 123 Mb/s fiber-optic communication system", Optical Fiber Transmission, OSA Technical Digest, (1975).

[39] Y. Matsui, T. Pham, T. Sudo, G. Carey, B. Young, J. Xu, C. Cole and Charles Roxlo "28-Gbaud PAM4 and 56-Gb/s NRZ performance comparison using 1310-nm Al- BH DFB laser", Journal of Lightwave Technology, vol. 34(11), pp. 2677-2683, (2016).

[40] C. Zhang, S. Srinivasan, Y. Tang, MJR Heck, ML Davenport, and JE Bowers, "Low threshold and high speed short cavity distributed feedback hybrid silicon lasers, Optics Express, vol. 22(9), pp. 10202–10209, (2014).

[41] G. de Valicourt, G. Levaufre, Y. Pointurier, A. Le Liepvre, J.-C. Antona, C. Jany, A. Accard, F. Lelarge, D. Make, and G.-H. Duan, "Direct Modulation of Hybrid-Integrated InP/Si Transmitters for Short and Long Reach Access Network", Journal of Lightwave Technol, vol. 33(8), pp. 1608–1616, (2015).

<div style="text-align: right; font-size: 4em;">**2**</div>

Theory of directly modulated DFB laser diode

Distributed feedback (DFB) laser diodes are the transmitter of choice in most advanced optical communication systems. Numerous advantages of a DFB laser diode over other laser types such as their stable single-mode spectrum, high output power, integration compatibility and low noise operation make it an attractive source for many applications. In this chapter, the theoretical background of high speed DFB lasers will be presented in detail.

We will start with a brief introduction on semiconductor laser diodes. The basic properties of DFB laser diodes are discussed via rate equations and coupled mode equations. The lasers' high speed characteristics can be obtained after linearization of the rate equations. The most important parameters in order to enhance the modulation bandwidth are examined. A method to extend the reach of a link based on a directly modulated DFB laser is described as well.

2.1 Introduction to distributed feedback laser diodes

In general laser operation needs a gain material in combination with a feedback mechanism. The feedback mechanism uses a resonator that brings back part of the optical field passing through a given point to the same point repeatedly. For specific frequencies, the optical path length of each round trip inside the resonator will be equal to an integer number of wavelengths. Then the fields will add up in phase and are amplified through the process of stimulated emission. This leads to the generation of a coherent and collimated light beam [1, 2].

The gain material inside the resonator determines the type of laser. For example, a CO_2 laser is a gas laser which consists of a cylinder tube filled with a mixture

of a few gases (CO_2, N_2 and He) with two mirrors at each side of the tube that serve as a resonator [3]. In this thesis, we will restrict ourselves to semiconductor materials. First semiconductor lasers were demonstrated almost simultaneously by four different groups in 1962 [4-7]. Light emission in a semiconductor material occurs when an excited electron in the conduction band recombines with a hole in the valence band [1, 2]. During this process both energy and momentum should be conserved. The energy difference between these two states will determine the energy of the emitted photon (energy conservation). Conservation of the momentum on the other hand, implies that materials with a direct band gap should be used for this purpose. These direct band gap materials are typically III-V semiconductor compounds (such as AlGaAs, InGaAs and InGaAsP). The band gap can be adjusted by varying the material composition of ternary and quaternary compounds, which enables varying the operating wavelength and thereby to cover most of the visible, near-infrared and mid-infrared spectral range.

Since these lasers can directly convert electrical power to optical power, they have been employed in various interesting applications in communication systems. In addition, their small footprint makes them suitable for use in high speed and low energy consumption photonic integrated circuits.

A simple Fabry-Perot laser with two cleaved facets, which act as optical mirrors, can lase in multiple longitudinal modes (Figure 2.1). The wavelengths λ of these longitudinal modes satisfy the following phase condition:

$$m\lambda = 2n_e(\lambda)L \tag{2.1}$$

with L the length of the cavity and $n_e(\lambda)$ the effective refractive index.

The spectral width of the gain material normally covers multiple longitudinal modes, which results in a lasing spectrum with different peaks (multimode operation). The existence of multiple longitudinal modes limits the use of Fabry-Pérot lasers for communication applications because of chromatic dispersion effects in optical fibers.

The requirement for a low noise, high power and single mode laser is met by a DFB laser. The modified cavity of the DFB laser assures single mode lasing. In this type of laser diode, the feedback structure is distributed along the laser cavity instead of being two discrete mirrors (Figure 2.2).
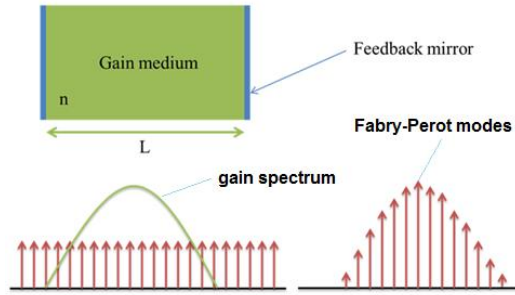
Figure 2.1: Schematic representation of a Fabry-Pérot laser cavity with its lasing spectrum.

This is realized by a periodic variation of the thickness or width of a waveguide layer (most commonly a cladding layer), introducing a periodic change in the effective refractive index. Subsequent reflections on these layers will generate a coupling between forward and backward propagating waves in a similar way as the reflections at the end facets in a Fabry-Pérot structure. Since the period of these effective index variations is of the order of a few hundred nm, the free spectral range will be much broader than the gain profile of the materials. In this way the laser can operate in a single longitudinal mode. Wavelength tuning can be achieved by slightly changing the period of the grating or the effective index of the waveguide.
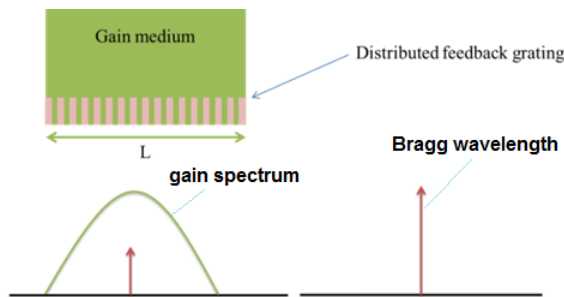
Figure 2.2: Schematic representation of a DFB laser cavity with its lasing spectrum.

This type of laser was proposed in the early seventies [8, 9]. The first experimental demonstrations were performed using optically pumped devices [10, 11] at low temperature and later on, also with electrically pumped devices having a single [12] and double heterostructure [13]. After extensive research during the 1980s, DFB laser diodes have become the main optical source in fiber-based telecommunication systems and their properties have been optimized in the past decade. In order to obtain a profound insight in the performance of DFB lasers, we will discuss two models (rate equation theory and coupled mode theory) that describe the DFB laser characteristics.

2.2   Rate equation theory

The rate equations state the time evolution of the average carrier density inside the active layer and of the average photon density inside the laser cavity. They are coupled to each other through the carrier density dependence of the stimulated emission, the absorption and the refractive index in the active material. They mathematically represent the interaction between the carrier density N and the number of photons S_m in mode m within the active layer [14]. The first equation describes the evolution of the carrier density N:

$$\frac{dN}{dt} = \frac{J}{qd} - AN - BN^2 - CN^3 - \sum_m G(N, \lambda_m)S_m \qquad (2.2)$$

The first term represents the injection of carriers (with charge q) in the active region with thickness d due to the current density J in the diode assuming 100% injection efficiency. Spontaneous carrier recombination is represented by the following three terms. Recombination via defects (Shockley-Read-Hall) and surfaces involves only one carrier and is therefore represented by AN. The bimolecular recombination is a process in which an electron and hole are involved and is therefore given by the quadratic term BN^2. The recombination process where the energy released by electron hole recombination is transferred to another electron is referred to as Auger recombination and represented by CN^3. The last term, the summation, corresponds to the stimulated emission in the different cavity modes m. This rate is proportional to the average photon density (S_m) in the mode and the gain coefficient (G). The gain coefficient depends on the carrier density and the wavelength but also could have photon density dependency at high photon densities.

The time evolution of the photon density inside the cavity depends on stimulated and spontaneous emission as photon creation sources and mirror loss and absorption as photon loss mechanisms. The photon density rate equation can thus be written as:

$$\frac{dS_m}{dt} = \left[G(N, \lambda_m) - \frac{1}{\tau_p} \right] S_m + R_{sp} \qquad (2.3)$$

The first term (with G (N, λ_m)) corresponds to the stimulated emission rate which is proportional to the average number of photons. The last term (with R_{sp}) accounts for the spontaneous emission that adds a number of photons to the considered mode per unit time. The losses inside the cavity are accounted by the photon lifetime τ_p and can be decomposed in two components:

$$\frac{1}{\tau_p} = \gamma = v_g(\alpha_{int} + \alpha_{mirror,m}) \qquad (2.4)$$

with v_g the group velocity, α_{int} the internal cavity losses (per unit of distance) and $\alpha_{mirror,m}$ representing the distributed mirror loss experienced by the photons in mode m.

It is interesting to look at the phase equation which describes the phase resonance condition for the different cavity modes. This equation for Fabry-Perot laser diodes can be expressed as:

$$\frac{\omega_m}{c} n_e(N, \omega_m) L = m\pi \tag{2.5}$$

with m an integer number and L the cavity length. Differentiating the equation results in:

$$\Delta\omega_m = -\frac{\omega_m}{c} v_g \frac{\partial n_e}{\partial N} \Delta N = \frac{\alpha}{c} \frac{\partial G(N,\lambda_m)}{\partial N} \Delta N \tag{2.6}$$

The α factor is the linewidth enhancement factor [15]. It is a material (e.g. bulk material or MQWs) and wavelength dependent parameter and normally has a value between 1 and 5.

The modal gain G appearing in the above equations is proportional to the material gain g :

$$G(N, \lambda_m) = \Gamma g(N, \lambda_m) v_g = g_{mod} v_g \tag{2.7}$$

with Γ the mode confinement factor which describes how much of the mode is confined in the active region. Both experimental and theoretical studies indicate that the gain g in bulk material and in unstrained quantum wells can be approximated as a linear function of the carrier density:

$$g(N, \lambda_m) = a(\lambda_m)(N - N_0) \tag{2.8}$$

where a=dg /dN is the differential gain (typically ~1 to 5 10^{-16} cm^2) and N_0 is the carrier density at transparency (typically ~0.5 to 2 10^{18} cm^{-3}). Figure 2.3 shows a typical gain curve of a 1550 nm bulk InGaAsP laser as a function of photon energy and carrier density.
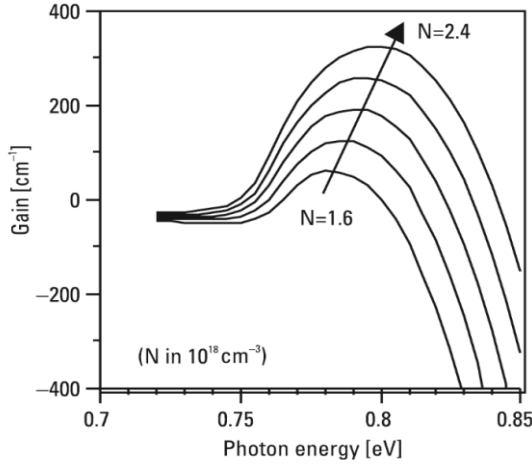
Figure 2.3: Gain in a bulk material as a function of photon energy for different carrier densities [14].

For strained layer quantum wells, the gain for a fixed wavelength or photon energy will have a sublinear dependence on the carrier density:

$$g = a \, ln \frac{N}{N_0} \tag{2.9}$$

This type of active region has very interesting features due to the discrete energy levels and the lower density of states. This leads to a reduction in the amount of carriers required to reach the lasing threshold and results in high quantum efficiency [16, 17].

As we already remarked, the gain of the lasing material could have an optical power dependency, if the laser is biased above threshold and the carrier density distribution in conduction and valence bands cannot reach its equilibrium condition by carrier scattering. In that case, lasing at a specific wavelength depletes the carrier density at the corresponding energy levels. This disturbance from the thermal equilibrium distribution is called spectral hole burning (SHB). The characteristic time scale associated with this process is $\tau_{shb} \sim 50 - 100$ fs. This will affect the gain properties of the material. The expression for gain suppression can be derived as:

$$g(N, E, S) = \frac{g(N,E,0)}{1+\varepsilon_{shb}S} \quad , \varepsilon_{shb} = \Gamma v_g \frac{\partial g}{\partial N} \tau_{shb} \tag{2.10}$$

This effect can be accompanied by transient carrier heating (CH) and carrier depletion (CD), which also cause a gain suppression (Figure 2.4). However, the exact contribution of each effect is not very well known [18].
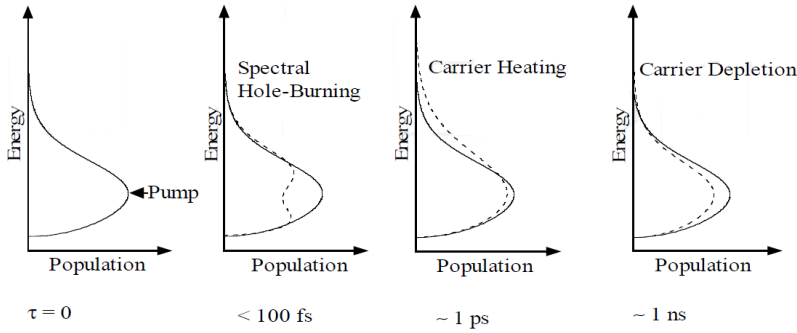
Figure 2.4: Nonlinear effects causing gain suppression: spectral hole burning, carrier heating and carrier depletion [18].

At a time scale of ~1 ps, the SHB effect is relaxed and the CH effect becomes dominant. The CH process increases the temperature of the carriers beyond the lattice's temperature. The main causes of carrier heating are (1) the stimulated emission, since it involves the removal of "cold" carriers close to the band edge and (2) the free-carrier absorption, which transfers carriers to higher energies within the bands. The "hot carriers" relax to the lattice temperature through the emission of optical phonons with a relaxation time of ~ 0.5 – 1 ps.

The effect of CD has a characteristic time scale of 0.1 to 1 ns. The stimulated electron-hole recombination depletes the carriers, thus reducing the optical gain. This effect causes another physical phenomenon known as spatial hole burning, which will be discussed in section 2.1.4 (coupled mode theory).

From the rate equations one can derive static and dynamic characteristics of a laser diode. The AM and FM response can be obtained after linearization of (2.2) and (2.3). This concept will be studied in more detail in the next section.

2.2.1 Small signal behavior

We restrict ourselves to single mode lasers with side mode suppression ratio more than 30 dB. Then the effect of the side mode on the main mode can be ignored [19]. Expanding the time dependent quantities in the form of:

$$N(t) = N_0 + Re(N_1 e^{j\Omega t}) \tag{2.11}$$

$$S(t) = S_0 + Re(S_1 e^{j\Omega t}) \tag{2.12}$$

$$J(t) = J_0 + Re(J_1 e^{j\Omega t}) \tag{2.13}$$

And linearizing (2.2) and (2.3) in N_1 and S_1, we find the following small signal equations:

$$\left(j\Omega + \frac{1}{\tau_d} + \frac{\partial G}{\partial N}S_0\right)N_1 = \frac{J_1}{qd} - (G + \frac{\partial G}{\partial S}S_0)S_1 \tag{2.14}$$

$$\left(j\Omega - \frac{\partial G}{\partial S}S_0 + \frac{R_{sp}}{V_{act}S_0}\right)S_1 = (\frac{\partial G}{\partial N} - \frac{\partial \gamma}{\partial N})S_0 N_1 \tag{2.15}$$

In which τ_d is the differential carrier lifetime:

$$\frac{1}{\tau_d} = A + 2BN_0 + 3CN_0^2 \tag{2.16}$$

These equations can be solved for S_1 (AM response) and N_1 (FM response), making use of equation 2.6:

$$S_1 = \frac{(\frac{\partial G}{\partial N} - \frac{\partial \gamma}{\partial N})S_0 \frac{J_1}{qd}}{\left[\left(j\Omega - \frac{\partial G}{\partial S}S_0 + \frac{R_{sp}}{V_{act}S_0}\right)\left(j\Omega + \frac{1}{\tau_d} + \frac{\partial G}{\partial N}S_0\right) + G(\frac{\partial G}{\partial N} - \frac{\partial \gamma}{\partial N})S_0\right]} \tag{2.17}$$

$$\Delta\omega = \frac{\frac{\alpha}{2}\frac{\partial G}{\partial N}\left(j\Omega - \frac{\partial G}{\partial S}S_0 + \frac{S_{sp}}{V_{act}S_0}\right)\frac{J_1}{qd}}{\left[\left(j\Omega - \frac{\partial G}{\partial S}S_0 + \frac{R_{sp}}{V_{act}S_0}\right)\left(j\Omega + \frac{1}{\tau_d} + \frac{\partial G}{\partial N}S_0\right) + G(\frac{\partial G}{\partial N} - \frac{\partial \gamma}{\partial N})S_0\right]} \tag{2.18}$$

The typical small signal responses for AM and FM are depicted in Figure 2.5 and 2.6.
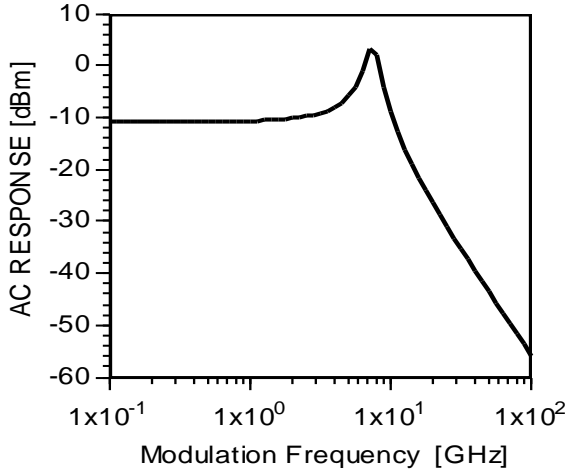
Figure 2.5: Typical AM response of a DFB laser, [14]
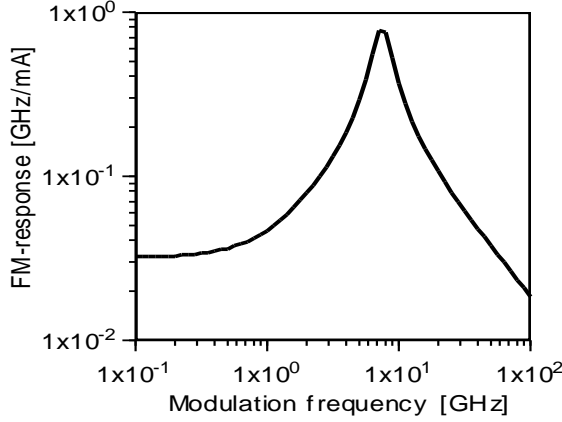
Figure 2.6: Typical FM response of a DFB laser [14].

Since the AM and FM responses are coupled to each other through the carrier dynamics, frequency modulation (chirp) will always be observed during the amplitude modulation of the laser diode. This effect is one of the limiting factors of using direct modulation of laser diodes in optical communication. The unwanted chirp can be suppressed by reducing the linewidth enhancement factor (α). This parameter has a lower value in multi quantum-well lasers than in bulk lasers. In more advanced configurations, chirp management techniques can be used to allow data transmission over longer spans in the presence of chirp as will be discussed later in this chapter.

In both figures 2.5 and figure 2.6, one can see a resonance peak. This resonance is known as the relaxation oscillation resonance in laser diodes which can be damped depending on the laser structure and bias. The damping rate is mainly caused by spontaneous emission and gain suppression and the differential gain. Close to threshold spontaneous emission-related damping is important. Far above threshold both power-dependent contributions become significant. The resonance frequency f_r and damping rate θ are given by [14]:

$$(2\pi f_r)^2 = G_{th}\left(\frac{\partial G}{\partial N} - \frac{\partial \gamma}{\partial N}\right)S_0 \approx \frac{\partial G}{\partial N}\frac{I - I_{th}}{qV_{act}} \qquad (2.19)$$

$$\theta = \frac{1}{\tau_d} + \frac{S_{sp}}{V_{act}S_0} + \frac{\partial G}{\partial N}S_0 - \frac{\partial G}{\partial S}S_0 \qquad (2.20)$$

where I_{th} is the threshold current and V_{act} is the volume of the active region. Typically the resonance frequency values are a few GHz to a few tens of GHz for semiconductor lasers. To design a high speed laser, the resonance frequency should be as high as possible at a chosen bias current I. In other words, the modal differential gain per unit active layer volume should be as high as possible. This requires a high differential gain, a strong confinement factor in the active region and a small active region volume.

The relaxation oscillation can be described by the resonant exchange of energy between photons and carriers (electrons) via stimulated emission and absorption. When population inversion occurs due to the injection of carriers into the active region, the gain exceeds the loss and consequently the photon density inside the cavity increases by the stimulated emission. This growth in the photon density will continue until the gain is suppressed due to the carrier depletion. In this situation, the number of photons decreases and slowly the carrier density increases above its equilibrium level. This cycle keeps repeating with a damping rate. There is an optimum damping value to achieve the highest modulation bandwidth. A high damping leads to an over-damped condition where the modulation bandwidth is not limited by the relaxation oscillation anymore but it is limited by the damping. This picture is illustrated in both time and frequency domains in Figure 2.7.
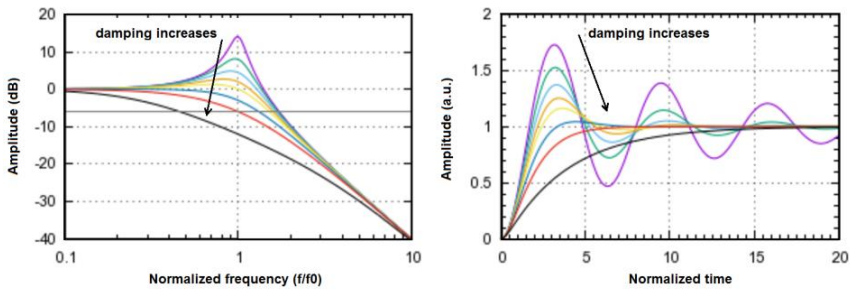
Figure 2.7: Influence of the damping rate on modulation bandwidth of the laser (left), in the time domain (right).

In our measurements, we observed an interesting behavior in the small signal response of our DFB lasers. In Figure 2.8, for example a low frequency contribution to the modulation response can be observed. This effect can be related to the modulation of the taper section which acts as semiconductor optical amplifier (SOA), or to spatial hole burning. Both of these phenomena have a cut-off frequency determined by the differential carrier lifetime. From the rate equations for a semiconductor optical amplifier, we can derive an expression for the small signal response in a similar way as we did for the DFB laser. The measured small signal response is the response from this compound structure (a DFB with two tapers). Depending on the amount of current injected in to the laser and tapers, the input optical power to the tapers and the gain of the tapers will change consequently. At low frequencies, the SOA can follow the modulated signal and respond with extra gain or absorption. But at higher frequencies, it will not follow and the small signal response can be referred to the DFB laser alone. This can lead to the low frequency response shown in Figure 2.8.

On the other hand, the axial distribution of the carrier density in a DFB laser can be non-uniform due to the non-uniform photon density. This phenomenon will be discussed later in this chapter when the coupled mode theory is introduced. This spatial hole burning effect can contribute to the intensity modulation and has a time constant given by the carrier lifetime. The contribution to the intensity (and frequency) modulation is therefore limited to

low frequencies (frequencies lower than $1/(2\pi.\tau)$ with τ the differential carrier lifetime).
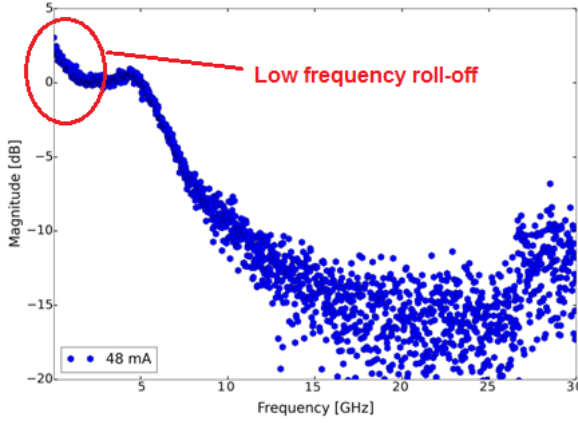
Figure 2.8: Small signal response of an III-V-on-Silicon DFB laser with a non-flat frequency characteristic. The length of the laser is 340 μm and the coupling coefficient is 135 cm⁻¹.

2.2.1 Large signal behavior

The small signal response provides information about the laser dynamical properties in the small perturbation approximation. This approximation can be applicable for analog modulation, but in digital on/off modulation one should deal with the large signal characteristics. In this case, high power pulses with very fast transitions are involved (steep rise and fall times) which contain high-frequency components in the frequency domain. The typical behavior of the carrier density and the photon density when the laser is switched on is depicted in Figure 2.9. The carrier density can follow the applied current variation with a finite rise time, but the photon density only starts to increase after a delay time (t_d). This delay time t_d is the time needed for the carrier density to reach the threshold value and can be calculated by solving the carrier rate equation (2.2), in which the stimulated emission is neglected:

$$\frac{dN}{dt} = \frac{I_1}{qV_{act}} - AN - BN^2 - CN^3 \qquad (2.22)$$

Assuming that the laser is biased below threshold at around I_0 and the current is switched to a value I_b above the threshold current I_{th}, one finds the following delay time, assuming that $\frac{dI}{dN}$ is constant:

$$t_d = \tau_d ln \frac{(I_b - I_0)}{(I_b - I_{th})} \qquad (2.23)$$

τ_d is the differential carrier lifetime and can be calculated using the carrier density at I_0. To avoid this delay, laser diodes are normally operated such that they do not switch off during modulation.
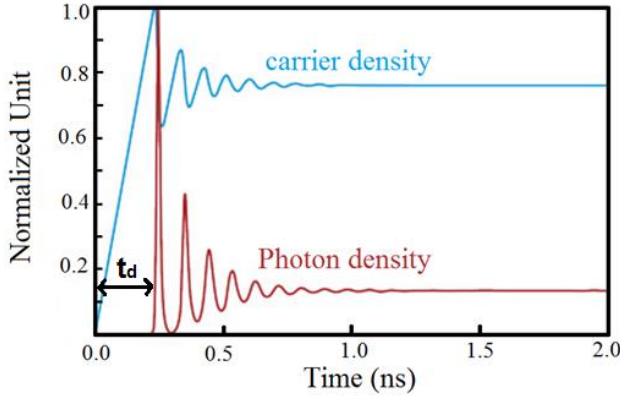
Figure 2.9: Typical carrier and photon density behavior of a DFB laser when it is switched on.

The laser is a complex nonlinear device and getting an accurate and realistic insight through solving these equations is a difficult task. In a typical laser, electrical, electro-optic, optical and thermal phenomena constantly interact in a nonlinear and complex way. Describing all these effects in detail may lead to a too complicated set of equations. There are techniques that satisfy the tradeoff between complexity and accuracy for DFB laser modeling. One of the most powerful methods is applying coupled-mode theory based on the longitudinal variation of the laser intensity and the carrier density. This enables us to study DFB laser features such as longitudinal spatial hole burning in an accurate way.

2.3   Coupled mode theory

This technique can be used to deal with a complex feedback system like a DFB laser, in which the carrier and photon density depend on the longitudinal coordinate. Multi-section DFB lasers can be studied in detail by using coupled-mode theory. The method is based on Maxwell's equations and they can be coupled to the carrier rate equation to study static and dynamic characteristics of the laser in the longitudinal direction.

The field inside the laser diode can be written as the sum of a forward $F(z)$ and backward $B(z)$ propagating wave:

$$E(z) = F(z) \exp(i\beta z) + B(z)\exp(-i\beta z) \qquad (2.24)$$

with β the wave propagation constant.

The grating will introduce a coupling between the forward and backward propagating waves. The reflected waves will add up constructively at the Bragg

wavelength. Typically, the coupling is described by the coupling coefficient κ which is proportional to the variation of the effective index Δ*n*. The spatial evolution of the forward and backward propagating waves can be described with coupled mode equations as [20-22]:

$$\frac{dF(z)}{dz} = (\gamma - j\Delta\beta)F(z) - j\kappa B(z) \tag{2.25}$$

$$\frac{dB(z)}{dz} = -(\gamma - j\Delta\beta)B(z) - j\kappa F(z) \tag{2.26}$$

with γ the gain for the field in a DFB laser with non-reflecting facets (corresponding to (Γ*g*-α$_{int}$)/2) and Δβ the Bragg deviation:

$$\Delta\beta = \frac{2\pi n_{eff}}{\lambda} - \frac{\pi}{\Lambda} \tag{2.27}$$

With Λ being the grating period. These equations constitute a set of two coupled, linear, first-order, ordinary differential equations for the functions *F(z)* and *B(z)*. They can be solved if we know *F* and *B* at a given point, for example z=z$_0$. The general relation between the fields at a point z and the fields at a point z$_0$ can be written as:

$$\binom{F(z)}{B(z)} =$$

$$\begin{pmatrix} \cosh(Sz) + \frac{\gamma - j\Delta\beta}{S}\sinh(Sz) & -\frac{j\kappa}{S}\sinh(Sz) \\ -\frac{j\kappa}{S}\sinh(Sz) & \cosh(Sz) - \frac{\gamma - j\Delta\beta}{S}\sinh(Sz) \end{pmatrix}\binom{F(z_0)}{B(z_0)} \tag{2.28}$$

with *S* given by:

$$S^2 = \kappa^2 + (\gamma - j\Delta\beta)^2 \tag{2.29}$$

This matrix which couples the forward wave to the backward one is called the propagator matrix T between z and z$_0$. In the simplest cases, we can solve these equations by knowing the boundary conditions. If we consider that both facets are anti-reflective (AR) coated, so that the reflectivity of each mirror is zero, by choosing z= L and z$_0$=0, applying the boundary condition results in $T_{22}(L) = 0$ or

$$SL\coth(SL) - \gamma L + j\Delta\beta L = 0 \tag{2.30}$$

This equation can be solved numerically to obtain oscillating modes in a gain versus detuning curve. The solutions for this equation in the γL versus ΔβL plane are depicted in Figure 2.10 for different values of the normalized coupling constant κL. It is clear that for the symmetric structure with AR-coated facets,

the DFB laser shows multimode operation or degeneracy: there are two modes with the same gain for a given κL.
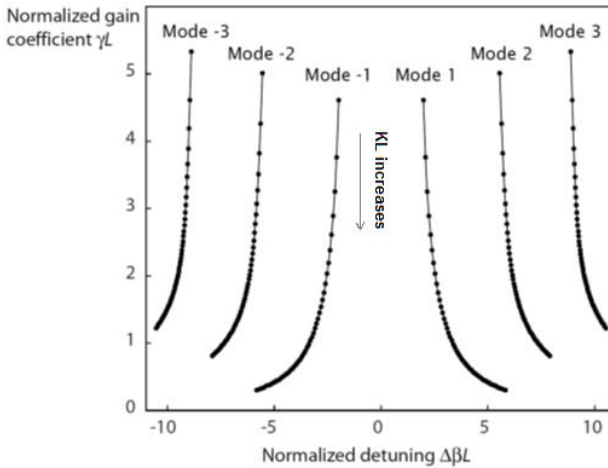
Figure 2.10: Solution of the threshold resonance condition for an AR-coated DFB laser for different values of κL. The values of the normalized coupling constant κ*L* range from 0.1 to 5 in steps of 0.1 [23].

The spacing between these two main modes is called the stop band of the DFB laser and gives a good indication about the laser's coupling coefficient. The existence of a stop band is a phenomenon for any periodic structure, which creates a gap in the propagating wave spectrum. Wavelengths inside this gap cannot propagate through the grating structure and will decay exponentially. By introducing a gain medium integrated with such a periodic structure (a DFB laser), the decay can be overcome and lasing can occur. For the Bragg grating without loss or gain, the relation between coupling coefficient and stopband width $\Delta\lambda$ can be expressed as:

$$\Delta\lambda = \frac{\lambda_\beta^2}{\pi n_{eff}L}\sqrt{(\kappa L)^2 + \pi^2}\qquad(2.31)$$

Where λ_β is the Bragg wavelength, n_{eff} is the effective refractive index and L is the grating length. The degeneracy in the lasing modes can be explained by looking at the sum of the distributed reflections at z_1 and z_2 in Figure 2.11. At the Bragg wavelength, the phase shift for propagating along half a period $\Lambda/2$ is $\pi/2$ and the phase of the subsequent interface reflections alternates between 0 and π. Therefore, the fields of the distributed reflections will add up constructively at z_1 and z_2. When there is no $\lambda/4$-shift in the middle of the grating, the bidirectional propagation across $[z_1, z_2]$ would add an additional

phase shift of π which would make the total round-trip phase in the cavity $(2p+1)\pi$ with p integer. Therefore, no mode will occur at the Bragg wavelength because the round-trip phase is not a multiple of 2π.
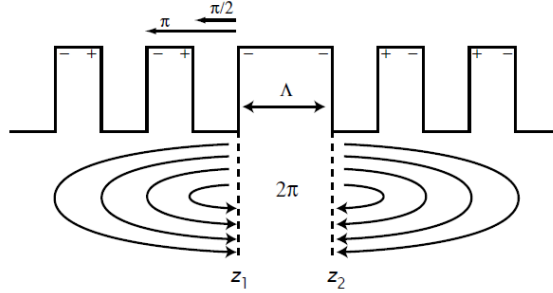
Figure 2.11: Physical explanation of the insertion of a $\lambda/4$-shift in the middle of the grating [14].

This problem can be solved by three different methods. Adding gain coupling [9] or facet reflectivity [25], will remove the degeneracy of the modes. Another technique is introducing a phase shift in the middle of the grating [26, 27]. This is the most straightforward and systematic way of making a single mode DFB laser. With the other methods, it is difficult to predict which mode (on the right or left side of the spectrum) will lase. The algorithm described above to find the oscillating modes can be generalized to include additional phase shifts. By adding a $\lambda/4$-shift in the middle of the cavity, an extra phase shift of $\pi/2$ will be introduced to each wave passing along this section. In total, a π shift will be added to the round-trip phase and it will remove the mode degeneracy. This can be described mathematically by adjusting the transfer matrix as $\mathbf{T}(L/2)\mathbf{T}(\Lambda/2)\mathbf{T}(L/2)$. After carrying out the matrix multiplications, the oscillation condition is found to be:

$$SLcoth\left(\frac{SL}{2}\right) - (\gamma - j\Delta\beta \pm \kappa)L = 0 \tag{2.31}$$
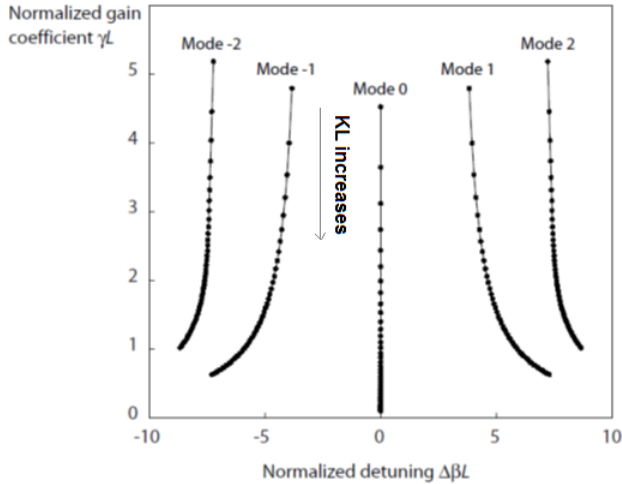
Figure 2.12: Solution of the threshold resonance condition for an AR-coated λ/4 shifted DFB laser for different value of κL. The values of the normalized coupling constant κ*L* range from 0.1 to 5 in steps of 0.1 [23].

The solutions for these equations in the γ*L* versus Δβ*L* plane are depicted in Figure 2.12 for different values of the normalized coupling constant κ*L*. The structure with a λ/4-shift has a single lowest order mode at the Bragg wavelength (Δβ= 0). Moreover, this mode has a lower loss than the other modes which means that it will dominate at low bias. Far above threshold, multimode operation can sometimes be observed due to longitudinal spatial hole burning [28].

The effective refractive index of the cavity is carrier density dependent. Since the lasing wavelength (Bragg wavelength) is strongly dependent on the refractive index of the cavity, any variation in the carrier density distribution will affect the laser operation. It has been demonstrated that low linewidth and high power lasers can be realized either by high coupling coefficients or longer cavities [29]. But theoretically and experimentally it has been found that a laser with high coupling coefficient or longer cavity will be multimode already at low or moderate power levels [30, 31]. This effect can be explained by studying the carrier density longitudinal distribution. The non-uniform longitudinal distribution of the carrier density is called Longitudinal Spatial Hole Burning (LSHB). This effect is strong in a DFB laser with a λ/4 phase shift, because the light intensity is concentrated in the vicinity of the λ/4-shift position. Mostly in text books, this term was mentioned just spatial hole burning, since lateral spatial hole burning does not have a strong effect.

The longitudinal distribution of carrier density and optical power for a λ/4 phase shifted DFB is shown in Figure 2.13 for different bias currents. As the bias current increases, the absolute non-uniformity in the carrier distribution also

increases. The laser has a coupling coefficient κ of 30 cm⁻¹ and has a 400 μm long cavity. It is clear that the carrier density is less (at the end facets and center of the cavity) where the photon density is high due to stimulated emission.
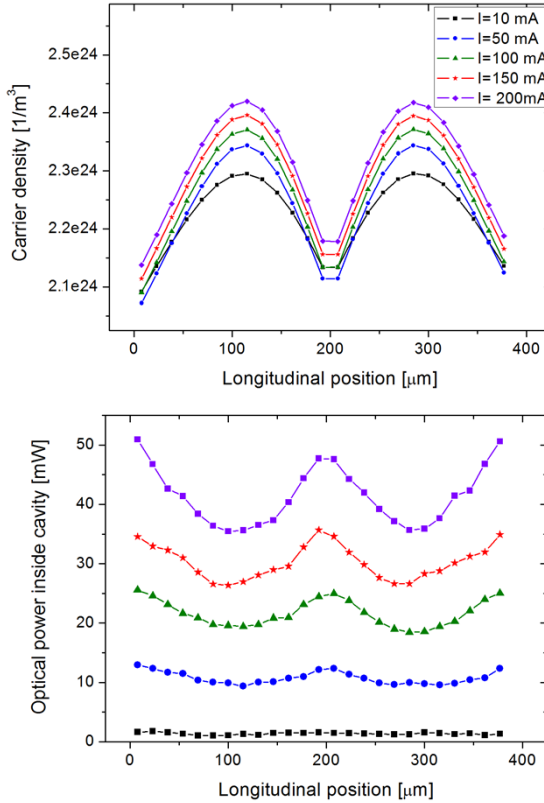

Figure 2.13: Longitudinal spatial hole burning in a λ/4 phase shifted DFB with a κ of 30 cm⁻¹ and a length of 400 μm and the facets reflectivity is zero.

As we discussed in the previous section, this spatial effect can be studied mathematically by using coupled mode theory. The exact treatment of the LSHB-effects means that the one dimensional rate equation for the carriers together with the wave equation (with a complex dielectric constant varying in space and time) have to be solved in a coupled way. To do this, the laser is longitudinally divided into small sections where the carrier density is assumed to be constant.

Different methods have been proposed to reduce the effect of the LSHB in DFB lasers. It can be reduced by the introduction of a longitudinal variation of the coupling coefficient and/or net gain [32]. Multi-section DFB lasers have been proposed by different authors to reduce the LSHB effect [33, 34]. In this approach, the use of multiple phase-shift regions leads to a more uniform axial distribution of the mode intensity inside the laser cavity than in a conventional

single phase shifted DFB laser. As a result, spatial hole burning is less effective in destabilizing the single-mode operation, and the performance of such modified DFB lasers should be less dependent on the operating power [33].
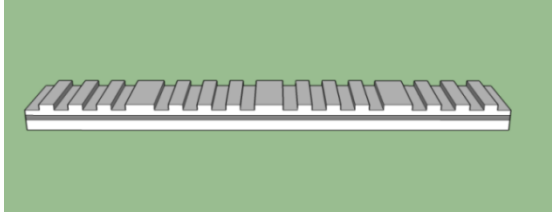
Figure 2.14: Multiple phase shifted DFB laser used to reduce the effect of LSHB.

## 2.4 Extending the bandwidth and reach of a directly modulated DFB laser

For DFB lasers to be competitive for high performance longer reach links, there is a need to extend their modulation bandwidth and extend their reach. The following sections will give a brief introduction on techniques used to extend the bandwidth of DFB lasers and to extend the reach of DFB lasers based single mode fiber links.

2.4.1 Bandwidth extension: photon-photon resonance

Conventional laser modulation speeds are internally limited by material properties, i.e. mainly by the interaction speed between electronic states and the electromagnetic field in the laser cavity. This relatively slow carrier-photon resonance (CPR) interaction, which shows itself in the relaxation oscillation, enables to fabricate a laser with almost 30 GHz as highest 3-dB bandwidth (for a 1550 nm laser with 120 μm cavity length [41]). Different approaches, like detuned loading [42], injection locking [43] and push-pull modulation [44] were used to overcome these intrinsic limitations and allow a significant increase of the 3-dB bandwidth beyond the relaxation oscillation resonance frequency of a standard laser.

The most promising way however to extend the bandwidth beyond the relaxation oscillation limitation is the use of a photon-photon resonance [45, 47]. This concept is illustrated in Figure 2.15. In the IM response of the laser, the first peak is called the carrier-photon resonance peak. A second resonance peak (the photon-photon-resonance) occurs as soon as one of the optical modulation side-bands coincides with a compound cavity resonance. This can, in principle, happen in all laser diodes. However, in order for the second resonance to extend the modulation bandwidth of the laser, it should be a strong resonance not too far from the first one. In other words, the first resonance peak should occur at

rather high frequencies, and the frequency separation between main and side mode should be rather small. For the first resonance peak to occur at rather high frequencies, one in general has to consider short cavities and high bias currents (see equation 2.19). In addition, the modulation bandwidth enhancement techniques mentioned above can be applied here to shift the first resonance position. The position of the second peak can be adjusted by adding an external cavity to the laser with well-chosen optical length. From the Fabry-Perot cavity approximation, we know that a small separation between main and side mode can be realized by a long external cavity.
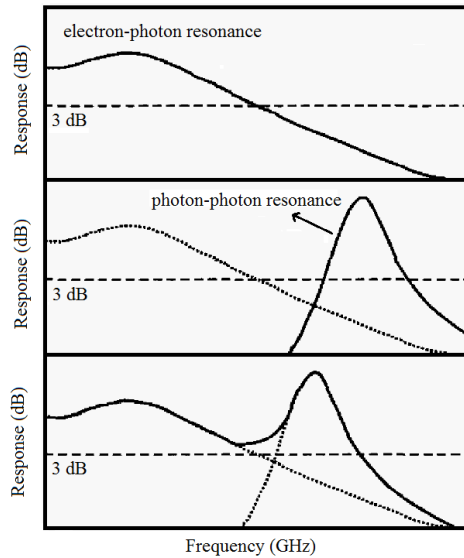
Figure 2.15: Schematic illustration and location of carrier-photon (CP) and photon-photon (PP) resonances in the modulation transfer function (top and middle part). The lower part illustrates a case where the modulation bandwidth is strongly increased by the overlap of the two resonances [45].

This technique has been applied to different kinds of DBR lasers [46], two-section distributed feedback (DFB) lasers [48], a Coupled Cavity Injection Grating laser [45], an Active Feedback Laser [49, 50] and a Passive Feedback Laser (PFL) [51, 52]. In order to calculate the small signal response of such systems, a longitudinal model should be used. A detailed theoretical explanation and numerical calculation can be found in [31], based on the laser diode model CLADISS. In this model, small-signal approximations of the single-mode longitudinal coupled-wave equations and the carrier-rate equations are used. For a two section DBR laser with an active and a passive section, one can obtain a typical numerical IM-response as in Figure 2.16.
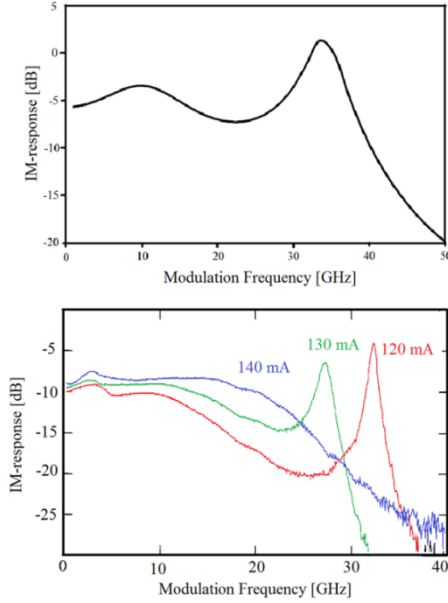
Figure 2.16: Calculated intensity modulation response of a DBR laser with AR-coated facet at the Bragg section and for $\kappa = 30$ cm^{-1} and $\alpha_{int} = 0$ cm^{-1} (top), Experimentally obtained modulation response for two-section InGaAsP DBR laser emitting at 1550 nm (bottom) [46].

Similar behavior has been obtained for a DFB laser with an external passive feedback (Figure 2.17) [52]. In this work, the modulation enhancement has been studied theoretically and experimentally. They showed that the modulation bandwidth can be extended up to 50 GHz, far beyond the first resonance peak at 12 GHz.
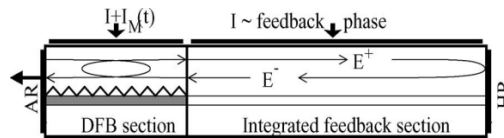
Figure 2.17: Schematic of a passive feedback laser, consisting of an anti-reflection coated DFB and a high-reflection coated Integrated Feedback section, E$^+$ forward wave, E$^-$ backward wave, I$_M$: modulation current.

The passive section was used to tune the phase of the compound cavity in order to reach the maximum modulation bandwidth. This can be done via the refractive index n_{eff} of the IFB (Integrated Feedback) section by current injection into this section.

Extension of the modulation bandwidth by the exploitation of a photon-photon resonance requires a carefully chosen external feedback. Adding the external cavity term to the rate equations one can derive (2.32).

$$\frac{\Delta S}{\Delta I} = \frac{\dfrac{dG}{dN}\dfrac{S_0}{qV}}{\left[j\Omega + \dfrac{1}{\tau_d} + \dfrac{dG}{dN} S_0 \right]\left[j\Omega + k_c\left(1 - e^{-j\Omega\tau}\right) + \varepsilon G_{th} S_0 \right] + \dfrac{dG}{dN} G_{th} S_0} \tag{2.32}$$

where Ω is angular frequency, τ_d the differential carrier lifetime, ε the gain suppression. If the external feedback magnitude is too strong, it gives strong oscillations in the intensity modulation response, as shown in Figure 2.18. If the external feedback is too weak, the photon-photon resonance doesn't appear or only is a weak resonance and it can't extend the modulation bandwidth either. The feedback strength k_c is, for DFB lasers, a complicated function of the external facet reflection (r_e) and of the DFB laser structure. For a fixed r_e, the feedback strength k_c usually decreases with increasing normalized coupling coefficient κL of the DFB laser. The phase difference between reflected field and the cavity field is also an important factor to get stable photon-photon response. As described in [53], when there is a phase alignment, the state corresponds to maximum feedback to the laser cavity. At moderately high reflection, a carrier number change will change the resonance frequency of the semiconductor cavity. This in turn causes a change in the phase difference between the laser field and the reflected field, reducing the feedback, resulting in a decreasing photon density in the cavity. Since there is a tight link between the photon density and the carrier density, the carrier density will further increase. This process can continue to grow the phase misalignment and result in instability then. Therefore the strength of the reflection and the phase should be optimized in order to realize a stable bandwidth extended laser.
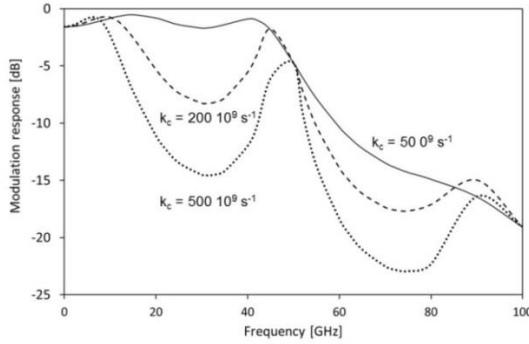
Figure 2.18: Small signal analysis performed for external cavity lasers with 3 different external feedback strengths κ_c (50, 200 and 500 10^9 s^{-1}) and for a cavity round trip time of 20ps.

2.4.2 Reach extension: Chirp managed laser

As we discussed before, direct modulation gets lots of attention as an energy efficient and compact method in WDM links. The simplicity of this method compared to external modulation techniques makes this method very attractive.

However, the performance of directly modulated lasers in the transmission over standard single mode fiber has been limited by the intrinsic chirp of the modulated lasers and the resulting spectral broadening [54] especially in the C-band. In this section, a technique called chirp management for directly modulated lasers will be introduced.

The chirp managed laser is an alternative transmitter technology that allows a DML to be used in longer reach link.

In fact, while EAMs are typically limited to 100 km reach at 10 Gb/s in SSMF fiber (using its negative chirp to go beyond the dispersion limit, at the cost of higher insertion loss), using a CML supports a reach of over 200 km without dispersion compensation [55]. In this method the chirp of the signal is actually used to extend the reach. The frequency chirp of DMLs has two major components, the transient chirp and the adiabatic chirp. At low data rates, the thermal chirp becomes dominant. Here we focus on high data rate operation (> Gb/s), therefore one can ignore the thermal chirp effect. The chirp of a DML is related to the laser output optical power P(t) through the expression[56]:

$$\Delta \nu(t) = \frac{\alpha}{4\pi} \left\{ \frac{d}{dt} \left[\ln(P(t)) \right] + \kappa P(t) \right\} \tag{2.33}$$

where α is the linewidth enhancement factor and κ is the adiabatic chirp coefficient, which can be calculated from:

$$\kappa = \frac{2\Gamma}{\eta h \nu V} \varepsilon \tag{2.34}$$

where ν is the optical frequency, h is Plank's constant, η is the differential quantum efficiency, Γ is the confinement factor and ε is the nonlinear gain compression factor and V is the active region volume. In formula (2.33), the first term is the transient chirp and the second term is the adiabatic chirp. DMLs can be classified as transient or adiabatic chirp dominated. Transient chirp occurs at each transition between "1"s and "0"s. (Figure 2.19-a). As one sees in Figure 2.19-b, a frequency modulation resulting from the adiabatic chirp follows the intensity modulation. The frequency modulation is the result of gain compression in the laser, which generates an adiabatic chirp in proportion to the output intensity. "1" bits are blue shifted relative to the "0" bits. Normally both types of chirp are undesired and cause an unwanted pulse broadening after transmission over an optical fiber. In the chirp management laser technique (CML) the adiabatic chirp can be exploited to enhance signal quality after transmission over optical fiber [56, 57]. As the bias current of the laser increases above the threshold current, the influence of the transient chirp becomes less. This will also add other benefits to the laser properties such as high output power and wide modulation bandwidth.
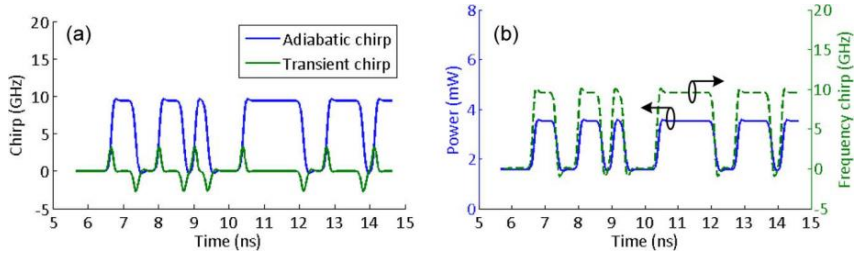
Figure 2.19: Simulated chirp for directly modulated DBR laser driven by 2.5 Gb/s NRZ PRBS signals. (a) Adiabatic chirp and transient chirp. (b) Output power and total frequency chirp [56].

The principle of the chirp management is illustrated in Figure 2.20. Due to the adiabatic chirp the carrier signal is blue shifted on the "1" state with respect to the "0"state. The laser wavelength is aligned on the transmission edge of the Optical Spectrum Reshaper (OSR) filter, so to pass the blue shifted "1" bits and attenuate the red shifted "0" bits. Normally because of the high bias current, the modulated signal extinction ratio (ER) is low (1-2 dB). This FM–AM conversion increases the ER at the output of the OSR filter to >10 dB. This is a first advantage of using CML.
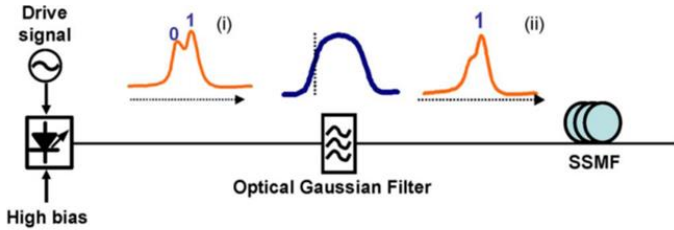
Figure 2.20: Schematic of the CML principle, the optical Gaussian filter is a specific implementation of an optical spectrum reshaper [58].

Secondly, consider a "1 0 1" bit sequence at 10 Gb/s having a 5 GHz frequency modulation; i.e. "1" bits have 5 GHz higher optical frequency than "0" bits. Hence the phase of the carrier slips by $2\pi \times 5GHz \times 100ps = \pi$ during the "0" bit making the second "1" bit π out of phase with the first "1" bit. Normally dispersion spreads the energy of the "1" bits into adjacent "0" bits and closes the eye. However, the π phase in the CML causes destructive interference in the middle of the "0" bits, keeping the eye open after fiber dispersion (Figure 2.21), together with the high ER, which is provided through FM-AM conversion by the filter (Figure 2.20). The same phase correlation is achieved in phase correlated optical duobinary by use of pre-coding and minimum transmission biasing of a Mach-Zehnder modulator [59] (Figure 2.22).
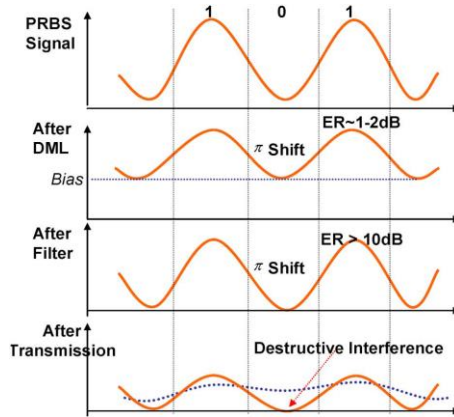
Figure 2.21: Schematic of the OSR function in a CML configuration [58].
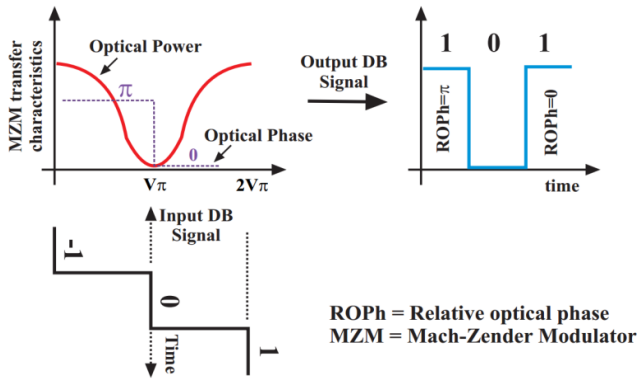

Figure 2.22: MZM bias and derive condition for the OD signal (bottom) [59].

2.5 Modulation formats & equalization

In digital modulation, an analog carrier signal is modulated by a discrete signal. The most fundamental digital modulation techniques are based on ASK (amplitude-shift keying), FSK (frequency-shift keying) and PSK (phase-shift keying). In a direct modulation system the intensity of light is modulated, making it a form of ASK.
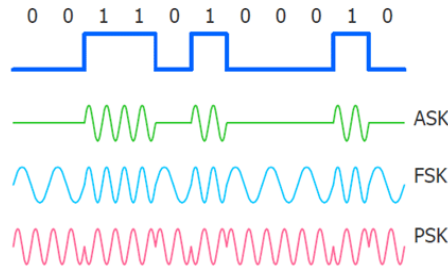
Figure 2.23: A digital data stream is encoded using different modulation formats.

2.5.1 On-Off keying

In this thesis we will deal with ASK modulation which is the most popular modulation format in optical communication systems for short reach applications. The Non-Return-to-Zero-On-Off-Keying (NRZ-OOK) format is one of the ASK prototypical representations of binary data: a logical zero state is transmitted as one signal level, and a logical one state as another level. Levels change at bit boundaries only if the bit value changes and remain constant for the entire duration of the bit period. These states are represented by different levels. There is a threshold level to distinguish any level above it to be considered as a "one" signal level and logically any level below it represents a "zero" signal level.

This is the simplest modulation scheme in data communication systems. There are other formats similar to NRZ such as return-to-zero (RZ) or Manchester coding, but their description is beyond the scope of this chapter. Many NRZ test patterns have been created for system test and verification purposes by different computational algorithms. These patterns are usually designed either to simulate the actual data or to stress certain aspects of the system. To understand the effects of various test patterns on a particular system, it is important to understand the frequency characteristics of both the test pattern and the system under test. In the time domain, each bit is assigned a unique time slot of duration, called the bit period. Between each two bits with different states there is a transition time. This transition time is usually much shorter than the bit period. High frequency components in the spectrum originate from the fast transitions and low frequency components are coming from continuous one or zero sequences.

As a result, we can assign for each NRZ-OOK test pattern an associated power spectral density (PSD) that indicates the frequency distribution of the power in the pattern. For a signal x(t), the autocorrelation function is:

$$R_x(\tau) = \lim_{T\to\infty} \frac{1}{T} \int_{-T/2}^{T/2} x(t)x(t+\tau)dt \qquad (2.34)$$

This function measures the similarity of the signal with itself as a function of delay. The Fourier transform of this autocorrelation function is the power spectral density of the signal. The PSD of a NRZ-OOK PRBS modulated signal is depicted in Figure 2.24. It is important to notice that the PSD gives information about the bandwidth requirements of a link. If this requirement is not satisfied, the signal will be distorted. As can be expected, the bandwidth requirements scale with the bit rate 1/T.
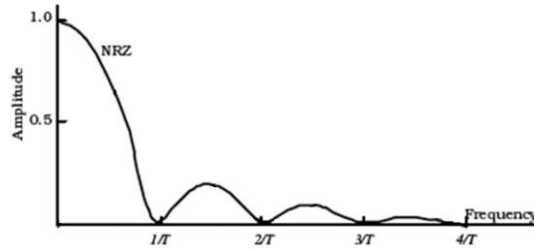

Figure 2.24: NRZ-OOK format power spectral density [60].

2.5.2 Pulse Amplitude Modulation (PAM)

In recent years, NRZ-OOK modulation has been used in most practical applications. As the megatrends of cloud computing, big data, social networks,… continue to accelerate and drive the insatiable need for unlimited bandwidth, there is obviously a demand to increase the speed of interconnect lines while maintaining cloud economics. PAM-4 modulation (Pulse Amplitude Modulation with 4 levels) has now been recognized [61] as the modulation scheme that will take the data transmission to the next generation of Ethernet deployments for optical interconnects by doubling the number of bits per symbol at the same baud rate. This multilevel modulation, with higher spectral efficiency, introduces a new degree of freedom in the link design. The drawing in Figure 2.25 shows the difference between NRZ-OOK and PAM-4 modulations.
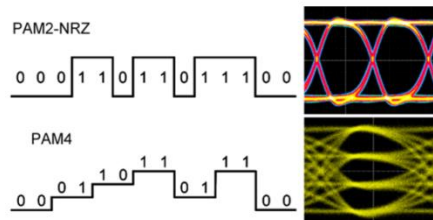

Figure 2.25: the difference between NRZ signal and PAM-4 signal [61].

2.5.3 Electrical duobinary

As the demand for faster communication increases there has been a natural evolution towards a better usage of channel bandwidth. Electrical duobinary (ED) transmission is one such idea that was developed in the early 1960's in the context of electrical data transmission and was later applied to optical signals in the late 1990's [62]. ED can be generated by two different methods, one is using a limited bandwidth component as a duobinary filter and another method is called the Delay-And-Add technique (Figure 4.26). The way that we used this format was the former case by operating a DFB laser beyond its bandwidth limits. Since the small signal response of the laser has a low pass filter shape (flat at lower frequencies and steep roll-off at higher frequencies), an electrical duobinary signal can be modulated on the optical carrier.
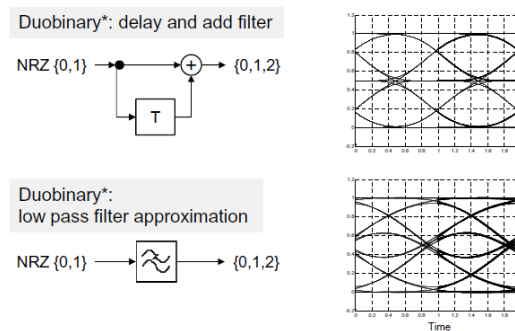
Figure 2.26: Two methods for an ED signal generation [62].

The duobinary signal presents three levels. The lower and upper signal levels represent sequences of 0s and 1s respectively whereas a transition from 0 to 1 or from 1 to 0 is mapped on the central level. Therefore, in the decoding of the duobinary signal, it is noticed that the decoding of the present bit value depends on the correct decoding of the previous bit value. This allows as decoding errors tend to propagate [63]. Therefore a precoder at the transmitter is required in order to allow easy data recovery at the receiver

2.5.4 Modulation bandwidth requirement

The bandwidth requirement is more relaxed for a PAM-4 signal than for a NRZ signal for the same bit rate. This is also the case for an electrical duobinary signal. These three intensity modulation formats are illustrated in Figure 2.27 with corresponding PSD curves. One can see that both PAM-4 and duobinary formats require only half of the bandwidth of the NRZ format. But their signal to noise ratio (SNR) is also less than that of the NRZ format.
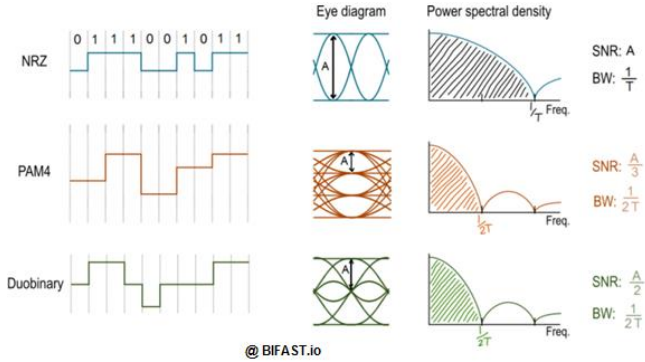
Figure 2.27: Schematic representation of the three intensity modulation formats.

2.5.5 Equalization

The optical signals passing through the transmission links encounter numerous optical devices such as multiplexers, optical cross connects, and optical amplifiers and also optical fibers. This causes degradation of the signal due to optical impairments in the links. But in optical networks, signal degradation can be also caused by electronic circuits. In the receiver, interface circuits and photodetectors introduce timing jitter, shot noise, and thermal noise (e.g., trans-impedance amplifier) [64].

In the optical fiber, Inter-symbol interference (ISI) is caused by the non-uniform frequency response of the system which modifies the pulse-shape of different bits in a signal. A high power optical signal can also cause a nonlinear distortion in the transmitted data. Combinations of these effects with the loss characteristics of a transmission path will close the eye diagrams. Since some of these effects are linear and deterministic, information of the original signal is still in the received signal whether or not the eye is closed; therefore we can recover the eye by mean of equalization.

For optical links different equalization methods exist that were mostly developed for long haul communication [65, 66].

These techniques now are becoming popular also in high speed short reach systems. Feed Forward Equalization (FEE) is one of the standard equalization methods. The simple explanation of the feed forward equalization can be given that it uses information from previously received bits and feeds forward information from earlier bits to later bits [66]. The number of bits that are used determines the number of so called taps which are the correction factors applied to the voltage levels of other bits. The normalized least mean square algorithm can be employed to determine the equalizer taps. More advanced corrections then can be applied to further improve the signal quality.

A complementary way to tackle the limit of equalization techniques is called Forward error correction. In this method the sender encodes the message in a redundant way by using an error-correcting code (ECC). In this case, the

source (transmitter) sends redundant data and the destination (receiver) recognizes only the portion of the data that contains no apparent errors [67].

2.6 Conclusion

This chapter discussed the use of a heterogeneously integrated III-V-on-silicon DFB laser for direct modulation. We started with a brief introduction of DFB lasers and extended the discussion to rate equations and coupled mode theory. From the rate equations, the static and dynamic (small and large signal) behavior of the laser have been derived.

The small signal response provides information about the modulation bandwidth. This theoretical framework gives insight into which laser parameters are key to enhance its high speed characteristics. For instance, in order to enhance the modulation bandwidth of the DFB laser, the confinement factor of the propagating mode inside the active region and the differential gain should be high.

On the other hand, from couple mode theory the condition for the single mode operation can be calculated. According to this theory, having a λ/4 phase shift in the middle of the DFB cavity ensures the single mode performance.

In the rest of the chapter, two methods to improve the performance of a directly modulated DFB laser have been discussed. Leveraging the external cavity coupled to the DFB laser, the modulation bandwidth can extend to beyond the relaxation oscillation resonance limit. The key aspects of the external cavity were discussed. The feedback light intensity and phase should be within an acceptable range to observe the modulation bandwidth enhancement.

The powerful technique of chirp management has been presented. Using this method, unwanted inherent adiabatic chirp of a directly modulated laser can be utilized to extend the reach beyond the single mode fiber dispersion limit.

Finally, the modulation formats that we used in this PhD are introduced with a brief explanation about their bandwidth requirement and the way to generate them. Equalization and forward error correction also briefly discussed.

References

[1] T. Suhara, "Semiconductor laser fundamentals", CRC Press, (2004).

[2] T. Numai, "Fundamentals of Semiconductor Lasers", Springer-Verlag New York, Inc, (2010).

[3] Witteman, W.J, "The CO2 Laser", Springer, (1987).

[4] R. N. Hall, R. O. Carlson, T. J. Soltys, G. E. Fenner, and J. D. Kingsley, "Coherent light emission from GaAs Junctions", Physical Review Letters, vol. 9(9), pp. 366– 368, (1962).

[5] M. I. Nathan, W. P. Dumke, G. Burns, F. H. Dill, and G. Lasher, "Stimulated emission of radiation from GaAs p-n Junctions", Applied Physics Letters, vol. 1(3), pp. 62–64, (1962).

[6]   N. Holonyak and S. F. Bevacqua, "Coherent (visible) light emission from Ga(As$_{1-x}$ P$_x$) junctions", Applied Physics Letters, vol. 1(4), pp. 82–83, (1962).

[7]   T. M. Quist, R. H. Rediker, R. J. Keyes, W. E. Krag, B. Lax, A. L. McWhorter, and H. J. Zeigler, "Semiconductor master of GaAs", Applied Physics Letters, vol. 1(4)pp. 91–92, (1962).

[8]   H. Kogelnik and C. V. Shank. "Stimulated emission in a periodic structure", Applied Physics Letters, vol. 18(4), pp. 152–154, (1971).

[9]   H. Kogelnik and C. V. Shank, "Coupled-wave theory of distributed feedback lasers" Journal of Applied Physics, vol. 43(5), pp. 2327–2335, (1972).

[10] M. Nakamura, A. Yariv, H. W. Yen, S. Somekh, and H. L. Garvin, "Optically pumped GaAs surface laser with corrugation feedback", Applied Physics Letters, vol. 22(10)pp. 515–516, (1973).

[11] C. V. Shank, R. V. Schmidt, and B. I. Miller, "Double-heterostructure GaAs distributed-feedback laser", Applied Physics Letters, vol. 25(4), pp. 200–201, (1974).

[12] D. R. Scifres, R. D. Burnham, and W. Streifer, "Distributed-feedback single heterojunction GaAs diode laser", Applied Physics Letters, vol. 25(4), pp. 203–206, (1974).

[13] M. Nakamura, K. Aiki, J.Umeda, A. Yariv, H.W. Yen, and T.Morikawa, "GaAs- Ga$_{1-x}$ Al$_x$As double-heterostructure distributed-feedback diode lasers", Applied Physics Letters, vol. 25(9), pp. 487–488, (1974).

[14] G. Morthier and P. Vankwikelberge. "Handbook of distributed feedback laser diodes". Artech House Publishers, (1997).

[15] C.-F. Chuang, Y.-H. Liao, C.-H. Lin, S.-Y. Chen, F. Grillot, and F.-Y. Lin, "Linewidth enhancement factor in semiconductor lasers subject to various external optical feedback conditions", Optics. Express. Vol. 22, pp. 5651-5658, (2014).

[16] Y. Arakawa and A. Yariv, "Quantum well lasers--Gain, spectra, dynamics", IEEE Journal of Quantum Electronics, vol. 22(9), pp. 1887-1899, (1986).

[17] C. Weisbuch, and V. Borge, "Quantum semiconductor structures: Fundamentals and applications", Academic press, (2014).

[18] N. Das, H. Kawaguchi and M. Razaghi, "Optical Communication", InTech, 2012.

[19] R. Tucker, "High-speed modulation of semiconductor lasers", Journal of Lightwave Technology, vol. 3(6),, pp. 1180-1192, (1985).

[20] H. Ghafouri-Shiraz and B. S. K. Lo, "Distributed feedback laser diodes: principles and physical modelling", Wiley, (1996).

[21] A. Yariv and P. Yeh. "Photonics Optical electronics in modern communications". Oxford University Press, sixth edition, (2007).

[22] M.-C. Amann, J. Buus, and D.J. Blumenthal, "Tunable laser diodes", Wiley- Interscience, second edition, (2005).

[23] K. Huybrechts. "Digital photonics using single laser diodes for all-optical network nodes". Doctoral Thesis, Ghent University, (2010).

[24] S. McCall and P. Platzman, "An optimized π/2 distributed feedback laser", IEEE Journal of Quantum Electronics, vol. 21(12),, pp. 1899-1904, (1985).

[25] Jens Buus, "Single Frequency Semiconductor Lasers", SPIE Press, (1991).

[26] H. A. Haus and C. V. Shank. "Anti-symmetric taper of distributed feedback lasers". IEEE Journal of Quantum Electronics, vol. 12(9), pp. 532–539, (1976).

[27] K Utaka, "Analysis of quarter-wave shifted DFB laser". Electronics Letters, 20(8):326–327, (1984).

[28] J. E. A. Whiteaway, G. H. B. Thompson, A. J. Collar and C. J. Armistead, "The design assessment of λ/4 phase-shifted DFB laser structures", IEEE Journal of Quantum Electronics, vol. 25(6), pp. 1261-1279, (1989).

[29] S. Ogita, Y. Kotaki, M. Matsuda, Y. Kuwahara and H. Ishikawa, "Long-cavity multiple-phase-shift distributed feedback laser diode for linewidth narrowing", Journal of Lightwave Technology, vol. 8(10) , pp. 1596-1604, (1990).

[30] H. Soda , Y. Kotaki , H. Sudo , H. Ishikawa , S. Yamakoshi and H. Imai, "Stability in single longitudinal mode operation in GaInAsP/InP phase-adjusted DFB lasers", IEEE J. Quantum Electron., vol. 23, pp. 804-814, (1987).

[31] P. Vankwikelberge, G. Morthier and R. Baets, "CLADISS-a longitudinal multimode model for the analysis of the static, dynamic, and stochastic behavior of diode lasers with distributed feedback", IEEE Journal of Quantum Electronics, vol. 26(10), pp. 1728-1741, (1990).

[32] P. Zhou and Lee, G. S. "Mode selection and spatial hole burning suppression of a chirped grating distributed feedback laser", Applied Physics Letters, vol. 56, pp. 1400-1402, (1990).

[33] G. P. Agrawal and A. H. Bobeck, "Modeling of distributed feedback semiconductor lasers with axially-varying parameters", IEEE Journal of Quantum Electronics, vol. 24(12), pp. 2407-2414, (1988).

[34] T. Kimura and A. Sugimura, "Linewidth reduction by coupled phase-shift distributed-feedback lasers", Electronics Letters, vol. 23(19), pp. 1014-1015, (1987).

[35] B. Teipen, "Considerations on Baud Rate and Lane Number for 400 Gigabit Ethernet Optical Interfaces", IEEE 802.3bs 400GbE, Norfolk VA, (2014).

[36] G. Denoyer, A. Chen, B. Park, Y. Zhou, A. Santipo, R. Russo, "Hybrid Silicon Photonic Circuits and Transceiver for 56Gb/s NRZ 2.2km Transmission over Single Mode Fiber", ECOC14, PD2.4, (2014).

[37] T. Fujisawa, K. Takahata, W. Kobayashi, T. Tadokoro, N. Fujiwara, S. Kanazawa, and F. Kano, "1.3 μm 50 Gbit/s electroabsorption modulators integrated with DFB laser for beyond 100G parallel applications", Electronic. Letter, vol. 47(2),, pp. 708-709, (2011).

[38] K. Nakahara, Y. Wakayama, T. Kitatani, T. Taniguchi, T. Fukamachi, Y. Sakuma and S. Tanaka, "Direct Modulation at 56 and 50 Gb/s of 1.3 μm InGaAlAs Ridge-Shaped-BH DFB Lasers", IEEE Photonics Technology Letter, vol. 27(5), (2015).

[39] D. M. Kuchta, F. E. Doany, L. Schares, C. Neumeyr, A. Daly , B. Kögel, J. Rosskopf, and M. Ortsiefer, "Error- free 56 Gb/s NRZ Modulation of a 1530 nm VCSEL Link", postdeadline paper ECOC2015, Valencia, Spain, (2015).

[40] R. S. Tucker, "Green Optical Communications – Part I: Energy Limitations in Transport", IEEE Journal of Selected Topics in Quantum Electronics, vol. 17, pp. 245-260, (2011).

[41] Y. Malsui, H. Murai, S. Arahira. S. Kutsuzawa. and Y. Ogawa, "30-GHz bandwidth 1.55-µm strain compensated InGaAIAs-InGaAsP MQW laser", IEEE Photonics Technology Letter, Vol.9(25), (1997).

[42] U. Feiste, "Optimization of Modulation Bandwidth or DER Lasers with detuned Bragg reflectors", IEEE Journal of Quantum Electronics, vol.34, pp.2371, (1998).

[43] T.B. Simpson and J.M. Liu, "Enhanced Modulation Bandwidth in Injection-Locked Semiconductor Lasers", IEEE Photonics Technology Letter. vol. 9, pp. 1322, (1997).

[44] D. D. Marcenac, M. C. Nowell, and J. E. Carroll, "Theory of enhanced amplitude modulation bandwidth in push-pull modulated DFB lasers", IEEE Photonics Technology Letter., vol. 6, pp. 1309-1311, (1994).

[45] J. P. Reithmaier , W. Kaiser , L. Bach , A. Forchel , V. Feies , M. Gioannini , I. Montrosset , T. W. Berg and B. Tromborg, "Modulation speed enhancement by coupling to higher order resonances: A road towards 40 GHz bandwidth lasers in InP", Proc. Int. Conf. Indium Phosphide Related Mater. (ICIPRM), pp. 118-123, (2005).

[46] G. Morthier , R. Schatz and O. Kjebon, "Extended modulation bandwidth of DBR and external cavity lasers by utilizing a cavity resonance for equalization", IEEE Journal of Quantum Electronics, vol. 36(12), pp. 1468-1474, (2000).

[47] P. Bardella and I. Montrosset, "A New Design Procedure for DBR Lasers Exploiting the Photon–Photon Resonance to Achieve Extended Modulation Bandwidth", IEEE Journal of Selected Topics in Quantum Electronics, vol. 19(4), pp. 1502408-1502408, (2013).

[48] H. Wenzel , U. Bandelow , H.-J. Wünsche and J. Rehberg, "Mechanisms of fast self-pulsations in two-section DFB lasers", IEEE Journal of Quantum Electronics, vol. 32(1), pp. 69-78, (1996).

[49] O. Brox , S. Bauer , M. Radziunas , M. Wolfrum , J. Sieber , J. Kreissl , B. Sartorius and H.-J. Wünsche, "High-frequency pulsations in DFB-lasers with amplified feedback", IEEE Journal of Quantum Electronics, vol. 39(11), pp. 1381-1387, (2003).

[50] S. Bauer , O. Brox , J. Kreissl , B. Sartorius , M. Radziunas , J. Sieber , H.-J. Wünsche and F. Henneberger,"Nonlinear dynamics of semiconductor lasers with active optical feedback ", Physical Review E, vol. 69, (2004).

[51] A. Tager and K. Petermann, "High-frequency oscillations and self-mode locking in short external-cavity laser diodes", IEEE Journal of Quantum Electronics, vol. 30(7), pp. 1553-1561, (1994).

[52] M. Radziunas et al., "Improving the Modulation Bandwidth in Semiconductor Lasers by Passive Feedback," IEEE Journal of Selected Topics in Quantum Electronics, vol. 13(1), pp. 136-142, (2007).

[53] C. Henry, and R. Kazarinov. "Instability of semiconductor lasers due to optical feedback from distant reflectors." IEEE Journal of Quantum Electronics, vol. 22(2), pp. 294-301,(1986).

[54] A. Zadok, H. Shalom, M. Tur, W. D. Cornwell, and I. Andonovic, "Spectral shift and broadening of DFB lasers under direct modulation," IEEE Photonics Technology Letter, vol.10, pp. 1709-1711, (1998).

[55] D. Mahgereften, D. Mahgerefteh, Y. Matsui, C. Liao, B. Johnson, D. Walker,X. Zheng, Z. F. Fan, K. McCallion, and P. Tayebati, "Error-free 250 km transmission in standard fibre using compact 10 Gbit/s chirpmanaged directly modulated lasers (CML) at 1550 nm," Electron. Lett,vol. 41, pp. 543–544, (2005).

[56] D. Mahgerefteh, Y. Matsui, X. Zheng, K. McCallion, "Chirp managed laser and applications", IEEE Journal of Selected Topics in Quantum Electronics, vol. 16(5), pp. 1126, (2010).

[57] H. Zhao, S. Hu, J. Zhao, Y. Zhu, Y. Yu, and L. P. Barry, "Chirp-Compensated DBR Lasers for TWDM-PON Applications," IEEE Photonics Journal, vol. 7(1), 7900809, (2015).

[58] J. Yu et al., "Applications of 40-Gb/s Chirp-Managed Laser in Access and Metro Networks", Journal of Lightwave Technology, vol. 27(3), pp. 253-265, (2009).

[59] R. Asif, C. Lin, M. Holtmannspoetter, and B. Schmauss, "Evaluation of correlative coding and DP-16QAM n-channel 112Gbit/s coherent transmission: digital non-linear compensation perspective," Optics Express, vol. 21, pp. 781-788, (2013).

[60] https://en.wikibooks.org/wiki/Communication_Systems/Line_Codes

[61] Interim Atlanta, GA, USA. Moving Forward. [Online]. Available: http://www.ieee802.org/3/bs/public/15_01/   ambrosia_3bs_01_0115.pdf, accessed Jan. (2015).

[62] T. Hyder, "Comparison between Duobinary Filter and Delay-And-Add Technique of Duobinary Transmission in Fiber Optic Communication System", IOSR Journal of Electronics and Communication Engineering, vol. 9(3), (2014).

[63] A. Rahman, M. Broman and M. Howieson, "Optimum Low Pass Filter Bandwidth for Generating Duobinary Signal for 40 Gb/S Systems", Thin Film Technology Corp. Commerce Drive, North Mankato, MN, 56003, USA, (1980).

[64] A. Kamran, E. F. Haratsch, H. Kim, F. Saibi, J. H. Saunders, M. Shaffer, L. Song and M. Lin Yu. "Equalization and FEC techniques for optical transceivers." IEEE Journal of Solid-State Circuits, vol. 37(3),, pp. 317-327, (2002).

[65] Bulow, Henning. "Electronic equalization of transmission impairments."Optical Fiber Communication Conference and Exhibit, 2002. OFC 2002. IEEE, (2002).

[66] Ransom Stephens Equalization: The Correction and Analysis of Degraded Signals, Agilent, V1.0 15-August-(2005).

[67] Kschischang, Frank, and Benjamin P. Smith. "Forward error correction (FEC) in optical communication." In Conference on Lasers and Electro-Optics, p. CThDD1. Optical Society of America, (2010).

3

# Development and optimization of III-V-on-silicon laser fabrication

In this chapter, a description of the standard fabrication procedure for heterogeneously integrated InP on SOI DFB lasers will be provided. First of all, an overview of the DFB laser based on adhesive bonding which is developed in the UGent Photonics Research Group is presented. In the rest of the chapter, the fabrication process flow together with details on each step are described. Optimizations and improvements are provided which have been developed during this PhD. The epitaxial layer structures that are used in this project will be discussed.

3.1 DFB structure overview & optical design

3.1.1 Laser structure

A typical heterogeneously integrated DFB laser on the Si-on-insulator (SOI) platform is shown schematically in Figure 3.1. A rib waveguide and DFB grating are patterned on a 400 nm thick Si device layer by a 180 nm deep dry etch using 193 nm deep UV lithography after which the Si waveguide layer is planarized. A thin DVS-BCB layer is used to bond III-V materials on top of the SOI. The III-V is etched down to the n-InP to create an active waveguide on top of the Si waveguide. A thick BCB layer covers the laser entirely to serve as a passivation layer and also provides a planarized surface for the metal pads.

Metallization pads are arranged in a GSG format to enable a high speed probing
After the laser emission is coupled to the 400 nm thick silicon waveguide layer,
a second spot-size converter is used to couple to a 220 nm strip waveguide. Two
grating couplers are patterned on the Si passive waveguide to couple the laser
optical power out through an optical fiber.
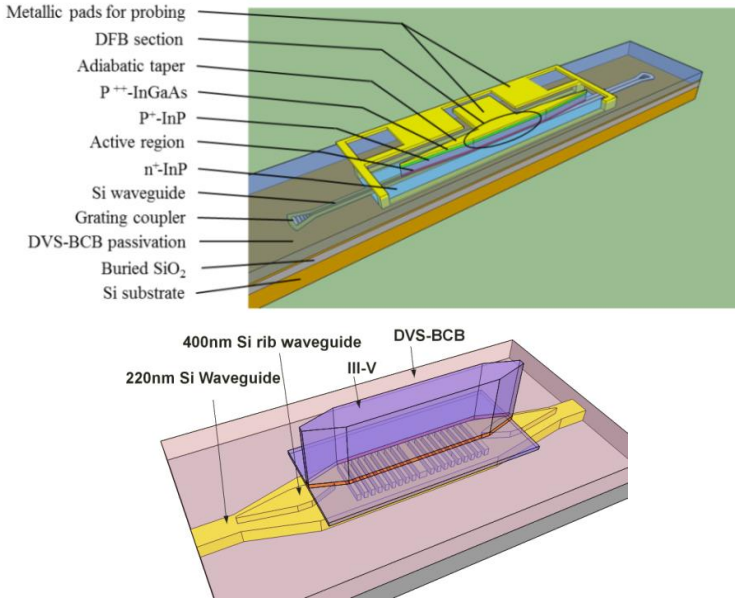
Figure 3.1: Schematic 3D representation of the heterogeneously integrated DFB laser
(a), close-up of the laser structure (b).

3.1.2 Optical design

In order to get an idea about the guided mode profile in this heterogeneously
integrated structure, the cross section of the device is depicted in Figure 3.2. The
active waveguide is 3μm wide. The III-V epitaxial layer stack that is used for
these simulations consists of a 200 nm thick n-InP contact layer, two 100 nm
thick InGaAsP separate confinement heterostructure layers, six InGaAsP
quantum wells (8 nm thick) surrounded by InGaAsP barriers (10 nm thick), a
1.5 μm thick p-InP top cladding, and a 300 nm InGaAs contact layer. The mode
profiles are calculated using the mode matching method [1]. The thick p-InP
cladding is used to keep the optical mode away from the highly absorbing
InGaAs contact layer. The guided mode is a hybrid mode meaning that the mode
is partially confined in the III-V waveguide and partially in the Si waveguide.
The confinement of the mode in the quantum wells is an important parameter to
realize a high speed directly modulated laser. This is because it appears directly
in the formula of the relaxation oscillation frequency, but also because a high
confinement results in a low threshold carrier density and a high differential gain
(section 2.2.1). The bonding thickness variation during fabrication gives one

degree of freedom to play with the confinement factor in the QWs and the Si waveguide. The dependency of the confinement factor in the QWs (Γ_{QW}) and in the Si waveguide (Γ_{Si}) on the bonding layer thickness and the n-InP thickness is shown in Figure 3.3.
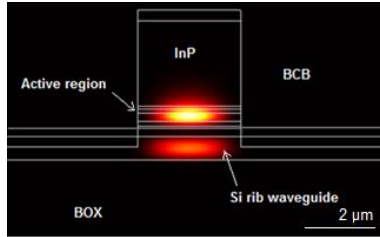
Figure 3.2: The guided mode profile in the cross section of the heterogeneously integrated DFB laser.
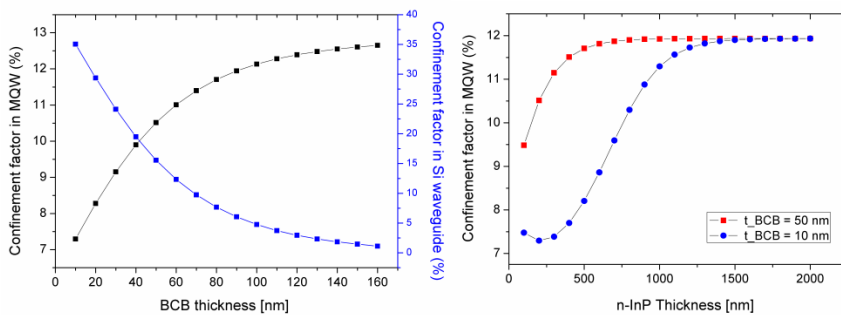
Figure 3.3: The simulated confinement factor of 6 InGaAsP MQW versus the BCB bonding thickness (left) and versus n-InP thickness (right).

When the bonding layer thickness increases the mode shifts to the active waveguide and the confinement factor of the active region rises. For instance, for a 50 nm bonding layer thickness the confinement factor in the quantum wells is 10.5 % (1.75% per QW). In this case the mode mostly sits in the active III-V waveguide and the confinement factor in the Si waveguide decreases to about 9.5% (Figure 3.3-left). In Figure 3.3-right, we have compared the confinement factor in the QWs where the transition from the heterogeneously integrated laser to a pure InP laser is emulated by increasing the n-InP thickness. In this way, we can compare the two platforms with the same geometries. One can see that the confinement factor increases as the n-InP layer thickness increases for both BCB bonding thickness of 10 and 50 nm and it saturates around 12%.

In general, for a heterogeneously integrated DFB laser, the coupling coefficient can be higher (because of the high index contrast in the SOI grating section) while the confinement factor in the QWs is comparable with a laser on an InP platform, especially for the case of 50 nm BCB thickness.

The high confinement in the III-V waveguide makes coupling of the light from the active waveguide to the Si more difficult. This optical coupling is realized using a III-V/silicon spot-size converter structure defined by tapering both the

III-V and silicon waveguide as shown in Figure 3.4. The total III-V taper length is 200 µm and consists of two parts. In the first part the III-V waveguide is tapered down from 3 µm to 1 µm (section between I and II) whereas the second part tapers from 1 µm to a taper tip of 600 nm (section between II and III). The underlying silicon rib waveguide tapers from 300 nm to 2 µm over a length of 150 µm. This taper coupling section is implemented outside the laser cavity, which means that the taper structure has no impact on the internal loss (and hence the threshold current density) of the DFB laser. As we will see in chapter four, damage to the taper section only decreases the out-coupled light without any influence on the laser's dynamic and static performance.

In order to ensure a high coupling efficiency and a low reflection at the transition interfaces, the taper tips should be as narrow as possible. For the Si waveguide, a very narrow taper tip (< 300 nm) can be fabricated using 193 nm deep UV lithography.
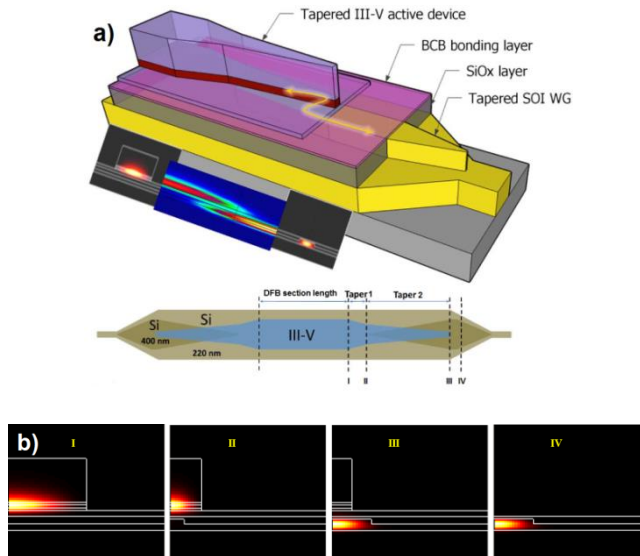
Figure 3.4: Spot-size converter structure consisting of two inverted taper sections (a), the first one for coupling the light from III-V waveguide to the 400 nm thick Si waveguide and the second one to couple the light from 400 nm thick Si to the 220 nm Si waveguide. The light coupling mechanism from III-V active waveguide to the Si passive waveguide at different positions of the coupling taper (b) [2].

On the other hand, a narrow III-V mesa tip (< 700 nm) is difficult to realize with 300 nm UV contact lithography. However the wet etching of the III-V mesa, which will be discussed later in this chapter, allows creating a negative slope in the spot size convertor, which again relaxes the lithography requirements in the definition of the III-V taper tip (Figure 3.5).

Another parameter that can be optimized for the efficient coupling is the inverted taper section length (section between II and III in Figure 3.4-a). A long gradual tapering of the III-V waveguide ensures that the optical mode is

adiabatically coupling to the Si passive waveguide. Figure 3.6 shows the coupling efficiency of the fundamental TE-mode of the III-V waveguide to the fundamental TE-mode of the Si rib waveguide versus the second taper length, for different thicknesses of the bonding layer. For the thin 50 nm BCB thickness this coupling saturates after 150 μm of taper length.
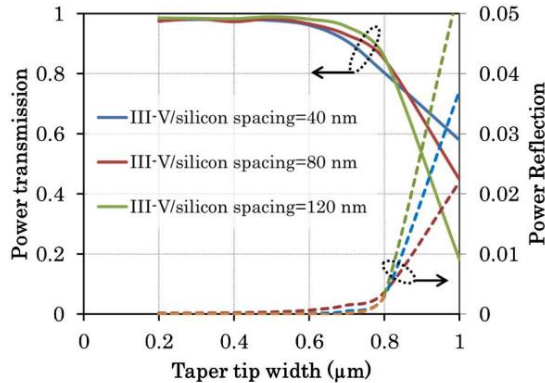
**Figure 3.5:** Simulated power transmission and reflection at the spot-size converter taper tip as a function of III-V taper tip width [2].
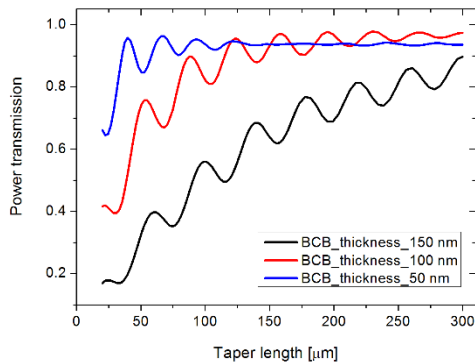
Figure 3.6: Taper coupling efficiency versus taper length for different values of the BCB bonding thickness for the taper tip width of 600 nm.

In general, the same simulations can be done for the second epitaxial stack consisting of 8 InGaAlAs QWs which has been used in this PhD work. From these simulations, one can conclude that more than 90% power transfer with low reflection can be realized using this spot size convertor approach, the remaining 10% power is believed to transfer to the higher order modes at the interfaces.

These simulations can be used for further optimization and more elaborate design cases. It is important to note that these simulations approximate the fabricated devices and sometimes the simulation results do not exactly correspond to the experimental results. Accurate thicknesses and refractive indices are not easy to estimate.

3.2 Process flow

A brief outline of the fabrication process is illustrated in Figure 3.7. Main steps are the SOI waveguide circuit fabrication, the III-V growth, the bonding and post processing on the hybrid structure. After designing the SOI which includes waveguides, DFB gratings and grating couplers (Figure 3.7-a), the III-V epitaxial stack, which is grown on a 2 inch InP wafer, is bonded on it by a thin layer of DVS-BCB (Figure 3.7-b) [3, 4]. The next steps are combinations of dry and wet etching to define the III-V mesa and isolate individual devices (Figure 3.7-c). N and P contact metallization are realized on the n-InP and the P-InGaAs surfaces respectively (Figure 3.7-d). Then a thick DVS-BCB layer is spin coated to passivate the device and also provide a flat area for metal pads. The pads' metallization is the final process step. This is the standard fabrication process flow for a heterogeneously integrated DFB laser. These steps are modified for different practical reasons to improve the laser performance and will be described in the rest of this chapter.
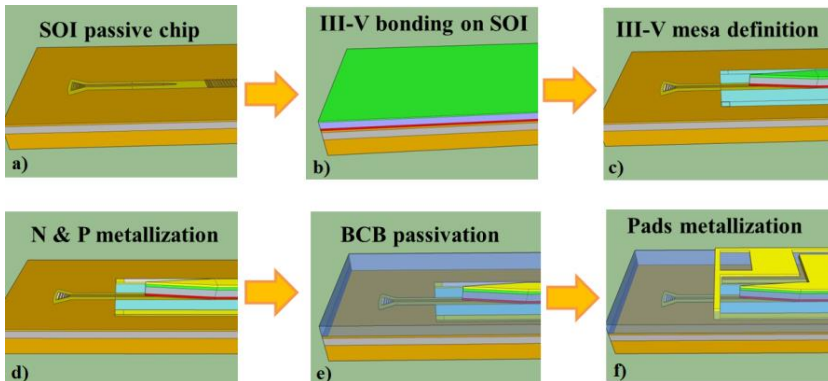
Figure 3.7: Standard process flow of the DFB laser fabrication.

3.3 Standard fabrication steps for heterogeneously integrated DFB lasers

In this section, we review in detail the fabrication steps mentioned above. They consist of the SOI waveguide circuit fabrication and preparation before bonding, the III-V die preparation, the BCB adhesive bonding and the III-V post-processing to form a DFB laser.

3.3.1 SOI preparation

The DFB gratings are defined in a 400 nm thick silicon waveguide layer by a 180 nm deep dry etch, using 193 nm deep UV lithography. The use of a 400 nm Si waveguide in the laser section simplifies the optical coupling between the III-V mesa and the silicon waveguide layer. Details about this SOI platform can be found in ref. [2]. The SOI wafer normally is not diced and is planarized leaving 100 nm SiO_2 on top of the waveguides. The preparation starts with cleaving a 200 mm SOI wafer. Before the cleaving, a thin layer of photoresist can be spin coated to protect samples from small Si particles (by- products of the cleaving). The DFB structures should be in the center of the die and enough margin (in our case using a die size of 2cm*2cm) should be considered for the sample handling during fabrication and for alignment markers. The protective photoresist is removed using acetone and iso-propyl alcohol (IPA). The remaining organic contamination can be removed by a 10 min O_2-plasma etching in a Reactive-Ion Etching (RIE) tool.

The separation between III-V and Si can be varied by etching the top SiO_2 cladding layer by dipping the sample in a BHF solution. The sample prior to the bonding should be kept in a closed box to avoid any contamination, otherwise the bonding failure risk will increase.

3.3.2 III-V preparation

The epitaxial layer structures are grown on a 2 inch InP wafer (300 μm thick). A typical InP structure is shown in Figure 3.8. To protect the wafer from contamination before cleaving, a thin layer of photoresist is coated on it. Depending on the size of the target SOI waveguide circuit, a small piece (in our case 1cm*1cm) of the III-V wafer is cleaved. In order to protect the epitaxial layers, two sacrificial layers are grown on each side of the epi stack. These layers normally are thin films (100 nm) of InP and InGaAs which can be selectively etched away by a HCl and a H_2SO_4 based solution respectively.
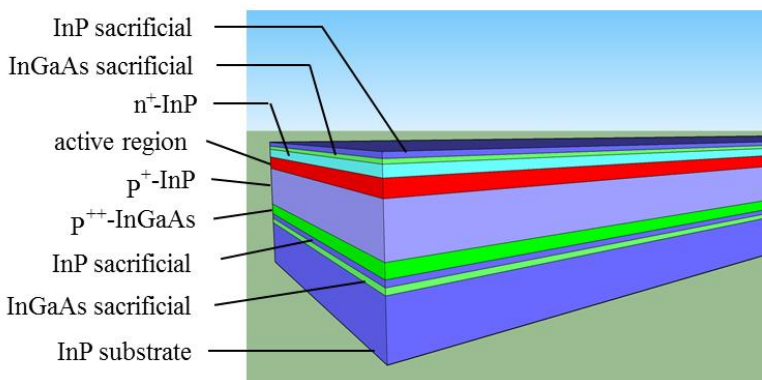
Figure 3.8: Schematic representation of the typical InP epitaxial stack.

The two top sacrificial layers are removed by wet etching prior to bonding. III-V wafers are very fragile; therefore for handling small pieces a plastic tweezer can be used. The adhesion between III-V die and BCB layer can be improved by the deposition of a thin layer of SiO_2 (less than 10 nm) in a PECVD chamber on the III-V die. Now, the die is ready for bonding.

3.3.3 Adhesive bonding

For integration of an InP epitaxial layer structure onto an SOI waveguide wafer, there are various methods. The most important ones are molecular bonding [5] and adhesive bonding [2, 4]. Adhesive bonding provides several significant advantages over the other bonding methods. Surface preparation of both SOI and InP dies can be reduced because of the relaxed requirements on surface cleanliness, contamination and surface roughness combined with the planarizing action of the adhesive spin coating process. In addition, the integration process is a low-temperature process, reducing the stress in the bonded stack due to the difference in thermal expansion coefficients between silicon and III-V semiconductor.

DVS-BCB (divinylsiloxane-bis-benzocyclobutene) is a good candidate for die to wafer bonding because of its beneficial properties such as low dielectric constant, low moisture absorption, low curing temperature, high degree of planarization, low level of ionic contaminants, high optical clarity, good thermal stability, excellent chemical resistance, and good compatibility with various metallization systems [6, 7]. The drawback of BCB is its low thermal conductivity. In table 3.1, the thermal conductivity of several materials is shown. It is obvious that BCB has the lowest thermal conductivity of all materials that are involved in the fabrication of a heterogeneous integrated DFB laser.

Table 3.1: Thermal conductivity of some materials which were used in this project.

Materials	Thermal conductivity ($W.m^{-1}.K^{-1}$)	Reference
Au	315	[8]
Si	149	[9]
InP	63	[10]
Si_3N_4	16-33	[9]
SiO_2	1.4	[9]
BCB	0.29	[11]

The bonding procedure begins by spin coating a thin layer of a BCB solution on the SOI sample. This solution consists of 1 volume of Dow Chemical's Cyclotene 3022-35 solution and 8 volumes of Mesitylene. The spin coating can be done in two steps at 500 RPM and then at 3000 RPM in order to have good planarization. Using a pre-defined BCB solution and the correct spin velocity

one can realize the desired bonding thickness in a reproducible way. For example, with the above mentioned numbers, a bonding thickness of 40-50 nm is achieved [12]. The BCB thickness can be checked after bonding using Focused Ion Beam (FIB) milling and Scanning Electron Microscope (SEM) imaging.

Next, the SOI substrate is baked for 10 min at 150 °C, to let mesitylene evaporate, after which the substrate is slowly cooled down to room temperature in 20 min. Finally, the SOI is mounted on a carrier wafer made of Pyrex glass (1200 um thick, 100 mm diameter). Then the clean III-V die is flipped on the SOI die. After that, the SOI substrate on its carrier wafer is mounted on the transport fixture (Figure 3.9-a) and is loaded into the processing chamber of the wafer bonding tool (Figure 3.9-b). The chamber is pumped-down and heated to 150°C with a ramp of 15 °C/min for 10 min, while applying pressure on the III-V/SOI stack. The actual bonding pressure (the applied force per unit area of the III-V die) is kept in the range of 200 to 400 kPa. After keeping the pressure on the dies for 10 min at 150 °C, the temperature is increased up to 280 °C, with a ramp of 1.5 °C/min. Upon reaching 280 °C, the dies are kept at this temperature for 60 min in a nitrogen atmosphere. After the curing, the bonded samples are cooled down (at 6-10 °C/min) and unloaded from the processing chamber. A photograph of a bonded sample is shown in Figure 3.9-c. The next step is to remove the thick InP substrate (Figure 3.9-d).
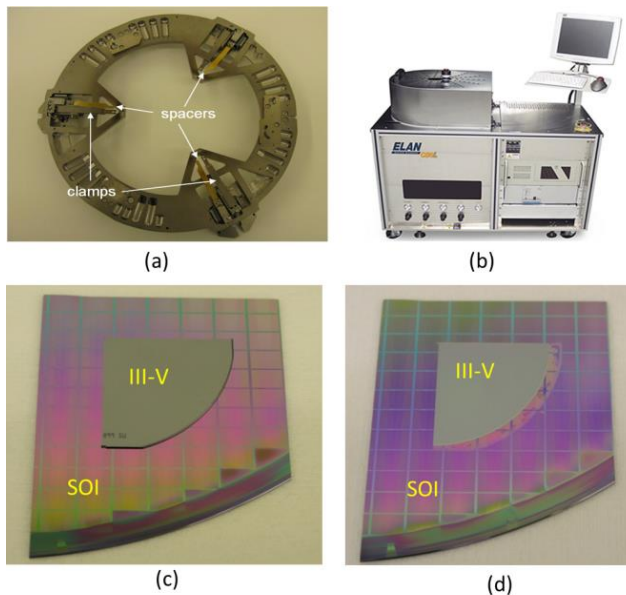
Figure 3.9: Süss Microtec ELAN CB6L wafers bonder: a) transport fixture for handling 100 mm diameter wafers b) front view of the bonder with the control PC (c), a photograph of a bonded sample before substrate removal step; (d) after substrate removal [13].

3.3.4 Substrate removal

After bonding, the 300 μm thick InP substrate is etched away by immersing the sample in a 1:3 HCl:H$_2$O solution. In order to speed up the etching process and decrease the chance of "ear creation" on the III-V bonded die (Figure 3.10-a), the solution can be heated up to 40-45 ℃. Under this condition, after 15 min the substrate is removed totally and the etching will finish on the InGaAs etch-stop layer. Following the substrate removal, the 100 nm etch stop layer is removed by a 1:1:18 H$_2$SO$_4$:H$_2$O$_2$:H$_2$O solution in 30 seconds. In this step, one can trace a color change on the surface of the die as a good indicator of the etching process. Finally, the 100 nm InP sacrificial layer is etched by pure HCl in 20 seconds. Sometimes defects on the III-V epitaxial structure can be seen in this step (Figure 3.10-b).
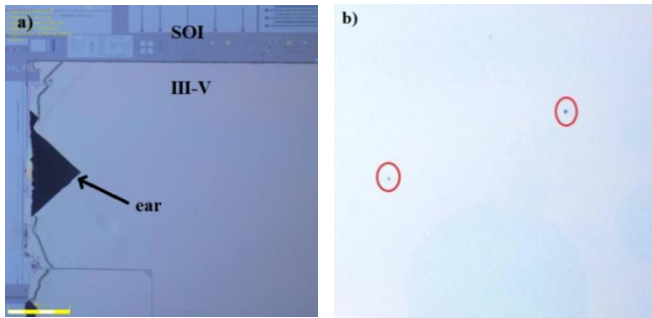
Figure 3.10: Ears creation (black in color) during the substrate removal on the side of the bonded die (a), defects on the InP epitaxial structure after substrate removal (b)

3.3.5 Mesa definition

After removing the sacrificial layers, the next processing step is defining the III-V waveguide (mesa). This step can be done in two different ways. We can use a metal mask so that a top metallization (P contact) is deposited first which can also serve as a mask for etching the remaining III-V stack. Another way is the deposition of a thin layer (200 nm) of SiNx by PECVD as a hard mask. We found that working with the hard mask is less complex and reduces the risk of fabrication failure. Using a metal mask should provide a better p-contact resistivity than a hard mask, but we did not see any noticeable difference. For all the samples that we report in this work we used a hard mask. The hard mask deposition is performed at 280 ℃.

Sometimes during bonding air gets trapped between the SOI and the III-V die. Then exposure of the sample to a high temperature during the SiNx hard mask deposition leads to a rapid expansion of the trapped gases which eventually can damage the bonded III-V film. To prevent air bubble extension one can scratch them with a scalpel (Figure 3.11-a, b).
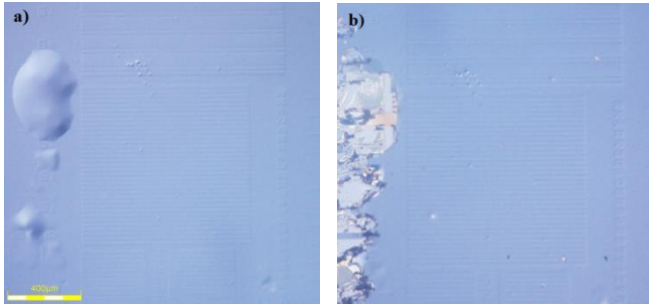
Figure 3.11: Air bubble inflation (a), scratching them away by a scalpel (b).

Following this, a lithography is carried out using MIR-701 as a positive photoresist. The mesa lithography is a critical process. A good alignment (less than 200 nm) and clean surface are essential requirements for a heterogeneously integrated DFB laser fabrication. If there is any particle or topography on the sample, the bad contact between the sample and the glass mask would result in a wide mesa tip (Figure 3.12).
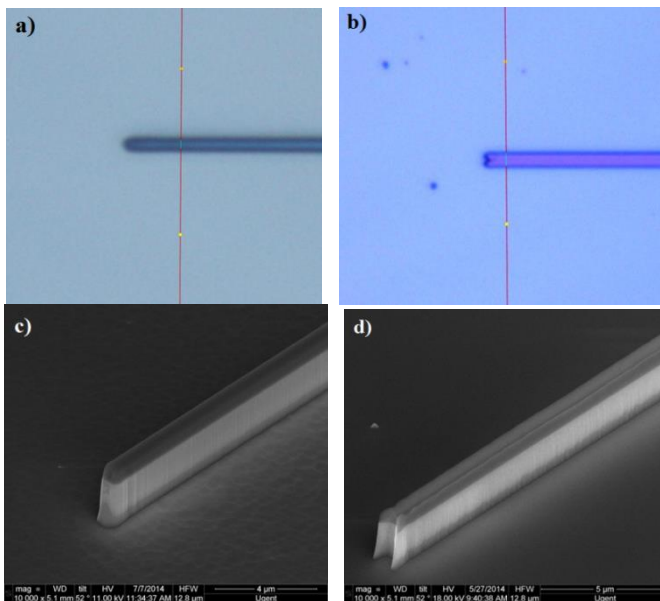
Figure 3.12: A successful narrow-tip mesa lithography (a, c), a bad contact leads to a wide mesa tip (b, d).

After developing the sample, the photoresist acts as soft mask to etch the deposited SiNx layer in a reactive ion etching (RIE) tool. The contact layer (InGaAs) is etched preferably with Inductively Coupled Plasma (ICP). This dry etching is not selective, but over etching of the stack will not harm, since the underneath InP layer is a thick layer (1500 nm). Using a HCl:H_2O 1:1 solution

at room temperature will etch selectively this thick InP layer with negative slope (Figure 3.13) with an etch rate of 100 nm/min, when the mesa is oriented along the [100] crystal axis. This V-shaped mesa provides an effective optical and electrical confinement. Furthermore this shape contributes to narrow taper-tips on the bottom of the mesa and consequently couples light more efficiently to the underlying Si waveguide circuit.
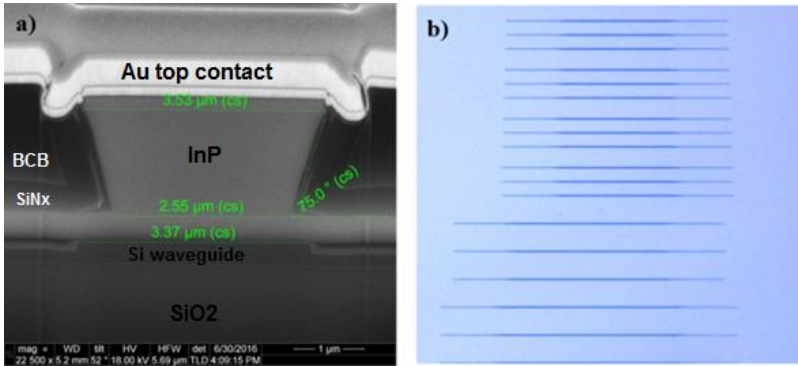
Figure 3.13: SEM image of the laser's cross section, a V-shape mesa is created with an angle of 75° (a), a top microscopic view of the mesas (b).

3.3.6 Etching of active layer

This step can be done in two different ways. The simplest method is to use the mesa mask and continue etching the active layers without any lithography. But in this case, a large undercut during wet etching can damage the narrowest part of the mesa, i.e. the tapers (Figure 3.14-a). To solve this problem we perform a dry etching prior to the wet etching to reduce the undercut. This technique will be explained in detail in section 3.4.3. Another way to deal with this problem is to define a wider mask than the mesa mask by lithography to make sure that the undercut will not damage the mesa (Figure 3.14-b).

After the p-InP etching the top layer of the active region (SCH, QWs, barriers) is exposed. Depending on the epitaxial structure the top layer can be InGaAsP or InGaAlAs. Therefore two different solutions are used to etch these layers. For the InGaAsP samples, an isotropic $H_2SO_4:H_2O_2:H_2O$ 1:1:10 solution was used. 2 min. etching is enough to remove the 300 nm thick InGaAsP layer, which makes a lateral undercut on this layer (Figure 3.14-b). However this solution can etch the ohmic InGaAs contact layer much faster than the InGaAsP layer. Thus before this etching step, the contact layer must be protected with a thin layer of SiNx (see section 3.4.2). For the InGaAlAs stack, a $H_3PO_4:H_2O_2:H_2O$ 1:1:20 solution is used to etch the layers.

The selective etching will stop on top of the n-InP layer. Then the sample is rinsed with DI water and dried.
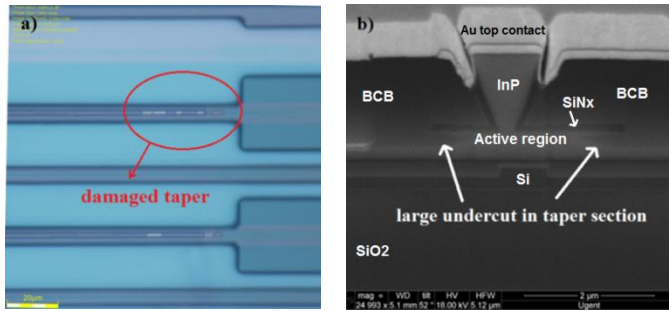
Figure 3.14: A long wet etching can damage the tapers (a), SEM image of a lateral undercut on the InGaAsP active layers by a H_2SO_4 based solution (b).

3.3.7 N-contact metallization

In this stage, the n-type InP layer is clean and the metallization should be done immediately. The lithography is performed with a relatively thick layer (3µm) of TI35 photoresist used as an image reversal photoresist. The thicker layer of photoresist enables an easier and more reliable lift-off procedure. After developing the photoresist, first a 30 seconds O_2-plasma in an RIE tool is performed to remove potentially remaining photoresist. Next, the sample is immersed for few seconds in a diluted Piranha solution $H_2SO_4:H_2O_2:H_2O$ 1:1:20 in order to etch away the native oxide formed on top of the InP layer. The metallic layers are deposited using an evaporation/sputtering system. First, 30 nm nickel (Ni) is deposited, followed by deposition of 20 nm germanium (Ge) and 50 nm of gold (Au).

A lift-off procedure is performed after the metallization by dipping the sample in acetone for 15 to 20 minutes, after which the sample is rinsed and dried. A microscope image of the sample after this processing step is shown in Figure 3.15.
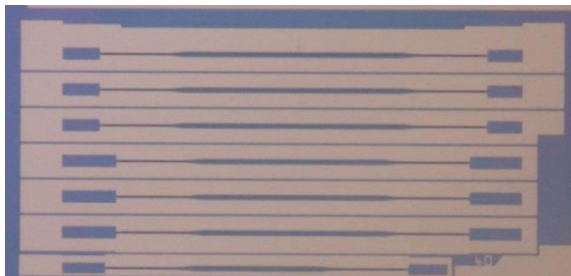
Figure 3.15: Microscopic image of the sample after N contact metallization.

3.3.8 Island definition

The next processing step, island definition, is performed to electrically isolate the lasers from each other. A wide area (including the n-contacts on both sides of the lasers) is patterned by an AZ9260 positive photoresist. Since the mesa thickness is around 2 μm, this thick photoresist can easily cover this topography. After developing the resist, the sample is dipped in a HCl:H$_2$O 1:1 solution for 2-3 min to etch the 200 nm thin InP layer. Then the sample is rinsed in DI water and dried. Now, all III-V layers are etched away and the SOI structures underneath are visible (see Figure 3.16).
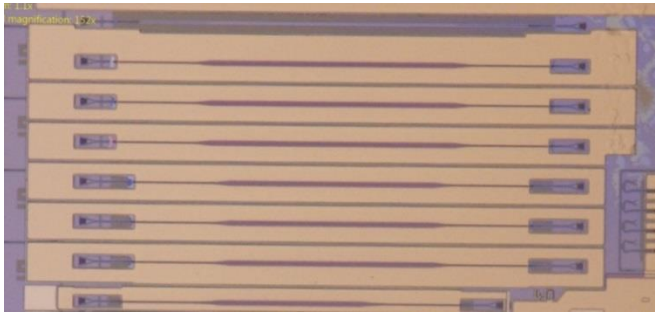
Figure 3.16: After the island definition, grating couplers are visible.

3.3.9 Passivation

After the n-type metallization, the passivation is performed. This is realized by spin coating a thick protective layer of DVS-BCB on the sample. This layer later provides an electric insulation between the p-contact on the top and the n-electrodes located below. For this purpose, an undiluted Cyclotene 3022-57 resin is spin-coated (at 2000 rpm) on the sample and cured in an oven at 280℃, according to a standard DVS-BCB curing procedure. Spin-coating at this rotation speed provides an approximately 7 μm thick cured BCB layer. Although the topography of the sample is not flat before passivation (approximately 2 μm), this method provides usually 50 nm topography after passivation. This height difference can easily be checked during fabrication with a profilometer. Using this tool to check the topography together with a microscope makes the fabrication processes much more reliable.

3.3.10 P-contact metallization

In order to reach to the top of the mesas, which is now covered with the thick BCB film, a RIE dry etching is performed. The etch rate of the BCB layer using a mixture of SF$_6$:O$_2$, 50:5 is 400 nm/min. After a 12 min long etch, measuring

with the profilometer reveals that the top InGaAs layer is exposed. We can use a thin photoresist AZ5214E for image reversal lithography to define the p-contact patterns. Following the resist development, the sample is loaded in the RIE tool for a 30 second to remove residual photoresist using O_2 plasma. Next, the sample is immersed in a $H_2SO_4:H_2O_2:H_2O$ 1:1:20 solution for a few seconds to remove the native oxide.

After rinsing the sample with DI water and drying, the sample is loaded into a Leybold Univex system for metal deposition. A 40nm-thick layer of Titanium is sputtered on the sample, followed by thermal evaporation of a 150 nm-thick layer of gold. Once the deposition is completed, the sample is dipped into acetone for the lift-off procedure. As for any lift-off process, the edges of the photoresist need to have inverted slopes. Also, it is essential to have a sufficiently thick layer of photoresist prior to metal deposition. After the lift-off is completed, the sample is rinsed and dried (Figure 3.17).
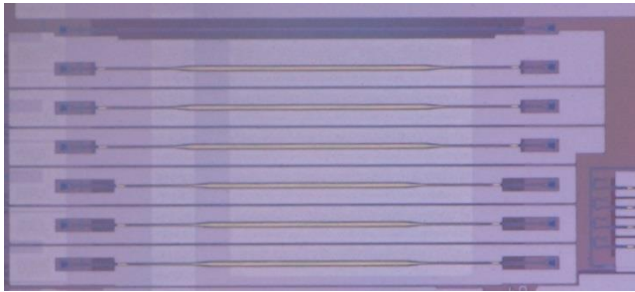
Figure 3.17: Microscopic image after the p contact metallization.

3.3.11 Pads metallization

After the p-contact metallization, the processing continues with the etching of windows on the n-contact which is covered by a 2 µm BCB layer. The lithography is performed with a thick TI35 photoresist layer (3 µm) and the sample is loaded into the RIE chamber. Dry etching of the BCB is performed with the same recipe as we used in a previous step, with a 50:5 $SF_6:O_2$ gas mixture. This process takes 5 min to finish. Over-etching will not harm since the layer underneath is a gold film. During etching test structures can be used to get the etch rate and thickness of the remaining BCB. When we are sure that the BCB is completely removed, the sample is rinsed with acetone, IPA and DI water. A microscopic image of the devices after this processing step is shown in Figure 3.18.

Opening of the windows in the BCB layer for n-contact metallization is followed by the final metallization step. In order to have metallic pads to electrically probe the lasers, a thick metallization is performed. The same lithography steps are followed as for the p-contact metallization with the

AZ5214 photoresist. Before the metal layer deposition, the sample is loaded in the RIE chamber to clean photoresist residuals as we did during n and p contacts metallization. The metallization consists of sputtering a 40nm-thick layer of titanium, followed by thermal evaporation of an 800nm-thick layer of gold. As in the previous metallization steps, the lift-off procedure is performed in acetone and can take up to 30 minutes.
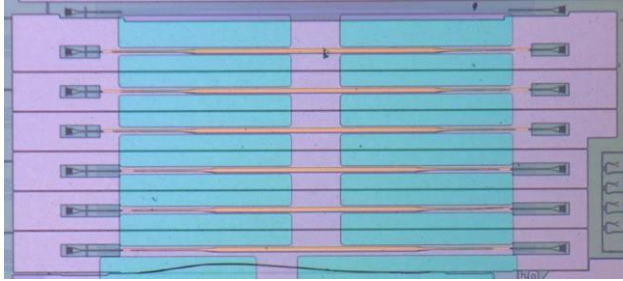
Figure 3.18: Microscopic image after N-contact via opening.

This is the last step of the standard laser fabrication processes. A fast annealing or gold plating can be done as complementary processing, but we did not do this in this work. A microscope image after the lift-off is depicted in Figure 3.19.
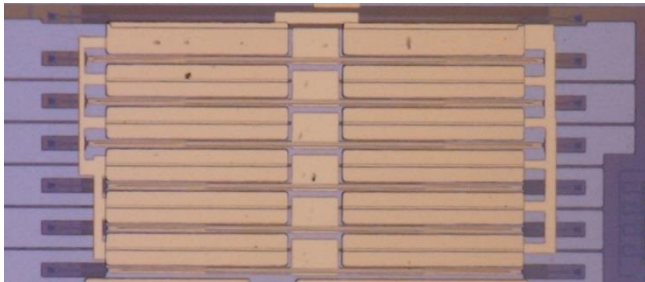
Figure 3.19: Microscopic image of the sample after the final pads metallization.

3.4   Fabrication improvements

During this PhD and in collaboration within the Photonics Research Group-UGent, we have developed techniques to improve the DFB laser fabrication. Since some of these techniques are completely different processes we provide them separately in this section. These methods can be used in other heterogeneously integrated devices such as modulators or photodiodes as well.

3.4.1 Thin bonding technique

The adhesive bonding with BCB brings flexibility to the DFB laser fabrication. Except the advantages that we mentioned in the bonding section about relaxed surface requirements, the bonding layer thickness can be optimized for different applications. The thickness can be controlled by the spinning speed or by the solution's concentration. Practically it is difficult to have a bonding thickness below 40 nm, because this increases the bonding failure risk.

Normally for an SOI wafer that we receive from foundries like Imec or CEA-Leti, there is a layer of SiO_2 on top of the waveguides. Before bonding, this layer can be thinned down by etching with a BHF solution to get the desired thickness or even totally remove it on top of a Si waveguide. One can continue the etching and even remove 30 nm of the SiO_2 in the trenches. As a result of this etching, with the same BCB solution (1:8), we can achieve a separation between III-V and Si of less than 10 nm (Figure 3.20). Further etching of the SiO_2 will not be useful, as air voids can be created compromising the following processes.

For a DFB laser a thin bonding layer leads to a high coupling coefficient. This is because the overlap of the optical mode with the grating increases. A DFB laser with a higher coupling coefficient can be a short laser. In order to reduce the power consumption, a short cavity DFB (SC-DFB) is preferred to minimize the threshold current, and enhance the wall-plug efficiency. Another advantage of shortening the cavity length is that it improves the high speed performance for direct modulation [13, 14].
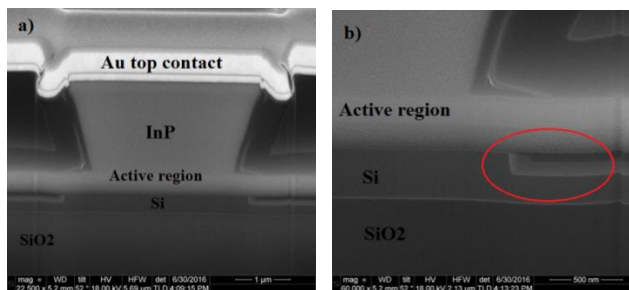
Figure 3.20: SEM image of a DFB laser cross section with an ultra-thin bonding thickness (a) zoom-in image shows over etching of the SiO_2 in the trench (b).

## 3.4.2 SiNx as a protection layer for the InGaAs contact layer

For samples with InGaAsP active region, a H_2SO_4-based solution is used to etch the active region. This isotropic chemical etchant etches the InGaAs contact layer at much faster rate than the active layers. It is therefore crucial to protect this layer during the wet etching. ICP etching of the InGaAs contact produces

vertical side walls, which cannot be effectively protected by a SiNx deposition. Therefore an extra wet etching step is added after ICP. The sample is dipped in a H_2SO_4:H_2O_2:H_2O 1:1:20 solution for 5 seconds to create an undercut on this layer. Following this wet etching, deposition of a 200 nm SiNx film in a PECVD chamber can fully cover the contact layer. As one can see in Figure 3.20, using this technique the InGaAs contact remains intact during fabrication.

3.4.3 QW etching (dry etching and wider contact mask)

For QW etching, the combination of dry etching and a wide contact mask can be used to get the desired structure for the laser. In Figure 3.21 the contact mask layout of this layer is depicted. The mask is wide on the DFB section and tapers down to the mesa tip width on the taper sections.
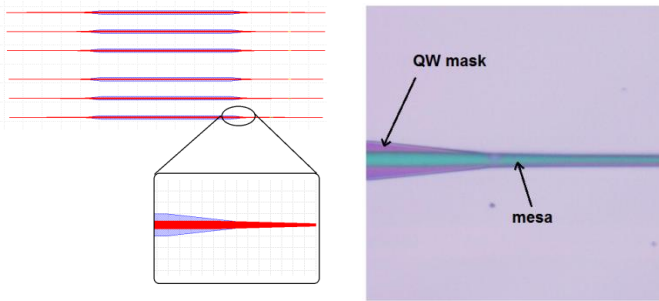
Figure 3.21: QW contact mask layout, the mask is 9 µm wide in the DFB part (a), and then tapers down to the tip of the taper (inset), microscopic image of the sample (b).

The thickness of the active region is around 300 nm in total and can be dry etched using ICP. The ICP recipe is based on a CH_4/H_2 chemistry. The ICP recipe is a standard process, optimized to reduce the roughness of the etched sidewalls with an accurate etch rate. The sample in etched in multiple cycles. Within each cycle 50 nm of the active region is removed. One should be careful not to over etch the sample, because the recipe can etch also the n-InP layer. This layer is quite a thin film and etching it would increase the device series resistance.

3.4.4 Cleaning of Al-containing QW

The second type of active materials that we have used was an InGaAlAs MQW stack. The issue encountered with this structure is that InGaAlAs materials are vulnerable to oxidation when exposed to air [15, 16]. This effect is difficult to avoid during fabrication. The oxidized regions may introduce nonradiative recombination centers and are an issue for reliability [17]. Oxidation can either happen on the top exposed surface of the active region (SCH layer) and on the

mesa side walls. On the top SCH layer an InGaAsP layer can be grown to protect the surface from oxidation. This was the case for one of our III-V wafers in which 25 nm of InGaAsP (PL at 1170 nm) is grown on the InGaAlAs active region.

Generally cleaning processes are required to remove the oxidized films, after which the surface needs to be covered with a protective layer immediately. In a regrown laser, the cleaning can be done in the Metalorganic Vapor Phase Epitaxy (MOVPE) chamber with cleaning gases after which a semi-insulating InP (Fe-InP) can be selectively grown to bury the mesa stripes [18].

In the wafer bonded devices the oxidized layers are wet etched. This is done in 2 steps by using H_2SO_4:H_2O_2:H_2O 1:1:20, followed by BHF. The first step is for etching the active region and the second step was for removal of the oxidized layer [19]. Following these steps, a 70 nm SiNx high frequency (HF) film is deposited at room temperature to protect the active region from oxidation.

3.4.5 Passivation with a thick SiNx layer

For the passivation of the III-V sample normally a thick layer of BCB is spin coated on the mesas. But the BCB layer adhesion to the mesa walls which are wet etched and have negative slope is poor. This leads to detachment of the BCB from the mesa wall, creating a gap between them. During the metallization of the pads the metal can penetrate through the gap and short circuit the laser. Therefore before BCB passivation, a thick 600 nm SiNx is deposited in a PECVD chamber (Figure 3.22). Before the p-contact metallization, these passivation layers need to be etched back to expose the top of the mesa. The dry etching of BCB in RIE is quite a fast process (400nm/min) but it is selective to the SiNx etching (8:1), so one can easily etch both layers and still preserve the planearity of the surface.
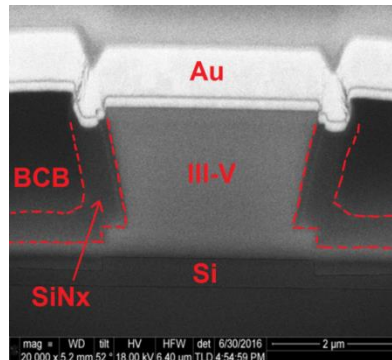

Figure 3.22: Thick SiNx layer passivates and protects the mesa side wall.

3.4.6 Taper isolation

For our heterogeneously integrated DFB laser on SOI, coupling light from the III-V waveguide to the Si waveguide is realized using inverted tapers. These tapers are long adiabatic tapers to realize high-efficiency optical coupling. In the standard laser geometry a single p-contact is used to pump the DFB lasers and the taper sections.

During dynamic measurement of these lasers we have observed a roll-off in the low frequency small signal response. Since this behavior has a cut off frequency of a few GHz, it is attributed to the modulation response of the tapers. In order to verify the theory, the tapers should be electrically isolated from the DFB laser. In this configuration (Figure 3.24) an RF signal can be applied to the DFB section, while a DC current is biasing the tapers.
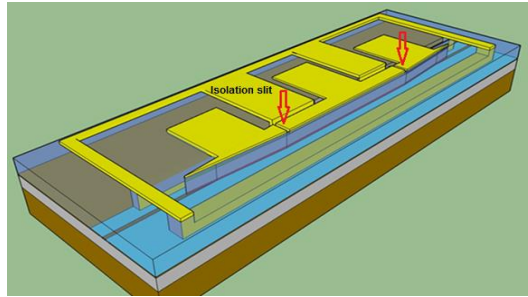
Figure 3.24: Schematic of the DFB laser with electrically isolated tapers.

In order to implement this, a few processing steps need to be modified. First of all, after the etch back of the BCB and SiNx layers and before the p-contact metallization, one lithography is performed to etch the InGaAs contact layer and into the p-InP cladding. The contact mask for this lithography is shown in Figure 3.25-a. Since the surface is planarized at this step, we could use a thin AZ5214 layer as a positive photoresist. Figure 3.25-b shows a microscope image of the sample after the lithography.
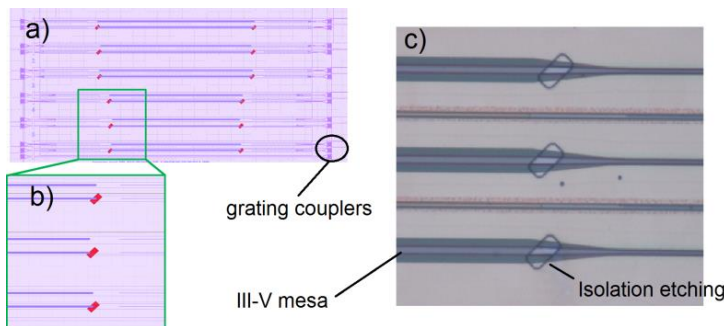
Figure 3.25: Mask layout for the isolation (a), zoom-in image (b), and microscope image of the device after the lithography (c).

Following the lithography, the sample is etched in the ICP, etching the top p-contact InGaAs layer and a bit of the p-InP film. 6 cycles were enough to etch the 200 nm InGaAs layer and 130 nm of the InP layer. The next step is the p-contact layer metallization as stated before in this chapter (Figure 3.26-a). The 45 degree angle of the isolating trench with respect to the waveguides is to reduce the back reflection to the DFB cavity (Figure 3.26-b). A cross section of the structure is shown in Figure 3.26-c. The zoom-in figure shows that the InGaAs layer is completely etched (Figure 3.26-d).
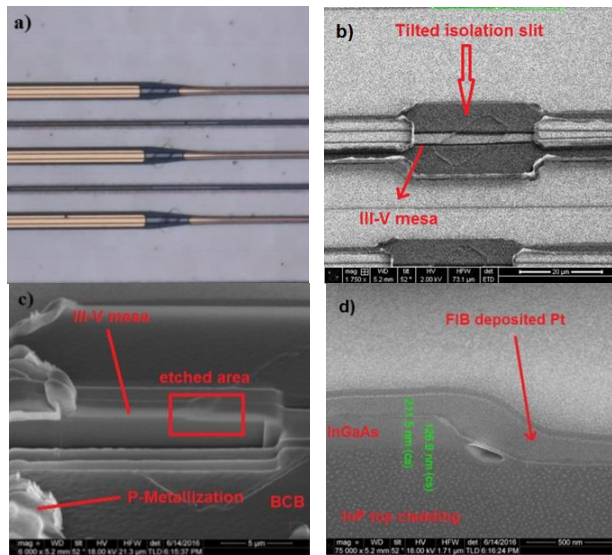
Figure 3.26: Microscope image of the sample after the P-contact metallization (a), SEM image of the isolation area (b), and the 45° angled cross section at this position (c), the cross section in the red rectangle area (d).

3.4.7 Slit etching for external cavity definition

In chapter 2 it is discussed that an external feedback mechanism in the DFB laser can be implemented to extend the modulation bandwidth. In this section the method that we used to create such a feedback reflector is discussed. After fabrication of the laser, a slit position on the sample is defined. The etching was realized by a Focused Ion Beam (FIB) system. Since there are two thick passivation layers on top of the Si waveguide, first a few test runs were performed on a sample with similar structure. The Ga-ion acceleration voltage and the current were optimized to reach to the waveguide and etch through it, see Figure 3.27-a. From left to right the etching time is increasing to realize the desired depth. The rightmost slit on Figure 3.27-b was selected to be on target in terms of depth for fabricating the reflector on the real samples.
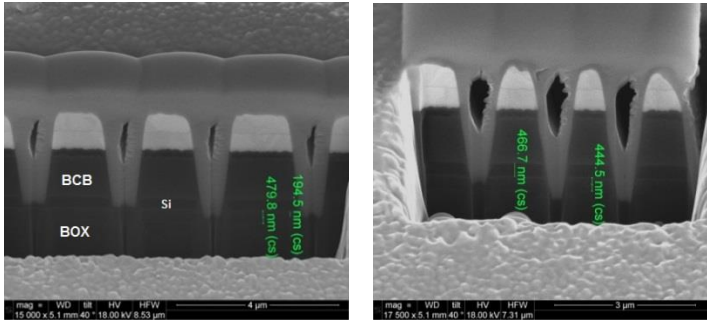
Figure 3.27: SEM images from the test sample for FIB definition of the slits. The etch time is increasing from left to right (a, b) to fulfil the desire depth.

As can be seen in the figure the etching is not vertical, which leads to less back reflection. But after testing different devices we concluded that this method is an effective way to achieve an extension in modulation bandwidth due to the photon-photon resonance, as will be discussed in the next chapter.

3.5 Epitaxial layer structures used during this PhD

3.5.1 InGaAsP

The InGaAsP epitaxial stack used for processing DFB lasers is presented in Table 3.2. This stack consists of a 180 nm thick n-InP contact layer, two 100 nm thick InGaAsP separate confinement heterostructure layers (bandgap wavelength 1.17 μm), six InGaAsP quantum wells (6 nm thick, emission wavelength 1.55 μm) surrounded by InGaAsP barriers, a 1.5 μm thick p-InP top cladding, and a 300 nm p-InGaAs contact layer. On both sides of the structure two sacrificial layers (InP/InGaAs) are grown with a 100 nm thickness. PL measurements were performed on the bonded sample (after removing the InGaAs contact layer (Figure 3.28)), showing a PL peak around 1540 nm.

Table 3.2: Description of the epitaxial InGaAsP stack used for the fabrication of DFB lasers

Layer nb	Layer type	nb of period	material	PL wavelenth	thickness (nm)	Carrier conc.	Type
17	Sacrificial		InP		100		nid
16	Sacrificial		InGaAs		100		nid
15	Caldding n		InP		10	1.0e18	n
14	superlattice	2	InP		7.5	1.0e18	n
13	Superlattice	2	InGaAsP	1.17	7.5	1.0e18	n
12	Cladding n		InP		180	1.0e18	n
11	SCH		InGaAsP	1.17	100		nid
10	MQW-w	6	InGaAsP	1.55	8		nid
9	MQW-b	5	InGaAsP	1.17	10		nid
8	SCH		InGaAsP	1.17	100		nid
7	Cladding p		InP		500	5.0e17	p
6	Cladding p		InP		1000	5.0e18	p
5	Transition		InGaAsP	1.17	20	1.0e19	p
4	Contact p		InGaAs		300	3.0e19	p
3	Sacrificial		InP		100		nid
2	Stop-etch		InGaAs		100		nid
1	Substrate		InP				N
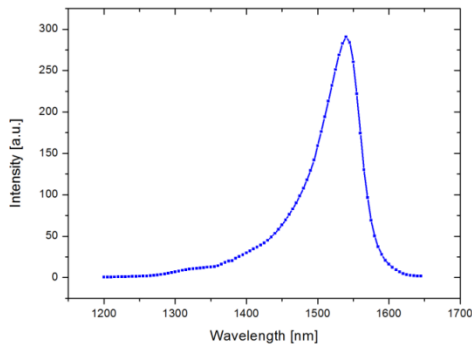
Figure 3.28: Photoluminescence spectrum of the InGaAsP active region after bonding.

3.5.2 InGaAlAs

The second epitaxial structure used in this project has an Al-containing active region. The structure is shown in table 3.3. Eight InGaAlAs quantum wells (8 nm thick, emission wavelength 1.55 μm) are surrounded by InGaAlAs barriers (10 nm thick) with a bandgap wavelength of 1.10 μm. For this structure the top SCH consists of an InGaAlAs layer (25 nm thick) and an InGaAsP layer (25 nm thick). In this configuration the InGaAsP cladding layer protects the active layers from surface oxidation during fabrication. The bottom SCH layer is a 50 nm thick InGaAlAs. For this wafer also two InP/InGaAs sacrificial layers are grown on both sides.

Table 3.3: Description of the epitaxial InGaAlAs stack used for the fabrication of DFB lasers

Layer nb	Layer type	nb of period	material	PL wavelenth	thickness (nm)	Carrier conc.	Type
17	Sacrificial		InP		100		nid
16	Sacrificial		InGaAs		100		nid
15	Cladding n		InP		10	1.5e18	n
14	Superlattice	2	InP		7.5	1.5e18	n
13	Superlattice	2	InGaAsP	1.17	7.5	1.5e18	n
12	Cladding n		InP		200	1.5e18	n
11	SCH		AlGaInAs	1.1	50	0 > 1.5e18	n
	MQW-b		InGaAsAl	1.1	10		
10	MQW-w	8	InGaAsAl	1.55	8		nid
9	MQW-b	8	InGaAsAl	1.1	10		nid
8	SCH		AlGaInAs	1.1	25		
7	SCH		InGaAsP	1.17	25		nid
6	Cladding p		InP		2000	1.0e18 >1.5e18	p
5	Transition		InGaAsP	1.17	20	6.0e18	p
4	Contact p		InGaAs		200	2.0e19	p
3	Sacrificial		InP		300		nid
2	Stop-etch		InGaAs		300		nid
1	Substrate		InP				N

PL measurements were performed on the bonded sample (after removing the InGaAs contact layer (Figure 3.29)), showing a PL peak around 1520 nm.
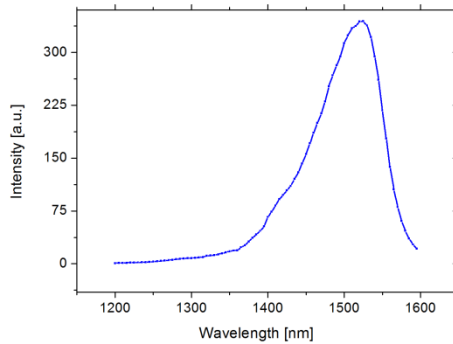
Figure 3.29: Photoluminescence spectrum of the InGaAlAs layers after bonding.

3.6   Conclusion

This chapter discussed the design and fabrication of the heterogeneously integrated DFB laser on the silicon waveguide circuit. The optical design for high speed performance was investigated. Various techniques to improve the laser diode fabrication which have been developed during this project were presented. Some of these methods are general solutions and can be applied to any heterogeneously integrated III-V-on-silicon devices, but others were specifically developed for high speed DFB lasers. For example, taper isolation and slit etching are optimized to enhance the dynamic properties of the directly modulated DFB lasers. At the end, the two epitaxial layers structures which have been used during this PhD are discussed together with their PL spectra.

References

[1]   Fimmwave, Photon Design, http://www.photond.com.

[2]   S. Keyvaninia, S. Verstuyft, L. Van Landschoot, F. Lelarge, G.-H. Duan, S. Messaoudene, J. M. Fedeli, T. De Vries, B. Smalbrugge, E. J. Geluk, J. Bolk, M. Smit, G. Morthier, D. Van Thourhout, and G. Roelkens, "Heterogeneously integrated III-V/silicon distributed feedback lasers", Optics Letter. vol. 38, pp.5434-5437 (2013).

[3]   G. Roelkens, D. Van Thourhout, and R. Baets, "Ultra-thin benzocyclobutene bonding of III-V dies onto SOI substrate", Electronics Letter, vol. 41(9), pp. 561–562 (2005).

[4]   G. Roelkens, J. Van Campenhout, J. Brouckaert, D. Van Thourhout, R. Baets, P. Rojo Romeo, P. Regreny, A. Kazmierczak, C. Seassal, X. Letartre, G. Hollinger, J.M. Fedeli, L. Di Cioccio, C. Lagahe-Blanchard, "III-V/Si photonics by die-to-wafer bonding", Materials Today, vol. 10(7), (2007).

[5]   D. Liang, G. Roelkens, R. Baets and J.E. Bowers, "Hybrid integrated platforms for silicon photonics", Materials, vol.3(3), pp.1782-1802, (2010).

[6]   F. Niklaus, P. Enoksson, E. Kalvesten, and G. Stemme, "Low-temperature full wafer adhesive bonding", Journal of Micromech. Microeng, vol. 11(2), pp.100–107 (2001).

[7]   D.-H. Choi, C.-H. Yeo, J.-T. Kim, C.-W. Ok, J.-S. Kim, Y. Kwon, and Y.-H. Im, "Study on bisbenzocyclobutene bonding for the development of a si-based miniaturized reformer of fuel cell systems", Journal of Micromech Microeng,vol.19(7), (2009).

[8]   D. D. L. Chung, "Materials for thermal conduction", Applied thermal engineering, vol. 21(16), pp. 1593-1605, (2001).

[9]   C. L. Yaws. Handbook of Thermal Conductivity. 3:1–398, (1995).

[10] T. P. Pearsall. "Properties, processing and applications of Indium Phosphide". IEEE Inspection, vol. 21, (2000).

[11] Dow Company. Processing Procedures for CYCLOTENE Series Dry Etch Resins.

[12] S. Keyvaninia, et al. "Ultra-thin DVS-BCB adhesive bonding of III-V wafers, dies and multiple dies to a patterned silicon-on-insulator substrate", Optical Materials Express, vol 3(1), pp. 35-46, (2013).

[13] K. Nakahara, T. Tsuchiya, T. Kitatani, K. Shinoda, T. Taniguchi, T. Kikawa, M. Aoki, and M. Mukaikubo, "40- Gb/s direct modulation with high extinction ratio operation of 1.3-µm InGaAlAs multiquantum well ridge waveguide distributed feedback lasers," IEEE Photonics Technology Letter, vol. 19(19), pp.1436–1438, (2007).

[14] C. Zhang, S. Srinivasan, Y. Tang, M.J. Heck, M.L, Davenport, J.E. Bowers,"Low threshold and high speed short cavity distributed feedback hybrid silicon lasers", Optics express, vol. 22(9). pp. 10202-10209, (2014).

[15] J. Decobert, N. Lagay, C. Cuisin, B. Dagens, B. Thedrez, and F. Laruelle, "MOVPE growth of AlGaInAs-InP highly tensile-strained MQWs for 1.3 µm low-threshold lasers," Journal of Crystal Growth, vol. 272(1-4), pp. 543–548, (2004).

[16] T. Nakamura, T. Okuda, R. Kobayashi, Y. Muroya, K. Tsuruoka, Y. Ohsawa, T. Tsukuda, and S. Ishikawa, "1.3-µm AlGaInAs strain compensated MQW-buried-heterostructure lasers for uncooled 10-Gb/s operation", IEEE Journal of Selected Topics in Quantum Electronics, vol. 11(1), pp. 141–148, (2005).

[17] Y. Takino, , M. Shirao,N. Sato,T. Sato, T. Amemiya,N. Nishiyama, and S. Arai,"Improved regrowth interface of AlGaInAs/InP-buried-heterostructure lasers by in-situ thermal cleaning", IEEE Journal of Quantum Electronics, vol. 48(8), pp.971-979. (2012).

[18] H. Sato, T. Tsuchiya, T. Kitatani,A. Taike, H. Uchiyama, and M. Aoki, "In-situ cleaning for highly reliable 1.3-µm InGaAlAs buried heterostructure laser", OFC(2004).

[19] R. Gessner, A. Dobbinson, A. Miller, J. Rieger,and E. Veuhoff"Fabrication of AlGaInAs and GaInAsP buried heterostructure lasers by in situ etching", Journal of crystal growth, vol.248, pp. 426-430, (2003).

4

High-speed characterization of III-V-on-Silicon DFB lasers

We already discussed the epitaxial layer structure of the III-V material that we have used to realize fast DFB lasers. In this chapter, first static measurement results together with small signal results will be presented for each of the III-V layer stacks. Then large signal measurement results will follow. Various techniques that have been discussed in the previous chapters will be studied experimentally in this chapter. For each modulation method, experimental setups will be introduced. Eye diagrams and bit error rate (BER) curves are important qualitative and quantitative characteristics of a communication link, respectively. These features will be presented for the links in a back-to-back configuration and after transmission over an optical fiber. Finally in the last section of this chapter a brief discussion and conclusion will be provided.

4.1 Static and small-signal characterization
4.1.1 6 QWs InGaAsP sample

The first batch of lasers was fabricated using InGaAsP quaternary materials in the active region. The active region consists of 6 QWs and the PL peak is at 1540 nm. More details about the epitaxial layer structure were given in chapter 3 (Table 3.2). The static characteristics of the lasers were measured using a Keithley 2400 low noise current source and a HP power meter. In Figure 4.1, the top view of the device is shown. The light from the DFB lasers was coupled from the Si waveguide to a single mode fiber by a grating coupler with a 7 dB fiber-to-chip coupling loss. The laser length is 340 μm and two 220 μm long

tapers are coupling light to the Si waveguide. The first order DFB grating period is 245 nm and the duty cycle is 50%. These lasers have asymmetric λ/4 phase shift meaning that the phase shift is located in a way that the ratio of the grating length on the right hand side over the grating length on the left hand side is 1 to 9. The primary idea for this design was to check the mode stability in the asymmetric configuration. We have also designed symmetric first order DFB lasers with the same period and duty cycle. These lasers had longer lengths (600 μm and 700 μm) compared with the asymmetric ones. However, they did not show a stable single mode behavior which can be related to their κL ≈ 9 product which is almost double that of the asymmetric ones (κL ≈ 4)

The measurements were done on a temperature-controlled stage at 20°C.
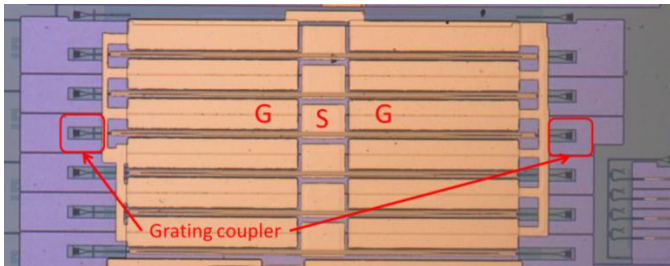
Figure 4.1: Top view of the fabricated DFB lasers.

The optical spectrum and the L-I-V curve of a typical laser are depicted in Figure 4.2. The side mode suppression ratio (SMSR) is more than 45 dB. Since this laser is a strongly asymmetric phase shifted DFB laser, depending on the round trip phase, one of the band edge modes is lasing depending on which one has the lowest threshold gain. The threshold current (I_{th}) is 17 mA and a waveguide-coupled optical output power of 6 mW is obtained at a drive current of 100 mA. The kink in the L-I curve is attributed to a mode hop from the shorter wavelength band edge mode of the DFB laser to the longer wavelength mode due to the device heating (an effect which only occurs in CW operation and not under dynamic operation). The extracted coupling coefficient from the stop-band of the laser spectrum in the low gain approximation is about 135 cm^{-1}. This corresponds with a DVS-BCB bonding layer thickness of 50 nm. It is worth to mention that yield of the fabrication was high and all lasers with the same period and length are working almost identical. But the lasers with longer length (600 μm) were multimode at the low current ($\approx 2I_{th}$) which is related to their high κL value.

The limited wall plug efficiency of the device (6%) is attributed to scattering losses in and incomplete pumping of the taper sections. Note that the current plotted in Figure 4.2-b represents the current injected in both the DFB laser and the taper structures and that the output power is the single facet output power of the symmetrical DFB laser. The series resistance of the device is 10 Ω. The laser operates at 1566 nm, which is close to the gain peak of the laser structure.
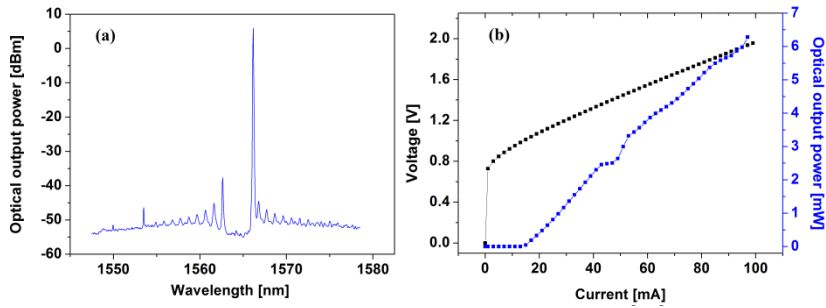
Figure 4.2: The DFB spectrum (a), LIV curve of the device (b) The optical output power is the waveguide-coupled single facet output power.

After these measurements, the sample's dynamic characterization has been done to find the small signal modulation bandwidth. The schematic of the experimental setup and the photograph of a device under measurement are shown in Figure 4.3.
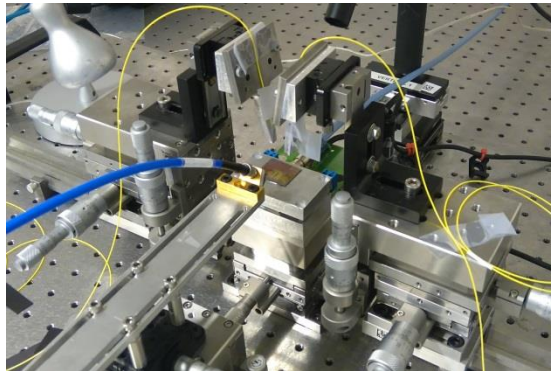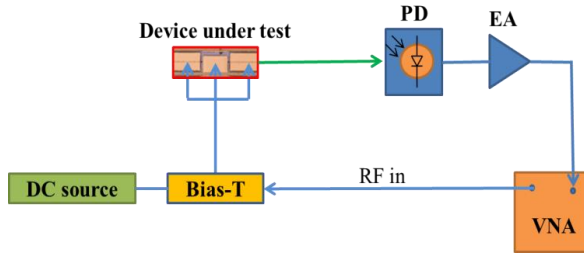

Figure 4.3: Schematic of the setup for a small signal measurement (top), a photograph of the actual setup with a GSG and vertical fiber coupling stages (bottom).

The small signal characterization was measured using a Keysight PNA-X 67 GHz network analyzer. The signal from the network analyzer is combined with a DC current in a Bias-T and applied to the laser via a GSG high speed probe. The modulated light from the laser is converted to an electrical signal by a 40

GHz pin photodiode. This signal is used by the PNA to measure the response of the laser.

As described in chapter 2, the relaxation oscillation frequency depends on the bias current of the laser. To illustrate this fact, in Figure 4.4, the modulation response of the laser is shown versus frequency for different bias currents. One can see that the relaxation oscillation resonance moves towards higher frequencies as the bias current increases (eq 2.19).

It is interesting to notice the modulation of the low frequency response of the DFB laser in Figure 4.4, 4.5. This effect can be related to the modulation of the taper section, which acts as an SOA, or to spatial hole burning. As has been discussed in chapter 2, both of these phenomena have a cut-off frequency determined by the differential carrier lifetime.
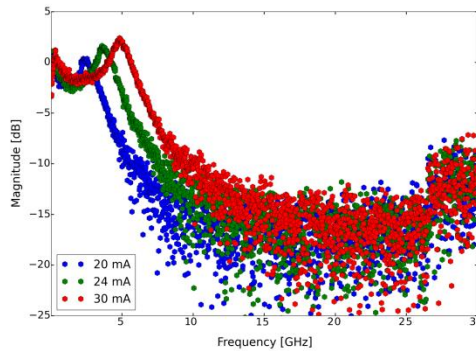
Figure 4.4: Small signal response of a DFB laser and its relaxation oscillation frequency shifting vs the bias current.

The highest measured modulation bandwidth was 15 GHz (Figure 4.5). The higher modulation bandwidth of this laser in comparison with other demonstrated hybrid lasers is attributed to the small laser mode volume and high confinement factor in the active region. As we discussed in the previous section, the relaxation oscillation frequency has a square root dependency on the optical confinement factor in the quantum wells regions. Our simulation with FIMMWAVE software shows that the confinement factor per quantum well is about 1.75% for this design. As we said before in chapter 3, for the InP based lasers (not heterogeneously integrated with the high contrast SOI platform) the confinement factor per quantum well is almost the same. These lasers mostly are based on buried heterostructures (lasers are covered by a low contrast InP material) which makes it difficult to control the confinement factor of the light in the active. However there are advanced structures like a ridge waveguide lasers where the laser is surrounded with a BCB or SiO_2 layer in order to increase the contrast.
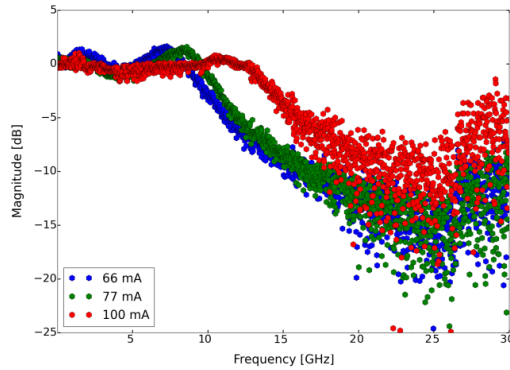
Figure 4.5: Small signal response of a DFB laser at the higher bias currents.

## 4.1.2 6 QWs InGaAsP sample with photon-photon resonance

From a theoretical point, we have seen that external feedback to the laser cavity can be exploited to enhance the modulation bandwidth [1, 2]. To verify this technique experimentally a feedback mirror is needed to reflect part of the laser output power back into the laser cavity. The 3D schematic picture of the laser structure with reflective mirror is depicted in Figure 4.6. To obtain such reflection after fabrication of the laser without any feedback mirror, a slit with 5 µm width has been etched by focused ion beam (FIB) all the way down through the passivation layers of BCB and SiNx and also through the Si waveguide until the buried SiO_2 was reached. A few test facets have been etched in advance with different ion energies and currents on dummy samples to make sure to create a flat and smooth etched facet (see section 3.4.6). The slit is 1.5 mm away from the DFB laser's closet facet.
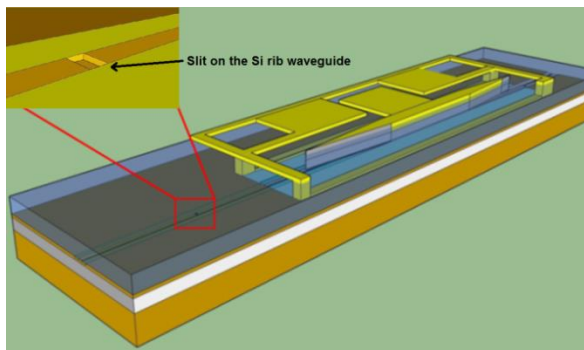
Figure 4.6: Schematic drawing of the laser with a feedback mirror.

The laser length is 400 μm and two 150 μm long tapers are coupling light to the Si waveguide. The first order DFB grating period is 245 nm and the duty cycle is 50%. These lasers have a λ/4 phase shift in the middle of the laser.

In Figure 4.7, the small signal modulation response of the laser before and after making the slit is depicted. It is obvious that the feedback mirror results in the creation of photon-photon resonance peaks. After the slit creation, at high bias currents, the CPR peak is suppressed. By increasing the bias current, the CPR peak is moving toward higher frequencies and starts to approach half the PPR frequency (18/2= 9 GHz). Around this frequency, the external reflection field is out of phase with the field inside the cavity. This destructive interference causes a decrease in the modulation response.
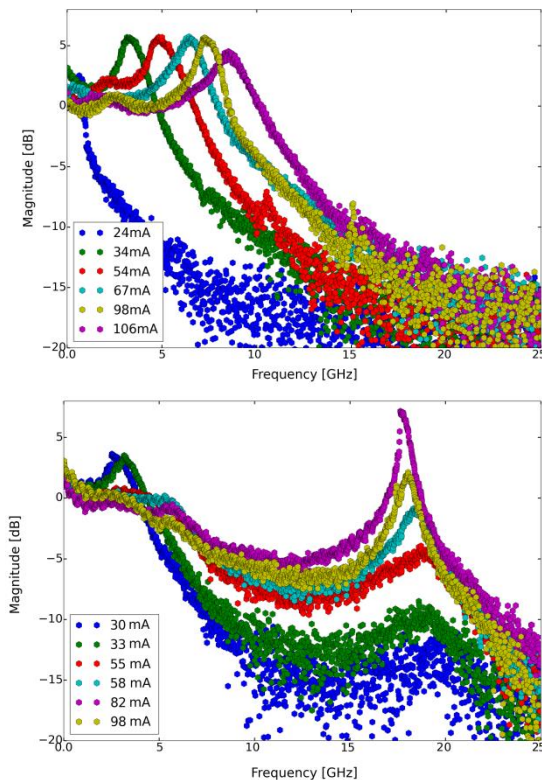
Figure 4.7: Small signal response before (top) and after (bottom) making the reflector facet.

The reflected light intensity depends on the reflectivity of the mirror and the losses in the external cavity. Between the cavity and the slit, there is a taper section which also is biased together with the laser cavity. While the photon-photon resonance in this design did not allow us to extend the modulation bandwidth it provided a way to relate the position of the PPR peak to the length of the external cavity. The important parameter is the roundtrip time in the external cavity, which depends on the length and the group index of the cavity:

$$f = c/(2n_g L) \qquad\qquad\qquad\qquad (4.1)$$

where c is the speed of light in vacuum, n_g is the group index of the waveguide and L is the cavity length (the distance between the DFB laser and the slit). The DFB laser has a finite penetration depth for the reflected light; therefore the reduced length should be considered and not the real laser length.

4.1.3 8 QWs InGaAlAs sample

The heterogeneously integrated DFB lasers that are fabricated on SOI have a thermal dissipation problem [3-5]. Since our approach for the integration of active III-V materials is adhesive bonding with a thin BCB-DVS layer, also this layer has a low thermal conductivity and acts as a thermal isolator hindering the heat dissipation from the active area. The heating deteriorates the laser performance in terms of threshold current, output power and speed. This is related to the thermionic emission of hot electrons to escape from the QWs conduction band. This can be overcome by introducing III-V materials with high conduction band offset [6, 7].

    This was one of the reasons to explore Al-containing materials in the active region. Another reason is a high differential gain of these materials compared with InGaAsP materials [8-10]. Because of a large conduction band offset, the escape rate of electrons is much lower for InGaAlAs QWs than for InGaAsP QWs. On the other hand, the valence band offset for InGaAlAs QWs is lower than for InGaAsP QWs. Therefore, the hole transport time will not be a limiting factor either.

    The first epitaxial layer structure that was used for this purpose was an InGaAlAs stack from III-V Lab with 8 QWs (Table 3.3). We already discussed the influence of the oxidation of the Al active layers on the laser performance; therefore we were interested to explore this effect experimentally. Two different fabrication processing sequences were followed in which for the first chip the cleaning process (see section 3.3) and a wider QW mask were used (sample A), while for the other sample, the active region was etched through by ICP using the laser's mesa as a mask and no cleaning processes were applied (sample B).

    Static characterization was done on both samples. Since the SOI and the epitaxy stack were identical for both samples, it is fair to compare the two different fabrication techniques. We did the comparison for all the lasers in both samples. For identical lasers, the lasing wavelengths are very similar (Figure 4.8). This means that the effective index of the hybrid waveguide mode of the laser is not changed substantially by widening the active region. This is related to the fact that the optical guided mode is well confined in the active region and increasing the width of the active region will not alter the effective index value.
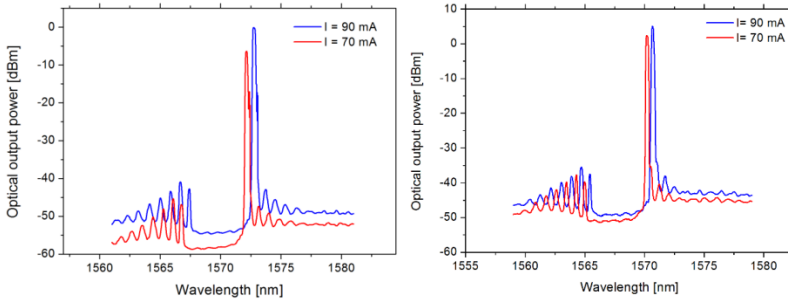
Figure 4.8: optical spectra of the DFB laser from sample A (a), from sample B (b).

We measured the series resistance for lasers on both samples. The fabricated laser cross-sections are shown in Figure 4.9. These cross-sections were done on both the taper and the DFB laser part. As described in the fabrication chapter, our QW mask was wider on the laser body and tapered down on the taper sections. Figure 4.9-a indicates a 350 nm under-cut for the sample A due to wet etching. As one can see in Table 4.1, the series resistance for the sample A (cleaning process was applied and a wide QWs mask was used) is higher than for the sample B. The under-cut is combined with a slight misalignment of the QW mask assumed to be the main reason for the increase of the series resistance.
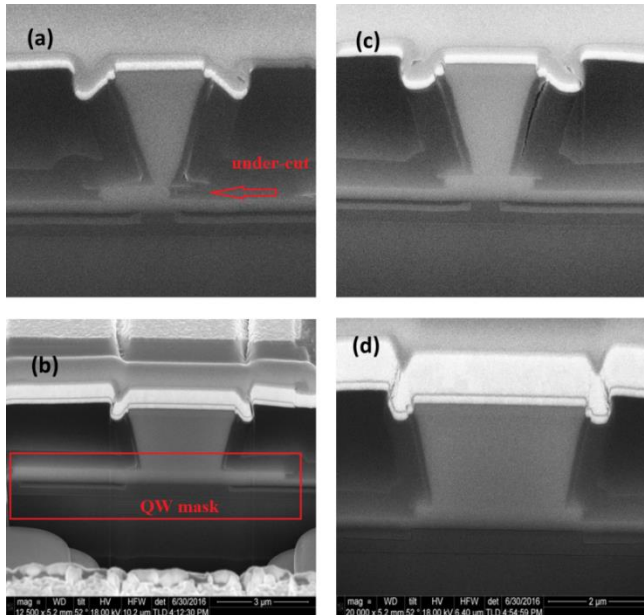
Figure 4.9: Cross-section of the DFB laser from sample A on the taper section (a), on the DFB section (b) and for the laser from sample B on the taper section (c) and the DFB section (d).

Table 4.1: Performance comparison of two samples with two different fabrication methods.

	Lasing wavelength	Series resistance	Output power	Stop-band width	I_{th}
Sample A	1572 nm	10 ohm	1 mW	5.5 nm	18 mA
Sample B	1571 nm	6 ohm	5 mW	5.5 nm	35 mA

This damage to the tapers affected the laser output power. The misalignment of the mesa with respect to the silicon waveguides layer is almost the same for both samples (70 nm), but an imperfect taper causes an inefficient coupling to the Si waveguide. On the other hand, the bonding thickness is the same for both samples (10 nm) (Figure 4.10).
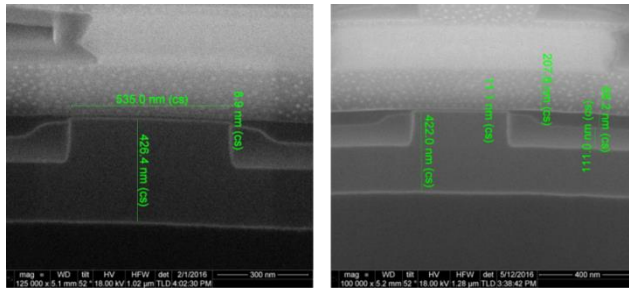
Figure 4.10: zoom in on the bonding interface of sample A (a) and sample B (b).

A thinner bonding layer results in a higher coupling coefficient, better thermal properties. The estimated coupling coefficient from the stop band is 200 cm^{-1}. A higher coupling coefficient results in a lower threshold current. This helps lasers to have a higher relaxation oscillation frequency at a lower bias current. The average threshold current for the sample A lasers with a 340 μm length is 18 mA at 20 ℃, but this value is 36 mA for the sample B (Figure 4.11). Above threshold the output power varies nonlinearly with current because of the thermal shift of wavelength with respect to the gain peak spectrum and sometimes mode hopping.
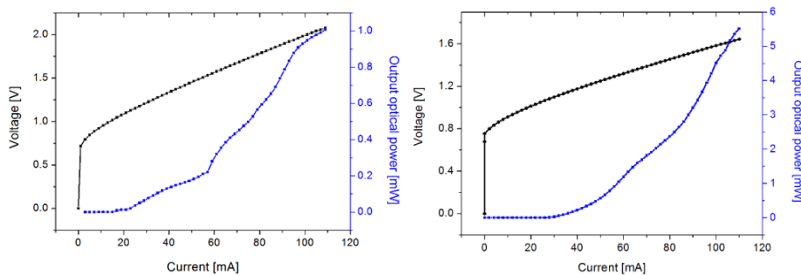

Figure 4.11: LIV curves for the DFB laser from sample A (a), from sample B (b).

This shows the importance of a wide active layer and cleaning process. It has been shown that the oxidation of the Al-containing active region can trap the carriers in defect energy levels and through carrier non-radiative recombination increases the temperature of the active region [11, 12]. This two-fold effect deteriorates the lasers' threshold current for sample B.

Small signal measurements have been done to know the modulation bandwidth. For the short stable lasers on both samples we have observed a photon-photon resonance. A large modulation bandwidth is achieved because of an external cavity, caused by the fiber-chip grating couplers assumed to reflect 4% and with 1000 µm length which correspond to a resonance peak between 25-30 GHz. One can see in Figure 4.12, for both lasers from different samples, photon-photon resonances occur around 26 GHz.
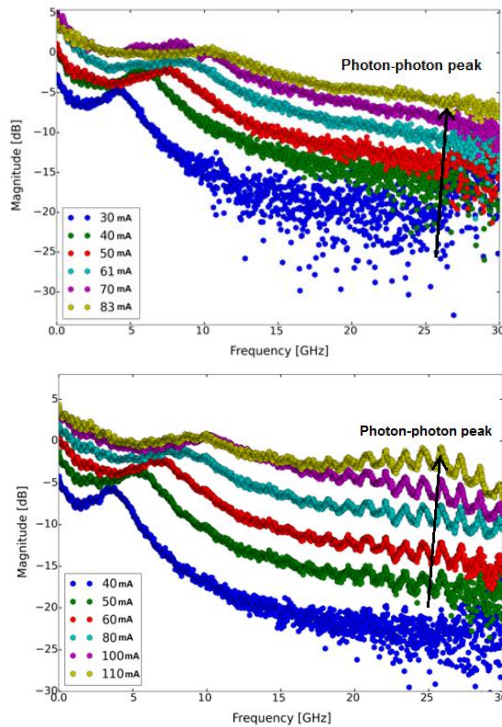
Figure 4.12: Small signal response of the DFB laser from sample A (top), sample B (bottom).

In sample A, the damage to the tapers reduces the amount of reflection, so that the photon-photon resonance peak is not strong enough to appear above the -3 dB level, but for sample B, the modulation bandwidth was 27 GHz due to the PPR. Based on our calculation for the previous experiment with the slit, these peaks positions correspond to a Fabry-Perot cavity between the two grating

couplers. To verify that reflections from the fibres' facets are not responsible for the PPR effect, the distance of the fibres from the grating couplers was changed during the measurement. We did not observe any influence in the photon-photon resonance peak position and strength.

4.2   NRZ direct modulation

4.2.1 6 QWs InGaAsP samples

The next step of the characterization procedure is a large signal measurement. In Figure 4.13, a schematic representation of the setup is shown. To generate pulses at high bit rates a SHF 12100B pulse pattern generator (PPG) was used with adjustable pattern length. The output of the PPG was amplified by a SHF S807 broadband RF amplifier. An RF-voltage of 2 Vpp (assuming a 50 Ω load) was applied to the laser to realize its large signal modulation. As the laser is not 50 Ω terminated, a much lower voltage swing (<1 V) is seen by the laser. Eye diagrams were measured using a Tektronix DSA 8300 sampling oscilloscope. Eye diagrams as a function of modulation rate, measured using a 40 GHz pin photodiode with external TIA, are shown in Figure 4.14 for the back-to-back case.
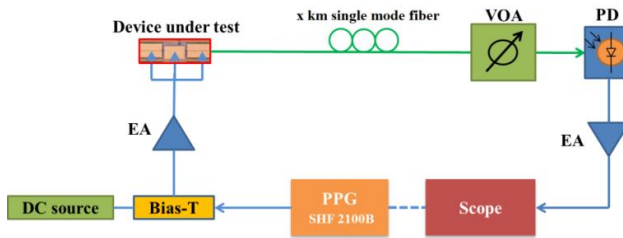
**Figure 4.13:** Schematic of the setup for a large signal measurement.
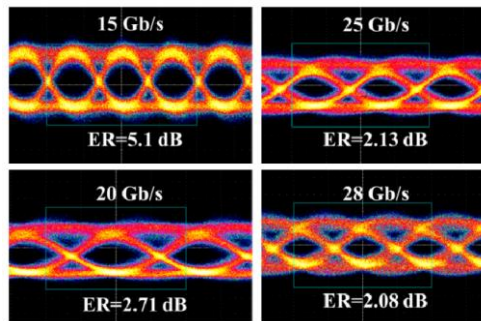
Figure 4.14: Eye diagrams for back-to-back operation at 15, 20, 25 and 28 Gb/s using a 2^7-1 pattern length (bias current of 100 mA at 20 ℃).

At 20 and 25 Gb/s modulation speed, the bit error rate (BER) measurements were done for both back-to-back and using 1 km standard single mode fiber

(SSMF) using a 2^7-1 NRZ PRBS pattern. The results are presented in Figure 4.15.
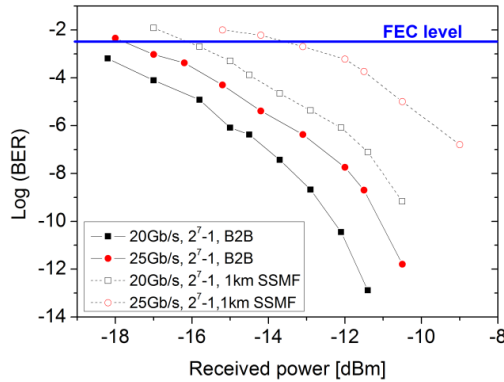

Figure 4.15: BER measurements for back-to-back and 1 km single mode fiber configurations using a 2^7-1 NRZ-PRBS pattern (bias current of 100 mA at 20℃).

As shown in Figure 4.15 assuming 7% hard-decision (HD) forward error correction (FEC), 2.4 dB and 4.0 dB power penalties were measured, for 20Gb/s and 25Gb/s transmission over 1 km SSMF respectively. At a bit error rate of 10^{-9}, a power penalty of 2 dB is obtained at 20 Gb/s. Back-to-back measurements and transmission measurements using a 2 km non zero dispersion shifted single mode fiber (NZ_DSSMF) were carried out at 28 Gb/s at a bias current of 100 mA at 20℃. This type of the single mode fiber has a lower dispersion in C-band. The dispersion was about 4.5-6 ps/nm.km at 1565 nm. A Sumitomo photodiode with a packaged limiting transimpedance amplifier was used at the receiver side. The eye diagrams of the back-to-back configuration and after the 2 km NZ_DSSMF fiber are shown in Figure 4.16. There was an internal DC blocker inside the oscilloscope for this measurement, so we could not measure ER for these eyes. Transmission over the 2 km NZ_DSSMF has a small impact on the eye opening. BER measurements were realized to verify the data transmission quality at 28 Gb/s for different PRBS pattern lengths (see Figure 4.17). Less than 1 dB power penalty at a BER of 10^{-9} was measured using the 2 km NZ_DSSMF at 28 Gb/s with a data stream length of 2^7- 1.
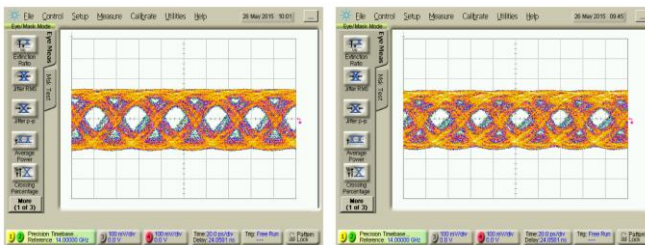
Figure 4.16: Eye diagrams for back-to-back (left) and after 2 km NZ_DSSMF fiber transmission (right) at 28 Gb/s using a 2^{11}-1 data pattern length (bias current of 100 mA at 20℃).
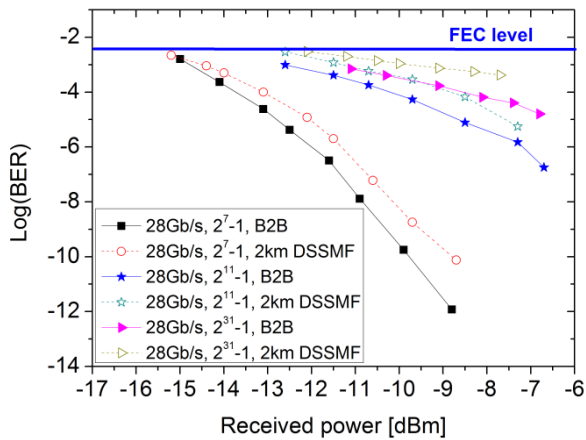
Figure 4.17: 28 Gb/s BER measurements for back-to-back and 2 km NZ_DSSMF configurations (the bias current is 100 mA).

Degradation can be observed for longer word lengths. This is related to the low frequency roll-off of the small signal response of the laser (see section 2.2.1) Using encoding methods such as 8b/10b may be useful to reduce this pattern effect [13].

4.2.2 8 QWs InGaAlAs sample

The large signal bit rate on the InGaAsP sample discussed above was limited to 28 Gb/s. In order to go beyond this limit, we measured the large signal response of the sample B, which had a higher modulation bandwidth (Figure 4.12). Normally with this bandwidth, one should be able to do 50 Gb/s, but at the time of this measurement, we had access only to an Alnair 400C PPG with a limited speed. This PPG can generate discrete bit rates of 20 Gb/s and 40 Gb/s and PRBS signals with pattern lengths of 2^7-1 and 2^{31}-1. A Keysight DSA_Z63 GHz real time oscilloscope has been used to capture the eye diagrams. The experimental setup was the same as the previous setup. In Figure 4.18, an electrical back-to-back signal at 40 Gb/s is shown.
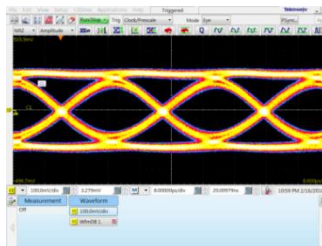

Figure 4.18: Back-to-back electrical eye diagram from the Alnair PPG at 40 Gb/s.

Optical eye diagrams at 40 Gb/s are depicted in Figure 4.19. In the case of a short PRBS pattern length of 2^7-1, for back-to-back (Figure 4.19-a) and after transmission over a 2 km NZ_DSSMF (Figure 4.19-b), eyes are open, but there are thick "1" and "0" levels. This can be explained by the fact that the small signal response of this laser is not flat, implying that the laser response depends on the length of the PRBS sequence. Therefore, the combination of these different amplitudes results in multiple transitions and thick levels. This becomes worse when a long PRBS pattern was used (Figure 4.19-c,d). The eyes become narrow and it is difficult to find a position in the middle of the eyes to do sampling for a BER measurement.
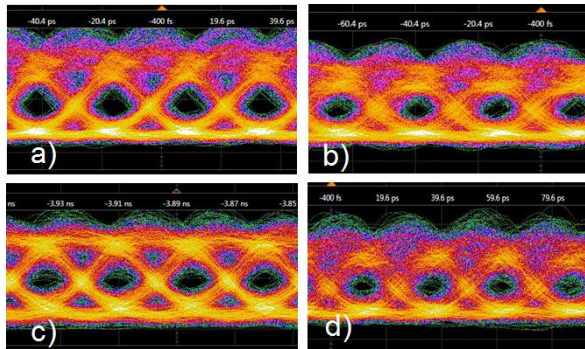
Figure 4.19: Eye diagram at 40 Gb/s, for a PRBS length of 2^7-1 for back-to-back (a) and after 2 km fiber (b), and the same for a length of 2^{31}-1 (c,d).

The BER measurement was done also with an Alnair 400C error detector set. Figure 4.20 shows the results of this measurement.
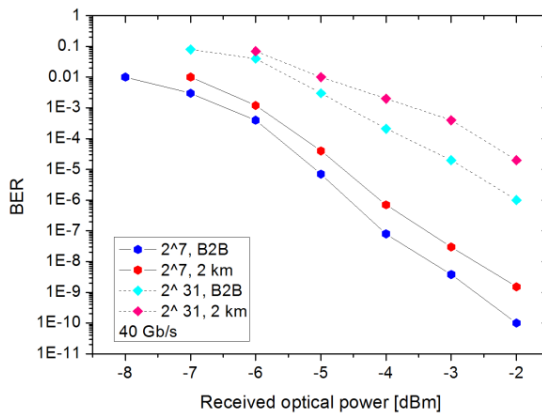

Figure 4.20: BER vs received optical power at 40 Gb/s.

Using a PRBS pattern length of 2^7-1, we achieved a BER of 1e-9 for a transmission over 2 km NZ_DSSMF. For a pattern length of 2^{31}-1, there are patterning effects due to the earlier mentioned low frequency roll-off in the small-signal response.

4.3   Pulse amplitude modulation (PAM-4)

The schematic in Figure 4.21, shows the standard experimental setup for PAM-4 direct modulation of a III-V-on-silicon DFB laser.
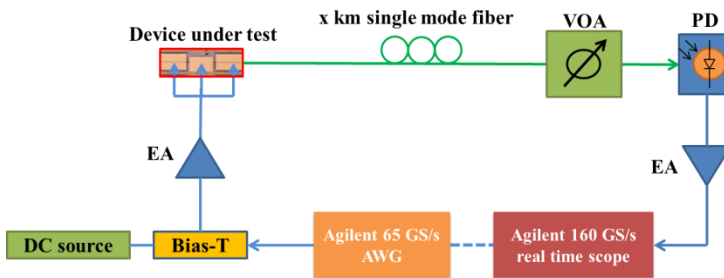

Figure 4.21: Schematic of the setup for a PAM-4 direct modulation experiment.

The electrical signal is generated by a Keysight M8195A arbitrary waveform generator (AWG) and is then amplified by an SHF-S708 RF amplifier. A low noise DC current is combined with the generated PAM-4 signal and was fed to the DFB laser through a bias-tee. The output of the bias-tee is used to drive the laser through a GSG RF probe. The DFB has approximately 15 GHz modulation bandwidth. The laser length is 340 μm and two 220 μm long tapers are coupling light to the Si waveguide. The first order DFB grating period is 245 nm and the duty cycle is 50%. The laser has an asymmetric λ/4 phase shift. The DFB bias and modulating signal amplitude were experimentally optimized for the best performance. The laser bias current is set around 100 mA and a 1.5 V_{pp} (assuming a 50 Ω load) data signal is used. The optical data signal is propagated through a 2 km non-zero dispersion shifted standard fiber (NZ-DSSF). At the receiver side, a variable optical attenuator (VOA) and a 40 GHz Discovery Semiconductors photodiode together with a SHF high-speed amplifier are used to boost the received signal to the desired level. The electrical data is captured by a Keysight DSA-Z634 63 GHz real time oscilloscope. The saved data was then processed off-line for BER estimation with and without equalization.

The eye diagrams for 20 GBaud PAM-4 back-to-back and after 2 km NZ-DSSF transmission measurements are depicted in Figure 4.22. PRBS sequence lengths of 2^7-1 and 2^{15} are used. In Figure 4.22 (a,b), eye diagrams for a word length of 2^7-1 in back-to-back configuration and after 2 km of transmission over NZ-DSF are shown respectively. The same is depicted in Figure 4.22 (c,d) for a word length of 2^{15} .Comparing the eye diagrams back-to-back and after 2km NZ-DSF

transmission, a deterioration can be observed, linked to the interaction between chromatic dispersion in the fiber and the inherent chirp of the laser. The resulting BER evaluated for both PRBS pattern lengths in the back-to-back and 2km fiber transmission cases are presented in Figure 4.23.
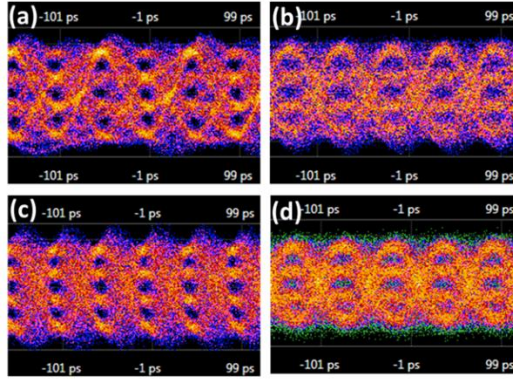
Figure 4.22: Eye diagrams for PAM-4 at 20 GBaud in back-to-back configuration and after 2km of transmission over NZ-DSF for a PRBS length of 2^7-1 (a,b) and for a length of 2^{15} (c,d).
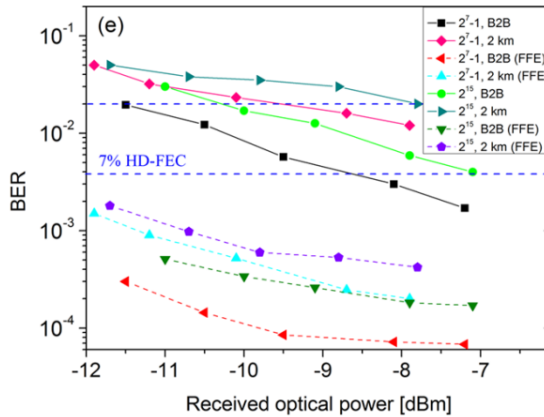
**Figure 4.23:** BER measurements for back-to-back and 2 km NZ-DSF configuration.

In the case of PAM-4, offline signal processing in MATLAB was used. This part has been done by our partner in National Technical University of Athens. A 10-tap Feed forward equalization (FFE) was used to eliminate the channel effect on the signal. As shown in Figure 4.23, the performance is significantly improved when equalization is performed.

4.4   Electrical Duobinary modulation

Since our DFB lasers' small signal responses are similar in shape to an electrical low pass filter with an almost flat response at low frequencies and a steep roll-off at the high frequencies, we tried to use a bandwidth limited DFB laser to generate an electrical duobinary signal. The laser length is 340 µm and two 220 µm long tapers are coupling light to the Si waveguide. The first order DFB grating period is 245 nm and the duty cycle is 50%. These lasers have asymmetric λ/4 phase shift. The setup was similar to the PAM-4 setup, but instead of generating a PAM-4 signal, a NRZ signal at 40 Gb/s was applied to the laser and the output signal from the laser was an ED signal.

Eye diagrams for 40 Gb/s duobinary modulation are shown in Figure 4.24. In Figure 4.24 (a,b) eye diagrams for a pattern length of 2^7-1 for back-to-back and 2km NZ-DSF transmission are shown respectively. Similarly, results for a pattern length of 2^{15} are given in Figure 4.24 (c,d). Signal post processing, decoding and BER estimation were performed offline using VPI-lab-Expert (Figure 4.25) by our partner VPI Photonics. The original signal or the electrical back-to-back signal was used to extract the original bit sequence and then this information was applied to create the PDF (probability density functions) for the three levels of the optical received signal. The BER was then estimated using Chi2 curve fitting.

Through the use of a low-complexity, 10-tap Feed Forward Equalizer (FFE), the BER can be improved. From Figure 4.25, when equalization is applied and for a 2^7-1 pattern, one can estimate less than 1.5 dB power penalty for transmission over a 2 km NZ-DSF fiber compared with the back-to-back configuration at 7% hard decision FEC limit.
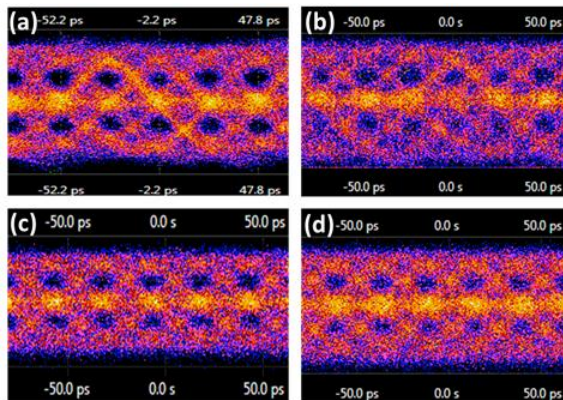
Figure 4.24: Eye diagrams for duobinary modulation at 40 Gb/s in back-to-back configuration and after 2km of transmission over NZ-DSSF for a PRBS length of 2^7-1 (a,b) and for a length of 2^{15} (c,d).
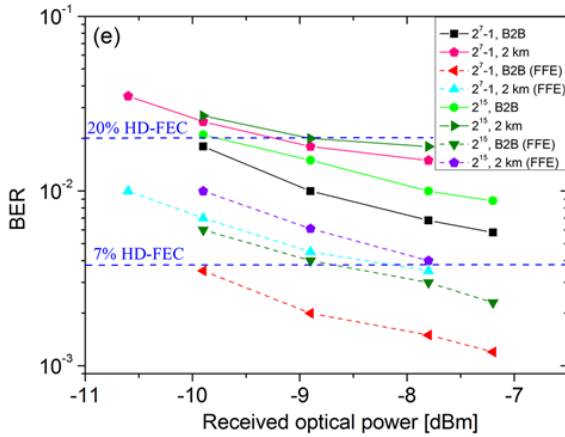
Figure 4.25: BER measurements for back-to-back and 2 km NZ-DSF configuration.

Based on the comparison of Figures 4.23 and 4.25, one may conclude that both schemes (PAM-4 and ED) are equally attractive to boost a directly modulated laser's performance for short reach links in datacenters.

4.5 Chirp managed transmission with a flat modulation response laser

In previous sections we faced two major problems for the direct modulation of heterogeneously integrated DFB lasers. One was a non-uniform small signal response for low frequencies below 5 GHz leading to a patterning effect and another one was the limited transmission distance over standard single mode fiber due to chirp and fiber dispersion. Theoretically we have shown in chapter 2 that the former problem can have two main reasons. It is partly caused by the modulation of the current into the tapers and partly by the longitudinal spatial hole burning. The latter problem will be addressed with a method called chirp managed laser (CML) direct modulation [14, 15]. In this section, we will first prove that taper current modulation is the dominant cause of the non-uniform small signal response at low modulation frequencies. Then, in the rest of the section, we will apply the CML method to reach 28 Gb/s transmission over a 20 km long standard single mode fiber.

To eliminate the tapers' dynamic characteristic from the DFB laser properties, these two sections can be electrically separated. As we discussed in chapter 3, we have designed a contact mask in a way to etch away the p-type contact layer and part of the p-InP before p-metallization in order to electrically isolate them. This is schematically illustrated in Figure 4.26-a. Figure 4.26-b shows the top view of the real fabricated devices. An electrical isolation of 3KΩ was obtained.
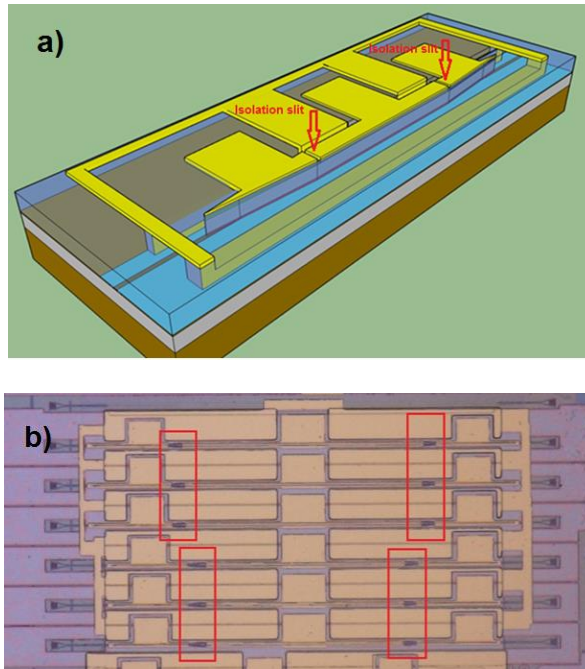
Figure 4.26: Schematic representation of the DFB laser with isolated tapers (a), a photograph of the fabricated device (isolation slits are indicated by the red rectangles).

The LIV curve of the device is shown in Figure 4.27. The laser has 7 Ω series resistance and 20 mA threshold current at 20℃. The maximum optical power in the waveguide at 100 mA is 3 mW. We have used the same Al-containing III-V epitaxial layer structure and processing for this sample as for the sample B in section 3.3.3 (InGaAlAs with 8 QWs as an active region was etched through by ICP using the laser's mesa as a mask and no cleaning processes were applied). Since the tapers are separately biased, the threshold current is reduced noticeably compared to the same laser of the sample B where the taper sections were not isolated. The laser length is 340 µm and two 220 µm long tapers are coupling light to the Si waveguide. The first order DFB grating period is 245 nm and the duty cycle is 50%. These lasers have asymmetric λ/4 phase shift. The laser's spectrum is depicted in Figure 4.28.
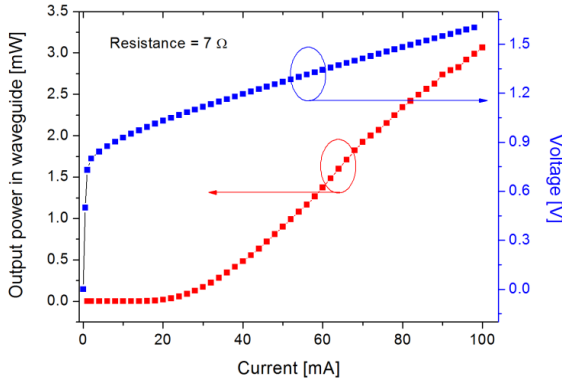
**Figure 4.27:** LIV curve of the isolated taper DFB laser.
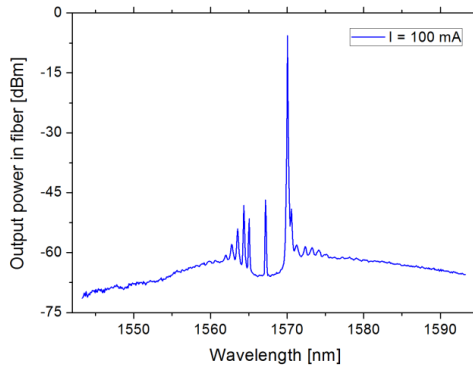
Figure 4.28: The laser single mode spectrum at 100 mA bias current.

The small signal response of the laser is shown in Figure 4.29. As the bias current increases, the low frequency part of the response is becoming flatter. This effect happens because the differential longitudinal spatial hole burning is decreasing with increasing bias current. This means that increasing the bias current results in smaller differential carrier density fluctuation with respect to the optical power. At higher bias current, there is a higher input power to the tapers and they saturate and thus the small signal response of the laser will be less affected by the tapers. Unfortunately for this laser the photon-photon resonance was not strong enough to enhance the bandwidth. The 3-dB bandwidth of the laser is 15 GHz.
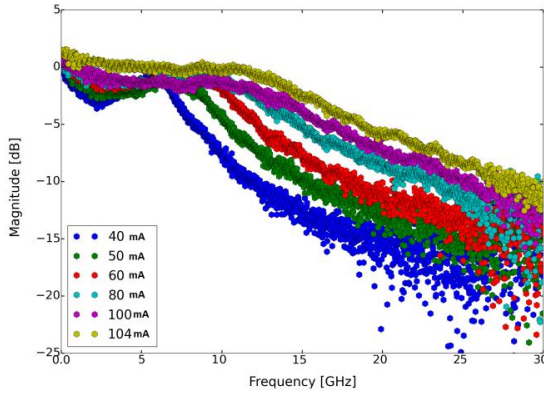
Figure 4.29: Small signal response of the laser with isolated tapers.

For the large signal measurement, the setup is modified to do the chirp management on the transmitted signal (Figure 4.30). In this figure, OTF is an optical tunable filter (commercial Santec 350 filter). The filter should be a narrow pass band filter with a moderately large slope. This kind of filters can be fabricated on-chip in the SOI platform (e.g. a ring resonator or MZI) [16, 17]. But here for the demonstration of the CML concept, we have used a commercial filter which is tunable in wavelength and bandwidth.
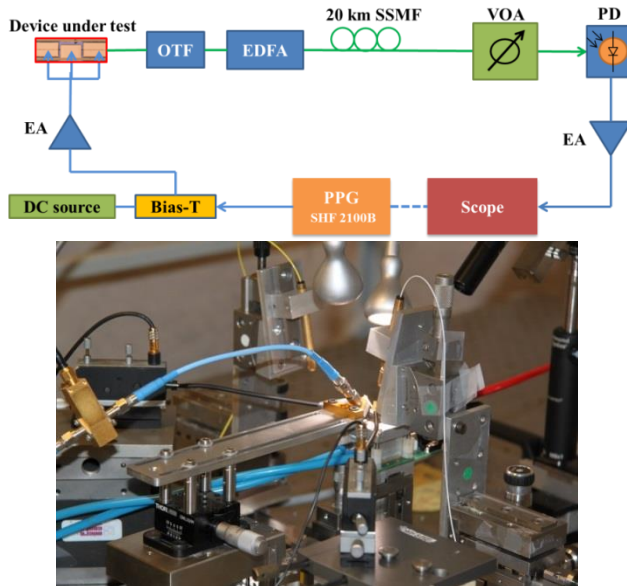

Figure 4.30: Schematic of the setup for a CML measurement (top), a photograph of the actual setup with a GSG, DC probes and vertical fiber coupling stages (bottom).

The large signal measurement has been done in two configurations: for back-to-back and after transmission over a 20 km SSMF. Our target applications are defined separately to be 10G-PON and inter-data center communication. For 10G-PON we wanted to show that the directly modulated heterogeneously integrated InP on SOI DFB laser can be used as a compact and low power consumption transmitter. At the receiver side we used a 10 Gb/s Ge/Si APD wire bonded on an electronics control board with a TIA [18]. Eye diagrams at different bias currents are shown in Figure 4.31.
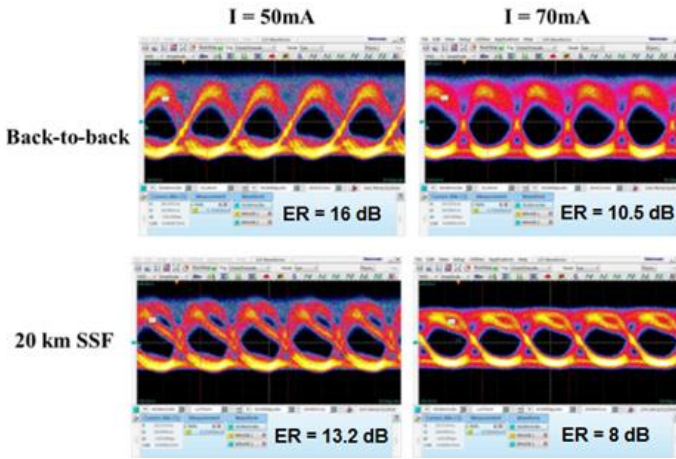

Figure 4.31: 10 Gb/s eye diagrams at different bias currents of the DFB laser for the back-to-back and over a 20 km SSMF configuration.

One can see that for all the bias currents, the eyes after transmission over the 20 km SSMF are open. As we discussed in chapter 2, in order to suppress the transient chirp the laser needs to be biased far above threshold and the RF signal peak-to-peak voltage should be small in order to not bring the laser close to the threshold. But typically, in this case the extinction ratio (ER) of the directly modulated laser would be only a few dB. Using an optical filter and aligning the laser wavelength with respect to the filter transmission slope, the ER can be dramatically increased [14, 15]. In Figure 4.32, this fact is depicted for 10 Gb/s modulation with and without filter at the 50 mA bias current. We used a filter with a 3 dB bandwidth of 0.2 nm and slope of a 2.4 dB/GHz (Figure 4.33).
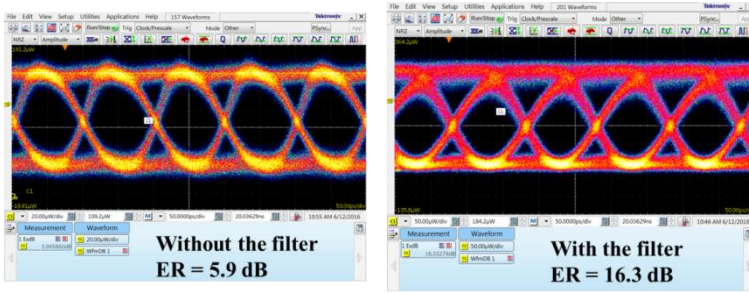
Figure 4.32: ER of the transmitted light at 50 mA without the filter (a), with the filter (b).
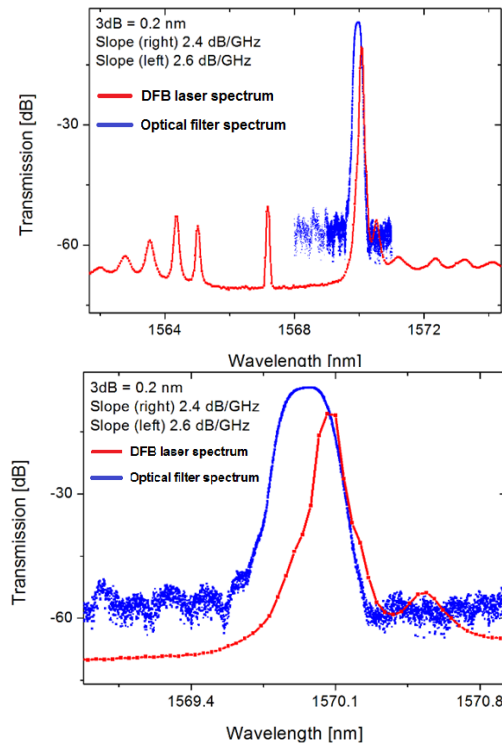
Figure 4.33: Optical spectrum of the laser with respect to the filter transmission spectrum (top), the zoom-in spectrum (bottom).

To confirm the quality of the transmitted signal, the BER was measured for each bias current in different configurations. Figure 4.34 shows the BER curves for bias currents of 50 mA and 70 mA for different PRBS pattern lengths. It is clear that the device does not suffer from the patterning effect thanks to the flat

modulation response. 1.5 dB power penalty was measured at a BER level of 10^{-9} for 20 km transmission over SSMF. The peak-to-peak RF voltage considering a 50 Ω load was 0.6 V. Because of an impedance mismatch between the transmission line and the laser just a portion of this value is actually applied to the laser.
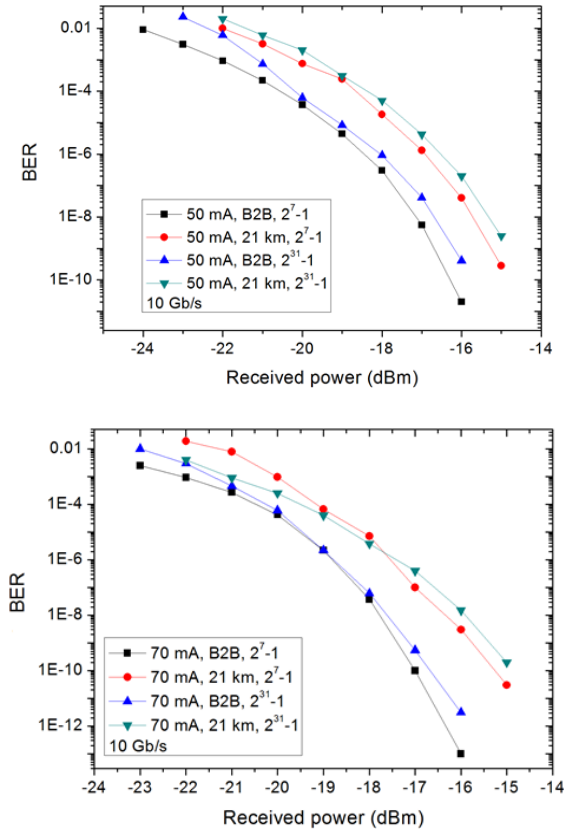
Figure 4.34: BER vs received optical power at 50 mA (top) and at 70 mA (bottom) the DFB bias currents.

For inter data-center applications, the bit rate should be higher than 10 Gb/s. Since the laser modulation bandwidth is high enough, we did the same measurements at a bit rate of 25 Gb/s and 28 Gb/s. The DFB bias current was increased to 100 mA to push the modulation bandwidth. The eye diagrams at 25 Gb/s and 28 Gb/s are shown in Figure 4.35. The RF V_{pp} was adjusted to optimize the link's performance and set to be 1 V_{pp}.
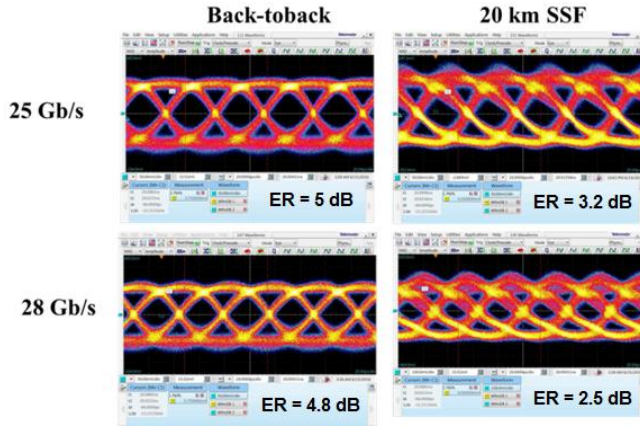
Figure 4.35: Eye diagrams at 25 Gb/s and 28 Gb/s for back-to-back and over 20 km SSMF.

BER curves for both 25 Gb/s and 28 Gb/s bit rates are shown in Figure 4.36 and 4.37, respectively. At the bit rate of 25 Gb/s, the power penalty for the fiber transmission and for the longer pattern length was 1.3 dB and 1.4 dB respectively.
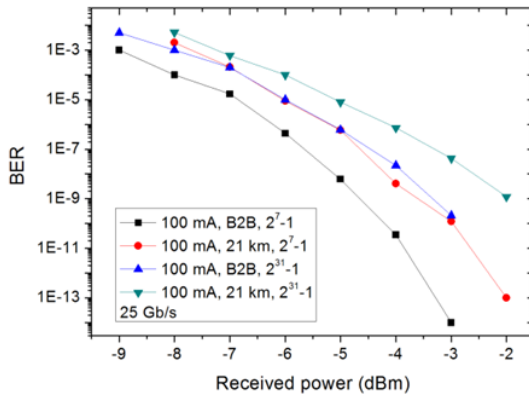
Figure 4.36: BER vs received optical power at 25 Gb/s.

At bit rate of 28 Gb/s, for the longest pattern length (2^{31}-1), the eye started to be closed after transmission over 20 km of SSMF. For this case, the measurement was very sensitive to power fluctuations and the error rate increases dramatically.
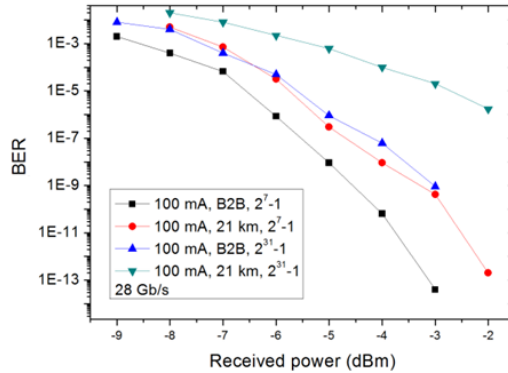
Figure 4.37: BER vs received optical power at 28 Gb/s.

In conclusion, by separating the tapers from the DFB laser and applying chirp management, we successfully demonstrated an error free 10G-PON transmission over a 20 km SSMF at 50 mA bias current and with only 0.6 volt V_{pp} RF voltage. Increasing the bias current to 100 mA, provides enough bandwidth to do 25 Gb/s error free transmission over 20 km SSMF with a PRBS pattern length of 2^{31}-1.

4.6   Conclusion

In this chapter, the heterogeneously integrated DFB laser has been used as directly modulated single mode source. We have successfully demonstrated 40 Gb/s NRZ-OOK direct modulation over a 2 km single mode fiber. This great achievement was attributed to the photon-photon resonance. The theoretical knowledge together with the technical background from the two previous chapters enabled us to fabricate a DFB laser with an extended bandwidth up to 27 GHz.

Advanced modulation schemes (PAM-4 and electrical duobinary) were successfully demonstrated at 40 Gb/s. These formats are promising solutions for short reach optical links when the bandwidth requirement for NRZ-OOK is hard to meet.

Finally a significant enhancement in the fiber link reach has been demonstrated using chirp management of the laser (CML). Putting the theoretical concepts into practice, a 28 Gb/s NRZ-OOK signal was sent over 20 km of a standard single mode fiber. This technology is of a great interest for medium reach 4 × 25 Gb/s applications.

References

[1] J. P. Reithmaier , W. Kaiser , L. Bach , A. Forchel , V. Feies , M. Gioannini , I. Montrosset , T. W. Berg and B. Tromborg, "Modulation speed enhancement by coupling to higher order resonances: A road towards 40

GHz bandwidth lasers in InP", Proc. Int. Conf. Indium Phosphide Related Mater. (ICIPRM), pp. 118-123, (2005).

[2] G. Morthier , R. Schatz and O. Kjebon, "Extended modulation bandwidth of DBR and external cavity lasers by utilizing a cavity resonance for equalization", IEEE Journal of Quantum Electronics, vol. 36(12),pp. 1468-1474, (2000).

[3] M. N. Sysak, H. Park, A. W. Fang, J. E. Bowers, R. Jones, O. Cohen, O. Raday and M. Paniccia, "Experimental and theoretical thermal analysis of a Hybrid Silicon Evanescent Laser", Optics Express, vol. 15, pp.15041-15046, (2007).

[4] C. Zhang, S. Srinivasan, Y. Tang, M. J. R. Heck, M. L. Davenport, and J. E. Bowers, "Low threshold and high speed short cavity distributed feedback hybrid silicon lasers", Optics Express, vol. 22(9), pp. 10202–10209, (2014).

[5] Y. Li, Y. Zhang, L. Zhang and A. W. Poon, "Silicon and hybrid silicon photonic devices for intra-datacenter applications: state of the art and perspectives [Invited]", Photonics Research, vol. 3, pp.10-27, (2015).

[6] Y. Matsui, H. Murai, S. Arahira, S. Kutsuzawa and Y. Ogawa, "30-GHz bandwidth 1.55-µm strain-compensated InGaAlAs-InGaAsP MQW laser", IEEE Photonics Technology Letters, vol. 9(1), pp. 25-27,(1997).

[7] T. Ishikawa and J. E. Bowers, "Band lineup and in-plane effective mass of InGaAsP or InGaAlAs on InP strained-layer quantum well", Journal of Quantum Electronics, vol. 30(2), , pp. 562–570, (1994).

[8] M. L. Xu et al., "Ultra-high differential gain in GaInAs-AlGaInAs quantum wells: experiment and modeling", IEEE Photonics Technology Letters, vol. 7(9), pp. 947-949, , (1995).

[9] A. Grabmaier, et al. "Low nonlinear gain in InGaAs/InGaAlAs separate confinement multiquantum well lasers", Applied physics letters, vol. 59(23), pp. 3024-3026, (1991).

[10] W. Kobayashi et al., "50-Gb/s Direct Modulation of a 1.3-µm InGaAlAs-Based DFB Laser With a Ridge Waveguide Structure", IEEE Journal of Selected Topics in Quantum Electronics, vol. 19(4), pp. 1500908-1500908, (2013).

[11] H. Sato, T. Tsuchiya, T. Kitatani,A. Taikeand H. Shinoda, "In-situ cleaning for highly reliable 1.3-µm InGaAlAs buried heterostructure laser". OFC(p. MF50), (2004).

[12] R. Gessner, A. Dobbinson, A. Miler, J. Rieger,and E. Veuhoff, "Fabrication of AlGaInAs and GaInAsP buried heterostructure lasers by in situ etching, Journal of crystal growth, vol. 248, pp.426-430, (2003).

[13] A. Chiuchiarelli, M. J. Fice, E. Ciaramella, and A. J. Seeds, "Effective homodyne optical phase locking to PSK signal by means of 8b10b line coding", Optics Express, vol. 19(3), pp. 1707–1712 (2011).

[14] D. Mahgereften, D. Mahgerefteh, Y. Matsui, C. Liao, B. Johnson, D. Walker,X. Zheng, Z. F. Fan, K. McCallion, and P. Tayebati, "Error-free 250 km transmission in standard fibre using compact 10 Gbit/s chirpmanaged directly modulated lasers (CML) at 1550 nm", Electronics Letter,vol. 41, pp. 543–544, (2005).

[15] D. Mahgerefteh, Y. Matsui, X. Zheng, K. McCallion, "Chirp managed laser and applications", IEEE Journal of Selected Topics in Quantum Electronics, vol.16 (5), pp. 1126, (2010).

[16] V. Cristofori, V. Kamchevska, Y. Ding, A. Shen, G. Duan, C. Peucheret, and L. K. Oxenløwe, "Error-free Dispersion-uncompensated Transmission at 20 Gb/s over SSMF using a Hybrid III-V/SOI DML with MRR Filtering",Conference on Lasers and Electro-Optics, OSA Technical Digest, paper STu1G.4, (2016).

[17] N. Chimot et al., "Monolithic Integration on InP of a DML and a Ring Resonator for Future Access Networks" IEEE Photonics Technology Letters, vol. 28(19), pp. 2039-2042,(2016).

[18] H. Chen, P. Verheyen, M. Rakowski, P. De Heyn,G. Lepage, J. De Coster, P. Absil, G. Roelkens, and J. Van Campenhout, "Low-voltage Ge avalanche photodetector for highly sensitive 10Gb/s Si photonic receivers", 11th International Conference on Group IV Photonics (GFP-2014). IEEE, (2014).

5

Conclusions and Perspectives

5.1   Conclusions

In this work, we have developed and optimized directly modulated heterogeneously integrated III-V-on-silicon DFB lasers.   We provide both theoretical and technical background for the realization of this type of lasers. It has been shown that an efficient and high speed laser can be fabricated based on heterogeneous integration on Si waveguide circuits. With the focus on the Si photonic platform for optical transceivers, the optical design has been investigated in order to have a moderate confinement factor in the QWs together with a high coupling coefficient of the grating. The coupling between the III-V and the Si waveguides is realized using an III-V/silicon spot-size converter structure defined by tapering both the III-V and silicon waveguide. This technology enables a high-efficiency, low-reflection power transfer from the III-V laser mesa to the silicon waveguide.

The fabrication process flow with details on each processing step has been provided. In order to fulfill high speed laser requirements, we have optimized the fabrication. These optimizations were utilized to fabricate heterogeneously integrated DFB lasers with large modulation bandwidth and acceptable output power.

Different epitaxial III-V structures have been used for this project based on a InGaAsP and InGaAlAs QW epitaxial layer stack. Using the InGaAsP based DFB laser with 6 QWs, we have successfully demonstrated 28 Gb/s NRZ-OOK direct modulation and transmission over a 2 km long single mode fiber. This modulation speed has been improved to 40 Gb/s NRZ-OOK by using an InGaAlAs based DFB laser with 8 QWs and extended modulation bandwidth. This modulation bandwidth enhancement was realized by introducing an

external reflector which creates a photon-photon resonance peak in the small signal response of the DFB laser.

Two advanced modulation formats for short reach optical links were investigated. At 40 Gb/s we managed to successfully demonstrate 4-level Pulse Amplitude Modulation (PAM-4) and Electrical Duobinary (ED) modulation formats and their transmission over a 2 km single mode fiber. The measurement results indicate that both schemes enable to boost a directly modulated laser's performance with limited modulation bandwidth over short reach links in datacenters.

Finally a significant enhancement in the fiber link reach has been demonstrated using chirp management of the laser (CML). Putting the theoretical concepts into practice, a 28 Gb/s NRZ-OOK signal was sent over 20 km of a standard single mode fiber.

5.2 Perspectives

We have presented a heterogeneous platform for integrating a directly modulated DFB laser on Si photonic circuits. Different aspects of this technology such as modulation bandwidth, maximum transmission reach and static properties of the lasers have been discussed. In order to move this technology forward toward more reliable and efficient devices, we need to put more effort on optimization and also exploring new techniques. In this context, a few ideas can be investigated:

5.2.1 Thermal management

The small size of our fabricated DFB lasers makes the thermal management of these lasers challenging. Heating is one of the major obstacles to achieve higher energy efficiency and higher integration density. The thick buried oxide (BOX) layer in silicon-on-insulator (SOI) has a poor thermal conductivity and prevents efficient heat dissipation in the substrate. This thermal management becomes especially an issue when one wants to use quantum wells which have low conduction band offsets. For these materials, it is well known that the photon emission process is very temperature dependent and that high speed lasers fabricated using this material system suffer from thermal instability. A future direction for the research on III-V-on-Si lasers may therefore be directed towards improving the quantum-well material. Optimized Al-containing QWs with a large conduction band offset will ensure the high speed direct modulation at higher temperatures without performance deterioration.

5.2.2 4-channel multiplexed transmitter

In this PhD, we have demonstrated a single channel transmitter based on heterogeneously integrated DFB laser, but in general these individual transmitters can be multiplexed to increase the optical line capacity. Since in Si photonic circuits wavelength multiplexers can be easily realized with high

efficiency, it will be attractive to demonstrate a 4-channel multiplexed transmitter for 100 G applications.

5.2.3 Integration with a ring resonator reshaper for chirp management

In the chirp management section, we already mentioned that on-chip optical filters such as ring resonators can be integrated with the Si photonic circuit. Using a ring resonator with an integrated heater has been shown to be a low insertion loss and compact filter to realize the chirp managed laser (CML) [1]. Ring resonators in the Si platform have been studied intensively for different applications. This mature technology enables to design and fabricate a ring resonator based optical spectral reshaper with a desired bandwidth and slope.

5.2.4 Beyond 40 Gb/s with equalization

As we mentioned earlier in chapter two, equalization provides an effective method to enhance the quality of a transmitted optical signal by pushing the system complexity to the electronic domain. In this domain, equalization techniques have been developed both for electronics and photonics. We have shown in chapter four that utilizing these techniques can improve the quality of the transmitted signal quality significantly. The next step would be to leverage the power of equalization and push the modulation bit rate beyond 40 Gb/s.

References

[1] V. Cristofori, V. Kamchevska, Y. Ding, A. Shen, G. Duan, C. Peucheret, and L. K. Oxenløwe, "Error-free Dispersion-uncompensated Transmission at 20 Gb/s over SSMF using a Hybrid III-V/SOI DML with MRR Filtering",Conference on Lasers and Electro-Optics, OSA Technical Digest, paper STu1G.4, (2016).